

T-4565

The Effect of Thermal Expansion Mismatch Between the Intergranular Glass, Crystal, and  
Alumina Phases on the Mechanical Properties of Alumina Ceramics

by

Mark W. Krutyholowa

ProQuest Number: 10784000

All rights reserved

INFORMATION TO ALL USERS

The quality of this reproduction is dependent upon the quality of the copy submitted.

In the unlikely event that the author did not send a complete manuscript and there are missing pages, these will be noted. Also, if material had to be removed, a note will indicate the deletion.



ProQuest 10784000

Published by ProQuest LLC (2018). Copyright of the Dissertation is held by the Author.

All rights reserved.

This work is protected against unauthorized copying under Title 17, United States Code  
Microform Edition © ProQuest LLC.

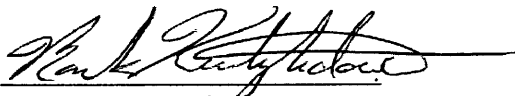
ProQuest LLC.  
789 East Eisenhower Parkway  
P.O. Box 1346  
Ann Arbor, MI 48106 – 1346


T-4565

A thesis submitted to the Faculty and the Board of Trustees of the Colorado School of Mines in partial fulfillment of the requirements for the degree of Master of Science (Materials Science).

Golden, Colorado

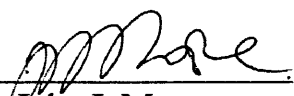
Date 5/12/94.

Signed:   
Mark Krutyholowa

Approved:   
Dr. Michael J. Haun  
Thesis Advisor

Golden, Colorado

Date 5/12/94.

  
Dr. John J. Moore  
Professor and Head,  
Department of Materials  
Science

ARTHUR LAKES LIBRARY  
COLORADO SCHOOL OF MINES  
GOLDEN, CO 80401

## ABSTRACT

Glass-ceramic compositions in the BaO-Al<sub>2</sub>O<sub>3</sub>-SiO<sub>2</sub> system were controlled to crystallize monoclinic or hexagonal (hexacelsian) forms of celsian (BaAl<sub>2</sub>Si<sub>2</sub>O<sub>8</sub>). Because the thermal expansion coefficients of these phases are significantly different (2.7 ppm/°C for celsian and 8.0 for hexacelsian), glass-ceramics in this system were investigated as intergranular species for thermal expansion mismatch toughening of high alumina ceramics.

Low melting compositions, deficient in alumina compared to stoichiometric celsian, were prepared into glass powders, and then combined with crystalline alumina powder. Results of qualitative and quantitative x-ray diffraction analysis showed that crystallization of celsian and hexacelsian can be controlled by varying the amount of alumina, composition, and heat treatment conditions. Computational modeling provided the amount of alumina dissolution, and the thermal expansion coefficients of the residual glass in 96 weight percent aluminas. Modeling then resulted in glass compositions that satisfied different types of thermal expansion mismatch models.

Mechanical testing was conducted on compositions satisfying the various thermal expansion mismatch models. Flexural strength was found to be linearly dependent upon glass composition and was a maximum for high silica content glasses. Toughness was more sensitive to residual stress states, and was a maximum in compositions crystallizing low TCE crystal phases with high TCE residual glasses. Glasses with low TCE are put into a state of compression, resulting in transgranular fracture, high strength, and low



toughness, while glasses with high TCE are put into tension resulting in intergranular fracture, low strength, and high toughness.

A process known as transient glass phase processing was observed during this research. This process dissolved crystalline alumina into an alumina deficient glass, driving the glass composition toward stoichiometric celsian, thereby crystallizing large amounts of celsian polymorphs.

## TABLE OF CONTENTS

ABSTRACT .....	iii
LIST OF FIGURES .....	x
LIST OF TABLES .....	xiii
ACKNOWLEDGEMENT .....	xv
DEDICATION .....	xvi
CHAPTER 1. INTRODUCTION .....	1
CHAPTER 2. LITERATURE SURVEY .....	6
2.1. Alumina Ceramics: Applications, Processing, and Properties.....	6
2.2. Microstructure and Mechanical Properties .....	8
2.3. Theory: Thermal Expansion Mismatch Toughening .....	10
2.4. The BaO-Al <sub>2</sub> O <sub>3</sub> -SiO <sub>2</sub> System.....	13
CHAPTER 3. PHASE 1: QUALITATIVE CRYSTALLIZATION BEHAVIOR OF BaO-Al <sub>2</sub> O <sub>3</sub> -SiO <sub>2</sub> GLASSES IN ALUMINA CERAMICS .....	16
3.1 Compositions Evaluated .....	16

3.2 Experimental Methodology .....	20
3.2.1 Preparation of Glass Powders .....	20
3.2.2. Addition of Alumina to Glass Powders.....	20
3.2.3. Forming and Sintering.....	21
3.3. Analytical Methodology: Qualitative X-Ray Diffraction of Samples ...	23
3.4 Results and Discussion .....	23
3.5. Summary and Conclusions.....	36
<b>CHAPTER 4. PHASE 2: QUANTITATIVE CRYSTALLIZATION AND ALUMINA DISSOLUTION BEHAVIOR OF BaO-Al<sub>2</sub>O<sub>3</sub>-SiO<sub>2</sub> GLASSES IN ALUMINA CERAMICS .....</b>	<b>38</b>
4.1 Compositions Evaluated and Experimental Methodology.....	39
4.2. Analytical Methodology: Quantitative X-Ray Diffraction.....	40
4.2.1. The Matrix - Flushing Method .....	40
4.2.1a Multicomponent Analysis .....	41
4.2.1b Amorphous Phase Content Analysis .....	42
4.2.1c Binary Mixture Analysis (Auto-Flushing) .....	42
4.2.2 Analytical Procedure.....	43
4.2.3. I/I <sub>COR</sub> Verification .....	45
4.3. Analytical Methodology: Alumina Dissolution.....	49
4.4. Analytical Methodology: Density Evaluation .....	50
4.4.1. Residual Glass: Composition and Density.....	50
4.4.2 Bulk, Theoretical, and Percent Theoretical Density .....	52
4.5 Results and Discussion .....	53

4.5.1 Quantitative X-ray Diffraction Analysis and Alumina Dissolution .....	53
4.5.1a 0% Alumina Addition.....	54
4.5.1b 50% Alumina Addition.....	55
4.5.1c 75% Alumina Addition.....	59
4.5.1d 96% Alumina Addition.....	61
4.5.1e MoO <sub>3</sub> Addition.....	62
4.5.2 Densification Analysis.....	63
4.6. Summary and Conclusions.....	68
Transient Glass Phase Processing (TGPP).....	69
<b>CHAPTER 5. PHASE 3: 96% ALUMINA - ALUMINA DISSOLUTION, RESIDUAL GLASS THERMAL EXPANSION, AND COMPOSITIONAL MODELING FOR MISMATCH ANALYSIS .....</b>	<b>72</b>
5.1. Alumina Dissolution .....	73
5.1.1. Methodology .....	74
5.1.2. Results and Discussion.....	75
5.2. The Thermal Expansion of the Residual Glass.....	79
5.2.1. Estimation of the Thermal Expansion of Oxide Glasses .....	79
5.2.2. Methodology: TCE Calculation of Residual Glass in 96% Alumina.....	81
5.2.3. Results and Discussion.....	82
5.3. Compositional Modeling for Thermal Expansion Mismatch Analysis....	87
5.3.1. Direct Observation.....	88
5.3.2. Computational Modeling.....	88
5.3.3. Results and Discussion.....	91
5.4. Summary and Conclusions.....	95

**CHAPTER 6. PHASE 4: THE EFFECT OF THERMAL EXPANSION MISMATCH ON THE MECHANICAL PROPERTIES OF 96% ALUMINA..... 97**

6.1. Experimental Methodology ..... 97

    6.1.1. Preparation of 96 Weight Percent Alumina Powders ..... 98

    6.1.2. Compositional Qualification..... 99

    6.1.3. Fabrication of Mechanical Test Specimens ..... 100

6.2. Analytical Methodology ..... 101

    6.2.1. Fixture Used for Mechanical Testing..... 101

    6.2.2. Flexural Strength ..... 102

    6.2.3. Fracture Toughness ..... 103

    6.2.4. Fractography ..... 106

6.3. Results and Discussion ..... 107

    6.3.1. Compositional Qualification ..... 107

    6.3.2. Stress State ..... 108

    6.3.3. Fractography ..... 109

    6.3.4. Flexural Strength..... 115

    6.3.5. Fracture Toughness..... 118

6.4. Summary and Conclusions ..... 122

**CHAPTER 7. CONCLUSIONS AND FUTURE WORK..... 123**

**REFERENCES CITED ..... 127**

**APPENDIX A: QUALITATIVE ANALYSIS ..... 132**

**APPENDIX B: QUANTITATIVE ANALYSIS..... 139**

T-4565

APPENDIX C: MECHANICAL TESTING..... 148

## LIST OF FIGURES

Figure 1.1. Methodology of experimental work, data obtained, and objectives met .....	4
Figure 2.1. Characteristic fractures in a two-phase structure with spherical particles dispersed in a homogeneous matrix. ....	12
Figure 2.2. Thoria spheres in a glass matrix. (a) TCE glass > TCE thoria;(b) TCE thoria > TCE glass. ....	12
Figure 2.3. A schematic representation of the effect of microcracks on the propogation of cracks. ....	13
Figure 2.4. Structure of celsian. ....	15
Figure 2.5. Structure of hexacelsian. ....	15
Figure 3.1. BaO-Al <sub>2</sub> O <sub>3</sub> -SiO <sub>2</sub> Phase Diagram. ....	18
Figure 3.2. Qualitative x-ray diffraction patterns with 0 and 50 percent alumina addition. (a) Composition 2a .....	25
(b) Composition 2b.....	26
(c) Composition 3a .....	27
(d) Composition 3b.....	28
(e) Composition 4a.....	29
(f) Composition 4b .....	30
Figure 3.3. Qualitative x-ray diffraction patterns for samples with 96 percent alumina addition. (a) Composition 2.....	31
(b) Composition 3.....	32
(c) Composition 4.....	33
Figure 4.1. Calibration Curve of Hexacelsian .....	49

Figure 4.2. Weight percent crystalline phases (A-C), Residual glass composition (E-G); Alumina dissolution (D,H), for 0%alumina addition.....	56
Figure 4.3. Weight percent crystalline phases (A-C), Residual glass composition (E-G); Alumina dissolution (D,H), for 50%alumina addition.....	58
Figure 4.4. Weight percent crystalline phases (A-C), Residual glass composition (E-G); Alumina dissolution (D,H), for 75%alumina addition.....	60
Figure 4.5: Quantitative crystallization results comparing composition 3a and 3b with 0% alumina addition.....	64
Figure 4.6: Quantitative crystallization results comparing composition 3a and 3b with 50% alumina addition.....	65
Figure 4.7: Quantitative crystallization results comparing composition 3a and 3b with 75% alumina addition.....	66
Figure 4.8: The percent theoretical density plotted versus temperature for 0 (A), 50 (B), 75(C), and 96 weight percent (D) alumina addition.....	67
Figure 4.9. Schematic representation of glass composition as it increases in alumina content due to transient glass phase processing.....	71
Figure 5.1. The weight percent alumina in crystal + glass plotted versus the firing temperature for composition 2a with $\text{SiO}_2/\text{BaO}=4$ .....	76
Figure 5.2. The weight percent alumina in crystal + glass plotted versus the firing temperature for composition 3b with $\text{SiO}_2/\text{BaO}=2$ .....	77
Figure 5.3. The weight percent alumina in crystal + glass plotted versus the firing temperature for composition 4a with $\text{SiO}_2/\text{BaO}=1.4$ .....	78
Figure 5.4. Percent maximum crystallization and TCE of the residual glass vs. dissolution for composition 2a.....	84
Figure 5.5. Percent maximum crystallization and TCE of the residual glass vs. dissolution for composition 3b.....	85



Figure 5.6. Percent maximum crystallization and TCE of the residual glass vs. dissolution for composition 4a. .... 86

Figure 5.7. The TCE of a silicate based glass plotted versus modifier addition calculated from Hormadaly's [52] model. .... 90

Figure 6.1. General schematic of a four-point - 1/4 - point fixture suitable for sintered, heat treated, or oxidized specimens. .... 103

Figure 6.2. Diagram of MOR specimens with location of indents shown. The measured crack length, 2C, is also shown..... 104

Figure 6.3. Photomicrograph at 1000X of composition 4a, showing intergranular fracture. .... 111

Figure 6.4. Photomicrograph at 1000X of composition 29, showing predominantly intergranular fracture with aspects of transgranular fracture..... 111

Figure 6.5. Photomicrograph at 1000X of composition 2a, showing predominantly mixed intergranular and transgranular fracture ..... 112

Figure 6.6. Photomicrograph at 1000X of composition 6, showing predominantly transgranular fracture with aspects of intergranular fracture..... 112

Figure 6.7. Photomicrograph at 1000X of composition 34, showing transgranular fracture. .... 113

Figure 6.8. Modes of fracture plotted versus the SiO<sub>2</sub>/BaO ratio. .... 114

Figure 6.9. Results of the flexural strength analysis as a function of composition. .. .... 117

Figure 6.10. Results of fracture toughness showing K<sub>ISB</sub>, K<sub>ICB</sub>, and K<sub>ICA</sub>. .. 119

Figure 6.11. Summary of the fracture toughness (K<sub>ISB</sub>) results as a function of composition. .... 120

## LIST OF TABLES

Table 1.1. Thermal Expansion Mismatch Models .....	2
Table 3.1. Initial Barium Aluminosilicate Compositions.....	17
Table 3.2. Compositions Evaluated .....	19
Table 3.3 Firing Temperatures (°C).....	22
Table 3.4 Qualitative Results: Preliminary Analysis .....	24
Table 3.5. Summary of qualitative results, detailed analysis. ....	34
Table 4.1 Weight Percent Sample and Quartz Standard .....	43
Table 4.2. $I/I_{COR}$ Values and Peaks Used for Analysis.....	44
Table 4.3. Sources of Crystalline Materials .....	46
Table 4.4. Comparison of Experimental and JCPDS ( $I/I_{COR}$ ) Values .....	46
Table 4.5. Qualification Results of Hexacelsian and Mullite.....	47
Table 4.6. X-Ray Densities of the Crystalline Phases.....	52
Table 4.7 Ratio of Crystalline Phases in 96% Alumina at 1640°C.....	62
Table 5.1. Compositions Used in Phase 3 .....	73
Table 5.2. Results of Alumina Dissolution in 96% Alumina Ceramics.....	75
Table 5.3. Thermal Expansion Mismatch Models .....	87
Table 5.4. Results of Direct Observation.....	92

Table 5.5. Starting Glass Compositions of Observed Compositions .....	93
Table 5.6. Results of Compositional Modeling .....	95
Table 6.1. Compositions Satisfying the Six Thermal Expansion Mismatch Models. .....	98
Table 6.2 Amount of Constituents in 96% Alumina Powders.....	99
Table 6.3. Results of Qualification Analysis.....	107
Table 6.4. Resultant Stress States of Qualified Compositions .....	109
Table 6.5. Resultant Stress States of Qualified Compositions .....	110

## ACKNOWLEDGMENT

This research was funded by Coors Ceramics Company, Golden Technologies, Inc., and the National Science Foundation through the Colorado Center for Advanced Ceramics. I would like to thank all personnel involved for their patience and generous support.

I would like to sincerely thank and express my gratitude to Dr. Michael Haun for serving as my advisor, colleague, and continued driving force in completing my thesis. Also, I would like to thank Ivan Cornejo, Boen Houng, Yangdo Kim, Chris Reed, and Steve Landin for their friendship. Without these fellow students, completion and execution of my work would have been more difficult.

I wish to express my thanks to all who helped in the technical execution of my project: Catherine Walter, Coors Ceramics; Kathy Krutyholowa and Tony Galeger, Ricerca, Inc.; and Jack Sibold and Terrence Brog, Golden Technologies.

Finally I would like to express my appreciation to Troy Tack of Ashurst Technology for hiring me. I believe that the opportunity he has given me will allow me to develop the skills and knowledge that I have attained at The Colorado School of Mines.

## **DEDICATION**

This thesis is meant for those who have tried and did not succeed, rather than for those who have succeeded without trying. They are the ones who know the true meaning of  
success.

## CHAPTER 1

### INTRODUCTION

The properties of glass-bonded alumina ceramics are strongly affected by the vitreous intergranular phase that forms throughout the microstructure [1,2]. The vitreous phase often partially devitrifies during the initial firing or upon subsequent heat treatments forming crystalline phases that further influence properties. Heat treatment to promote crystallization has resulted in enhancements in fracture toughness [2].

The improvement in fracture toughness is in part due to such phenomenon as microcracking and grain bridging [3,4]. Such mechanisms are inherently related to the thermal expansion mismatch between the crystalline, glassy, and alumina phases present. Previous research by N. W. Chen *et. al.* [5-7] investigated the mechanical properties of alumina ceramics with intergranular glass and crystalline phases having a thermal coefficient of expansion (TCE) either higher or lower than that of the alumina. The results show that when the TCE of the residual glass is higher than alumina, the glass is in tension and intergranular type fracture occurs, resulting in high fracture toughness. However, when the TCE of the residual glass is lower than alumina, the glass is in compression and transgranular type fracture occurs, resulting in lower fracture toughness.

The types of thermal expansion mismatch previously studied [5-7] focused on the differences in TCE between the residual glass and crystalline phases compared to alumina. However, this research did not investigate all of the types of thermal expansion mismatch possible by considering the differences in thermal expansion between the residual glass and

crystalline phases. Thus the objective of this research was to further investigate the effect of thermal expansion mismatch between the intergranular glass, crystalline, and alumina phases on the mechanical properties of strength and toughness in 96 weight percent alumina.

To evaluate the effect of TCE mismatch on the mechanical properties, a model matrix was devised relating the thermal expansions of each of the phases. Table 1.1 summarizes these models.

Table 1.1. Thermal Expansion Mismatch Models

Phase	1	2	3	4	5	6
Alumina	High	High	Med	Med	Low	Low
Glass	Med	Low	High	Low	High	Med
Crystal	Low	Med	Low	High	Med	High

Within each model the words High, Med, and Low represent the value of the thermal expansion for that phase, relative to all other phases. For example in Model 1 the thermal expansion of the alumina is high relative to that of both the glass and the crystal; the thermal expansion of the glass is lower than that of the alumina but higher than that of the crystal; and the thermal expansion of the crystal is low relative to that of both the crystal and alumina.

The research of N. W. Chen *et. al.* [5-7] investigated the effects of TCE mismatch utilizing a number of glass systems. To reduce the variation of composition in this research only one glass system was chosen for investigation; BaO-Al<sub>2</sub>O<sub>3</sub>-SiO<sub>2</sub>. The barium aluminosilicate system is ideal for providing an array of mismatch models. Glass-

ceramic compositions from this system typically crystallize monoclinic or hexagonal forms of  $\text{BaAl}_2\text{Si}_2\text{O}_8$ . The monoclinic phase (celsian) is stable below  $1590^\circ\text{C}$  while the hexagonal form (hexacelsian) is stable above this temperature. The thermal expansion coefficients are significantly different for these two polymorphs;  $2.7 \text{ ppm}/^\circ\text{C}$  (from  $20$ - $1000^\circ\text{C}$ ) for celsian versus  $8.0 \text{ ppm}/^\circ\text{C}$  (from  $300$ - $1000^\circ\text{C}$ ) for hexacelsian [8]. The thermal expansion of celsian and hexacelsian are lower and higher than that of alumina respectively. Thus by utilizing these two phases the above thermal expansion mismatch models can potentially be attained.

To fulfill all the proposed models the following methodology was used. After the mismatch matrix was set-up and the glass system chosen, four phases of work were conducted. Figure 1.1 summarizes these phases by the data generated and objectives that the data attained. Phase one provided qualitative crystallization data on a variety of  $\text{BaO}$ - $\text{Al}_2\text{O}_3$ - $\text{SiO}_2$  compositions to determine the potential of attaining the different types of mismatch models. Phase two provided the percentages of the various crystalline phases and residual glass. The objective of this phase was to obtain a quantitative knowledge of the alumina dissolution by which the composition and thermal expansion of the residual glass could be attained for 96 weight percent alumina. Phase three provided the composition and thermal expansion of the residual glass of 96 weight percent aluminas. Also new compositions were presented based on the remodeling of existing compositions, using the TCE as the modeling parameter. The objective of phase three was to fulfill the mismatch models through the analysis of original and remodeled compositions. Phase four provided the mechanical properties of toughness and strength for the satisfied models. The objective of phase four was to correlate the mismatch models with the mechanical properties.



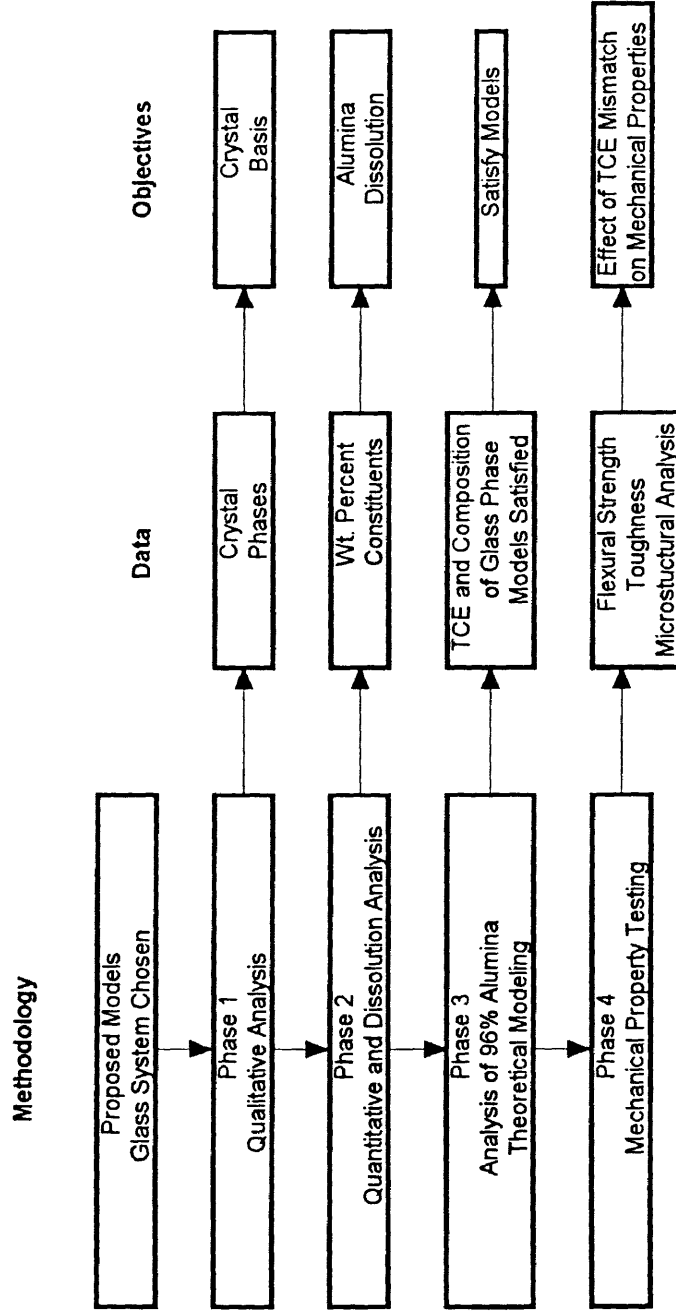


Figure 1.1. Methodology of experimental work; data obtained; objectives met.

As already explained the experimental work was divided into four phases. Utilizing this natural division each phase will be presented as a chapter, outlining the objectives, experimental work, and results that are relevant and important to the given phase of work. A literature review and history of the present work will be discussed in the next chapter. Chapters 3-6 will present each phase of experimental work. Chapter 7 will conclude by presenting the conclusions and future work.

## CHAPTER 2

### LITERATURE SURVEY

#### **2.1 Alumina Ceramics: Applications, Processing, and Properties**

Alumina ceramics have historically been used in a variety of applications, including industrial ceramics, electronic substrates, electrical insulators, refractories, optical glass, fine china, and abrasives [9,10]. Typically 85-99.8 weight percent alumina is used in such applications. The balance of the material is composed of talc, clay, kaolin, etc., which aids in the processing of the alumina [11]. The present research is focused on 96 weight percent alumina ceramics used generally for electronic substrate and structural applications. These substrates provide good thermal conductivity, electrical insulation, dimensional stability, chemical durability, and mechanical strength at very low cost [11].

The commercial processing of 96 weight percent alumina ceramics for substrate applications can be divided into three general sections: raw material preparation, forming, and sintering [12]. A finishing step is also used, but for purposes of brevity will not be discussed. Raw materials consisting of alumina, talc, clay, kaolin, etc., are first carefully measured, and then combined with binders, deflocculants, lubricants, and water [12]. Talc, kaolin, and other additives are introduced in order to lower the sintering temperature, enhance the formability, green strength, and densification, and to control the microstructure. Binders and lubricants are added in order to aid in green forming [13]. The resultant slurry is then ball milled and spray dried in order to produce a uniform free

flowing powder [12,13]. The powder is then formed into substrate materials through continuous tape casting or roll compaction [14]. In the continuous tape casting process the powder slurry is not spray dried but is aged until consistent slurry properties are achieved [13]. The slip or slurry is cast onto a moving plastic sheet to produce a flat thin ribbon of pre-sintered product [14]. In the roll compaction process, the spray dried product is passed between hardened rollers to form a thin, flat, green ceramic ribbon [12, 14].

The green alumina ceramic is then sintered at a temperature of 1600°C [12]. During sintering the additives form a liquid phase promoting liquid-phase sintering within the material. This process reduces the sintering temperature, improves densification, and aids in microstructural control. In order for liquid phase sintering to occur, several requirements must be met. The additives must form about 1-2 volume percent liquid. The liquid phase formed must wet the solid, and must dissolve the solid phase at elevated temperatures [15-19]. While the mixture of solid particles and liquid phase sinter together, the porosity of the powder compact gradually diminishes to form a dense ceramic part [16-24].

The properties of such substrates have been previously mentioned. They include good thermal conductivity, electrical insulation, dimensional stability, chemical durability, and mechanical strength. This research is only concerned with the properties of flexural strength and toughness. Flexural strength or bend strength is defined as the maximum tensile stress in the surface of a specimen fractured in bending [25]. For 96 weight percent alumina the flexural strength is about 300-350MPa [10]. The toughness is from 4-5 MPa/m<sup>2</sup> [9] and is defined as the resistance of the material to crack propagation. Toughness of electronic substrates is important in such applications as multilayer and

thick-film substrates. Often, the substrate fractures prematurely due to stresses produced by TCE mismatch between the silicon and alumina substrates [26]. This mismatch is due to the thermal cycling that the substrates undergo during use. To increase the life of such substrates, toughness must be maximized without degrading strength [25]. Several authors have shown that by carefully controlling the microstructure toughness may be maximized [5,27].

## **2.2 Microstructure and Mechanical Properties**

Much of the past emphasis in ceramics has been in achieving the most uniform particle size, resulting in ceramics with fewer flaws and higher mechanical strength [28,29]. The property of toughness is however more sensitive to processing flaws than is mechanical strength [4]. To optimize the toughness and strength, new processing routes are needed to control both the geometry and chemistry of the starting powders, and thereby the microstructure [29]. Knowledge and control of the microstructure are of great importance in thermal expansion mismatch toughening where the composition of the residual glass must be controlled, as well as the intergranular crystalline phases [5].

The understanding of thermal expansion mismatch, or microstructure, and its effect on the toughness of alumina ceramics has been pursued for the last decade. Hansen and Philips [30] were the first to critically characterize the microstructure of high alumina ceramics. They found that glassy triple points existed within the bulk alumina, which were artifacts of liquid phase sintering. Wiederhorn [31] showed that the glassy phase partially devitrified within the triple points. Heuer and Labun [32] observed microcracking that occurred along the grain boundaries between the alumina and devitrified glassy phase.

From this observation the authors concluded that the source of such microcracking was the thermal expansion mismatch between the alumina and devitrified glass [32].

From the work cited above, a great deal was learned about the microstructure and about the sources of such phenomenon as microcracking within the microstructure. The role of such microstructures on the toughness of alumina ceramics was virtually unknown until the work of Tomaszewski [33]. Tomaszewski showed that through the direct crystallization of the glassy phase microcracks were produced. The presence of these microcracks increased the toughness of the alumina [33]. Dogon and Heuer took the work somewhat further, observing the effects of various crystal-alumina mismatches on the toughness of alumina ceramics [34]. However, in addition to the effect of the crystalline phase the glassy phase did not completely devitrify and some residual glass remained, having possible effects on toughness due to the thermal expansion mismatch with the alumina. Work by N.W. Chen and M.J. Haun addressed this issue in 96 weight percent alumina ceramics. The authors looked at various crystal-alumina and glass-alumina combinations, and found that the glass phase does indeed contribute to thermal expansion mismatch toughening in 96% alumina [5]. However no work has been completed in evaluating the combined effects of both crystal-alumina and glass-alumina mismatches on the toughness of alumina ceramics, thereby facilitating the objective of this thesis.

### 2.3. Theory: Thermal Expansion Mismatch Toughening

As detailed above such phenomenon as microcracking contribute to the toughening of alumina ceramics. This process is related to residual stresses,  $\sigma_R$ , produced via thermal expansion mismatch [35]. Instead of detailing the phenomenological equations behind microcracking, which are very complex, a simple theory of stresses produced through thermal expansion mismatch will be presented. Following this, a schematic representation of microcracking will be presented regarding such stresses.

The phenomena of thermal expansion mismatch in alumina can be expressed as a two phase structure with spherical particles (Z) dispersed in a homogeneous matrix (M). The particles tend to crack if their expansion is higher and strength lower than the other phases (Figure 2.1a). However, if the weakest points occur at grain boundaries or in the matrix, the cracks may form in these locations approximately following the contour of the grains (Figure 2.1b,c). If on the other hand, the matrix shows a greater expansion than the dispersed particles, the cracks will arise in it (Figure 2.1d). Finally, when the expansion of all phases is similar, the cracks will propagate through both the particle and matrix (Figure 2.1e) [25].

Figure 2.2 shows micrographs of theoria spheres in a glass matrix, where the glass is of different TCE in both cases. Figure 2.2a corresponds to Figure 2.1d,e and Figure 2.2b corresponds to Figure2.1b,c. The residual stresses that occur in the above situations can be expressed by the following equation:

$$\sigma_R = \Delta\alpha \Delta T / [(1+\nu_M) / 2E_M + (1-2\nu_P) / E_P]$$

where subscripts M and P refer to matrix and particle,  $\Delta\alpha = \alpha_M - \alpha_P$  is the differential thermal expansion coefficient (controlled by the glass composition),  $\Delta T$  is the temperature range of cooling,  $\nu$  and  $E$  are Poisson's ratio and Young's modulus [35]. Relating the above mismatch, stresses produced, and fracture behavior the following is observed. When the matrix expansion is greater than the particle the matrix is placed in "hoop tension" and the crack is attracted to the particle, resulting in transgranular fracture as shown in Figure 2.2a. If the particle expansion is greater, a state of "radial tension" is obtained in the matrix, and the crack is repelled. This radial tension results in intergranular fracture, as shown in Figure 2.2b [35].

In 96 weight percent alumina, the above model may be applied as follows. The matrix is defined as alumina while the particles are the devitrified glass and residual glass. When a state of hoop tension results in the alumina, intergranular fracture occurs. Transgranular fracture occurs when a state of radial tension occurs in the matrix or alumina phase.

Microcracking increases toughness by constricting or slowing a crack from propagating. A schematic of this process is shown in Figure 2.3. Microcracks, M, form through various types of thermal expansion mismatch. These TCE mismatches can be expressed as stresses,  $\sigma_R$ . As a crack, P, propagates, the stress,  $\sigma_R$ , acts on the crack closing the crack front [35]. Upon closing the front the crack propagation is slowed, increasing toughness.



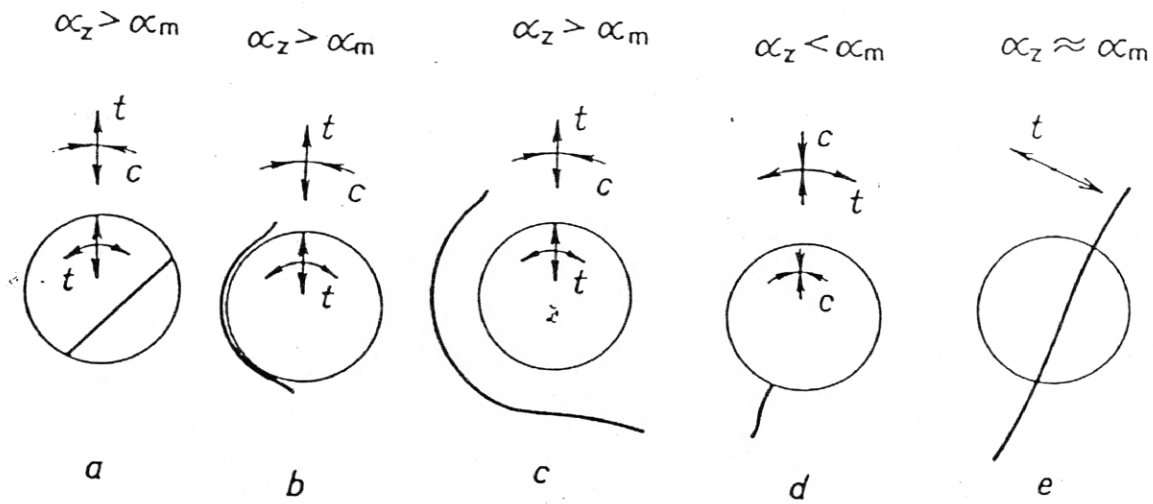


Figure 2.1. Characteristic fractures in a two-phase structure with spherical particles dispersed in a homogeneous matrix [25].

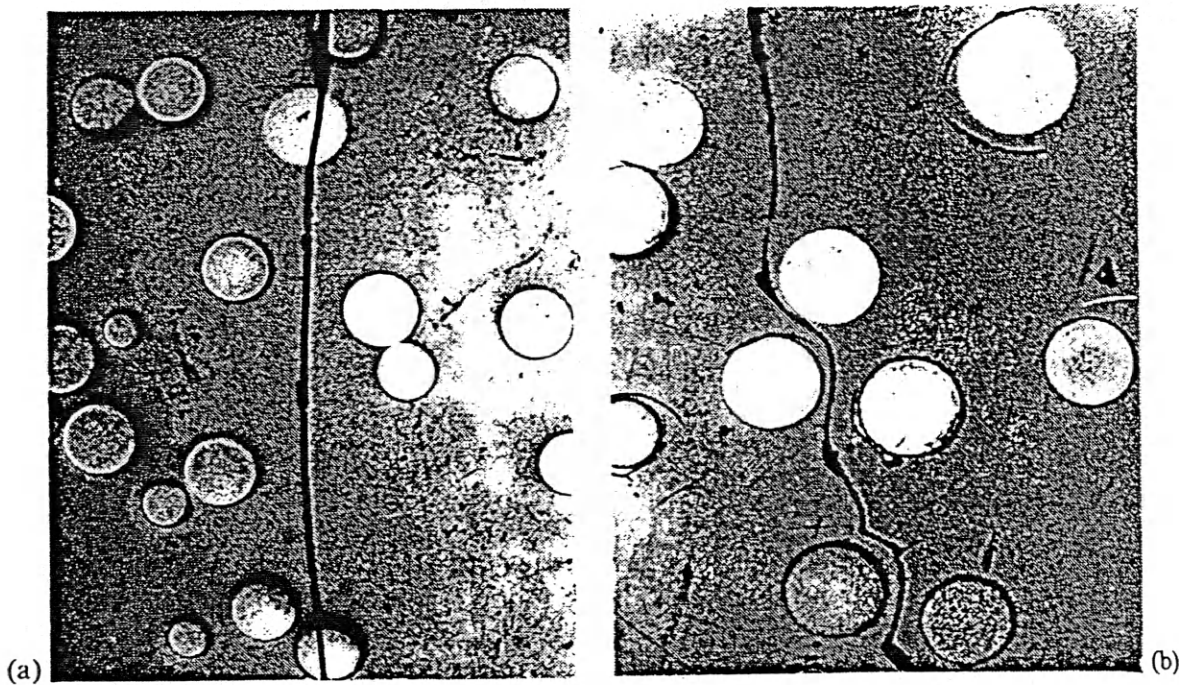


Figure 2.2. Thoria spheres in a glass matrix. (a) TCE glass > TCE thoria; (b) TCE thoria > TCE glass [35].

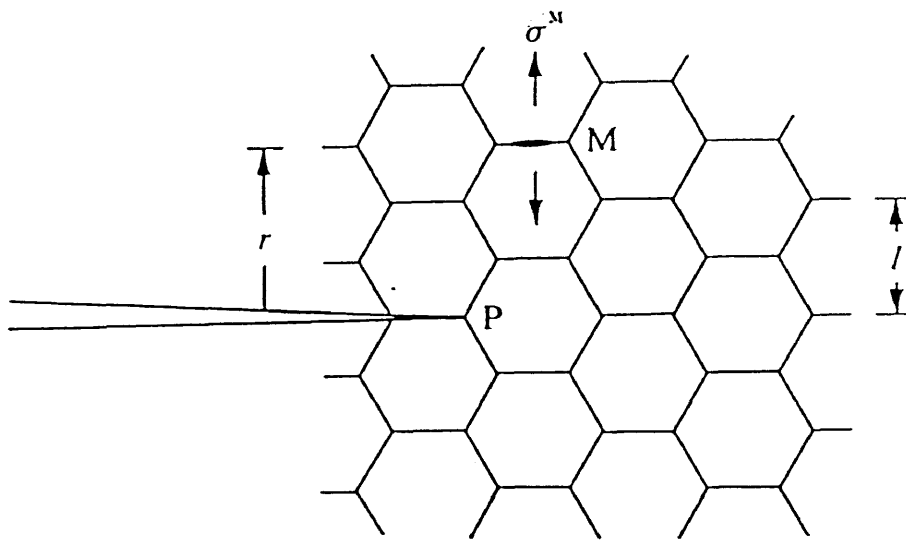


Figure 2.3. A schematic representation of the effect of microcracks on the propagation of cracks [35].

#### 2.4. The BaO-Al<sub>2</sub>O<sub>3</sub>-SiO<sub>2</sub> System

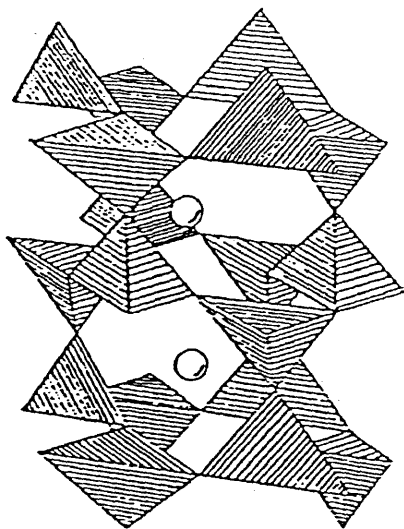
The alkaline earth feldspar composition BaAl<sub>2</sub>Si<sub>2</sub>O<sub>8</sub> has attracted an extensive amount of interest over the past several decades. It is valuable to various materials science fields due to its dielectric properties, high temperature stability, thermal expansion, and corrosion resistance [36,37]. In specific, the BaAl<sub>2</sub>Si<sub>2</sub>O<sub>8</sub> phase, has been used in such applications as dielectric glass-ceramics, refractories, commercial tableware, and ceramic-matrix composites [36-38]. The present research utilizes the wide range of thermal expansion present in the BaO-Al<sub>2</sub>O<sub>3</sub>-SiO<sub>2</sub> glass system, to satisfy the six thermal expansion mismatch models. To do this two crystalline polymorphs of BaAl<sub>2</sub>Si<sub>2</sub>O<sub>8</sub>, celsian and hexacelsian, were used.



The polymorphs celsian and hexacelsian are both described by the chemistry BaAl<sub>2</sub>Si<sub>2</sub>O<sub>8</sub>. Each phase contains its own unique set of properties. Celsian is

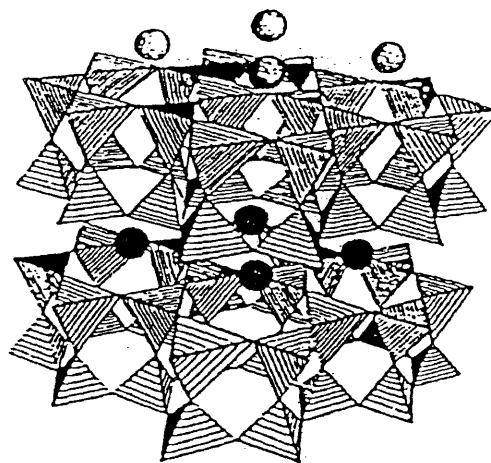
monoclinic in structure (see Figure 2.4), and can best be described as a feldspar structure in which all four vertices of the silica tetrahedra are shared, forming a three-dimensional network. The Al atoms substitute for the Si atoms with the charge compensated by the Ba atoms in the larger interstices of the structure [39]. Celsian is stable at temperatures less than 1590°C, and metastable above such temperatures until melting at 1760°C [40]. The thermal expansion of celsian is 2.7 ppm/°C from 20-1000°C [8], which makes it an ideal candidate for satisfying models where the TCE of the crystalline phase must be low.

Hexacelsian on the other hand is hexagonal in structure (see Figure 2.5), and can be described as infinite two-dimensional hexagonal sheets consisting of two layers of silica tetrahedra sharing all four vertices. Al atoms substitute for Si atoms in these tetrahedra, and the charge is compensated by the Ba atoms between sheets [38]. Hexacelsian is metastable at temperatures below 1590°C, and stable above such temperatures [40]. The thermal expansion of hexacelsian is 8.0 ppm/°C from 300-1000°C [8], which makes it an ideal candidate for satisfying models where the TCE of the crystalline phase must be high.

Several authors have reviewed the crystallization behavior of stoichiometric  $\text{BaAl}_2\text{Si}_2\text{O}_8$  glasses [8,36-44]. In such glasses, hexacelsian crystallizes first [8]. Then at temperatures of about 1590°C a hexacelsian to celsian transformation occurs [41,43]. There is a kinetic barrier to the nucleation of the celsian phase from hexacelsian. Bahat measured the heat of this transformation to be 20 kcal/mole [41]. Corral and Verduch, however, confirmed that this heat of transformation can be reduced when a solid solution of silica and hexacelsian is present [44]. Much emphasis has gone into trying to speed the transformation, or avoiding it all together. Such work entails novel processing and nucleating agents [37]. The effect of alumina on the crystallization behavior is unknown and will be a main emphasis of this work.



  $(Si, Al)O_4$  Tetrahedron  
 Ba





  $(Si, Al)O_4$  Tetrahedron  
 Ba

Figure 2.4. Structure of celsian [39].

Figure 2.5. Structure of hexacelsian [38].

### **CHAPTER 3.**

#### **PHASE 1: QUALITATIVE CRYSTALLIZATION BEHAVIOR OF BaO-Al<sub>2</sub>O<sub>3</sub>-SiO<sub>2</sub> GLASSES IN ALUMINA CERAMICS**

The objective of this phase of the work was to analyze the crystallization behavior of a number of barium aluminosilicate compositions to determine the potential of utilizing these compositions for thermal expansion mismatch models. Section one of this chapter will outline the compositions evaluated. Section two will present the experimental procedure used in the preparation of samples, while section three provides the method in which they were analyzed. This will be followed by the results of the qualitative x-ray diffraction analysis in section four and concluded by a summary in section five.

#### **3.1 Compositions Evaluated**

Three barium aluminosilicate compositions were selected, as listed in Table 3.1. All three compositions occur along the lowest melting region of this system as shown in the BaO-Al<sub>2</sub>O<sub>3</sub>-SiO<sub>2</sub> phase diagram in Figure 3.1. This phase diagram is composed of two separate diagrams separated by the line between Al<sub>2</sub>O<sub>3</sub> and BaSi<sub>2</sub>O<sub>5</sub>. This composite phase diagram was constructed because recent revisions have significantly changed section A of the phase diagram. No revisions were made for section B, therefore the original phase diagram was used. The resultant composite diagram allows for all the compositions to be analyzed utilizing the most recent data available.

The compositions listed in Table 3.1 and shown in Figure 3.1 were selected for the following reasons. They all exhibit low melting temperatures that make glass processing much more feasible and cost effective. Each composition has approximately the same alumina content, so trends in crystallization can be studied as a function of  $\text{SiO}_2/\text{BaO}$  ratio (or composition). The low alumina content allows for the study of alumina dissolution into the glass during firing (discussed in Chapter 4).

Composition 3 has a  $\text{SiO}_2/\text{BaO}$  molar ratio of 2.0; the same as celsian or hexacelsian  $\text{BaAl}_2\text{Si}_2\text{O}_8$ . Thus if this composition is used as an intergranular glass composition in an alumina ceramic, and alumina dissolves into the glass during firing, then the glass composition will shift toward the celsian composition. Compositions 2 and 4 have higher and lower  $\text{SiO}_2/\text{BaO}$  ratios compared to celsian. As celsian crystallizes in these compositions, the residual glass compositions will concentrate in  $\text{SiO}_2$  in composition 2 and in  $\text{BaO}$  in composition 4. This will potentially cause the thermal expansion of the residual glass in composition 2 to be lower than that of alumina. In composition 4 the thermal expansion of the residual glass will be higher than that of alumina.

Table 3.1. Initial Barium Aluminosilicate Compositions

Composition	<i>Weight Percent</i>			<i>Mole Percent</i>		
	2	3	4	2	3	4
$\text{SiO}_2$	55.3	40.0	32.0	74.0	61.1	52.8
$\text{Al}_2\text{O}_3$	9.5	10.0	10.0	7.5	9.0	9.7
$\text{BaO}$	35.2	50.0	58.0	18.5	29.9	37.5
$\text{SiO}_2/\text{BaO}$	-----	-----	-----	4.0	2.0	1.4

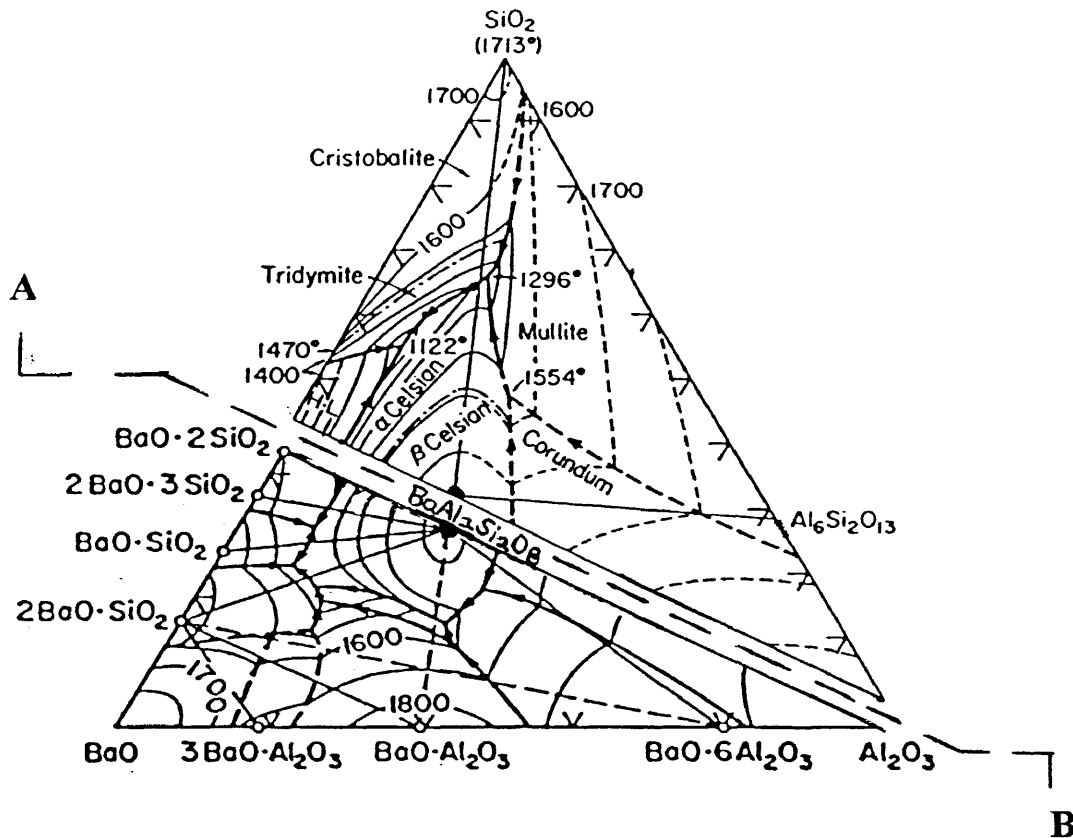


Figure 3.1. BaO-Al<sub>2</sub>O<sub>3</sub>-SiO<sub>2</sub> Phase Diagram

●: Composition 2; ■: Composition 3; ◆: Composition 4.

This phase diagram is composed of two separate diagrams. Sections A and B are from References 43 and 45 respectively.

The amount of celsian that can crystallize in the initial glass compositions is limited by the relatively small amount of alumina. However, when these compositions are used as an intergranular glass composition in a high alumina ceramic, there is effectively an unlimited supply of alumina that dissolves into the glass. The amounts of celsian crystallization and alumina dissolution will be discussed in Chapter 5.

All the compositions chosen in Table 3.1 were modified for this investigation with one mole percent sodium oxide to increase the wetting behavior of these compositions with alumina. In addition, the compositions were evaluated with and without two mole percent  $\text{MoO}_3$ , which was added as a nucleating agent. This resulted in six compositions as listed in Table 3.2. The subscripts "a" and "b" refer to zero and two mole percent  $\text{MoO}_3$  addition respectively. The  $\text{BaO}$ ,  $\text{Al}_2\text{O}_3$ , and  $\text{SiO}_2$  ratios in these compositions are the same as in Table 3.1.

Table 3.2. Compositions Evaluated

Composition	<i>Weight Percent</i>					
	2a	2b	3a	3b	4a	4b
$\text{SiO}_2$	54.87	52.93	39.73	38.49	31.80	30.88
$\text{Al}_2\text{O}_3$	9.43	9.09	9.93	9.62	9.94	9.65
$\text{BaO}$	34.93	33.69	49.66	48.11	57.64	55.97
$\text{Na}_2\text{O}$	0.77	0.76	0.68	0.67	0.63	0.62
$\text{MoO}_3$	----	3.53	----	3.11	----	2.89

Composition	<i>Mole Percent</i>					
	2a	2b	3a	3b	4a	4b
$\text{SiO}_2$	73.30	71.82	60.47	59.25	52.26	51.21
$\text{Al}_2\text{O}_3$	7.42	7.27	8.91	8.73	9.63	9.43
$\text{BaO}$	18.28	17.91	29.62	29.02	37.11	36.37
$\text{Na}_2\text{O}$	1.00	1.00	1.00	1.00	1.00	1.00
$\text{MoO}_3$	----	2.00	----	2.00	----	2.00



## **3.2 Experimental Methodology**

### **3.2.1 Preparation of Glass Powders**

The compositions listed in Table 3.2 were prepared from raw materials of  $\text{BaCO}_3$ ,  $\text{Na}_2\text{CO}_3$ ,  $\text{SiO}_2$ ,  $\text{Al}_2\text{O}_3$ , and  $\text{MoO}_3$ . The compositions were batched using a computer spreadsheet based on a batch weight of 60 grams. Two 60 gram batches were weighed out for each composition to  $\pm 0.05$  grams. The batches were then mixed for 20 hours by dry ball milling in a plastic jar with four alumina balls. All 120 grams of each batch were then melted in a platinum 10% rhodium crucible at  $1590^\circ\text{C}$  for one hour, and then water quenched. The liquid was held for one hour to ensure carbonate removal was complete and that uniformity through the sample was achieved.

The glass frit obtained after quenching was ball milled with 1000 grams of balls and 500 milliliters of water for 24 hours. The milled glass and water were poured through a 325 mesh sieve to separate out large unmilled glass particles and the milling balls. The glass powder/water slurry was then pan dried for 24 hours in an oven at  $100^\circ\text{C}$ . The resulting particle size from SEM analysis was within  $1\text{-}10\mu\text{m}$ . The glass powders were characterized by x-ray diffraction to ensure that they were amorphous.

### **3.2.2. Addition of Alumina to Glass Powders**

To study the crystallization behavior of each composition as a function of crystalline alumina addition, mixtures of the glass powders with 0, 50, and 96 weight percent crystalline alumina were initially prepared for all compositions in Table 3.2. Upon

preliminary qualitative and quantitative x-ray diffraction analysis, mixtures of glass powders 2a, 3a, 3b, and 4a were prepared with 75 weight percent crystalline alumina addition. Preliminary findings suggested little difference between the "a" and "b" compositions except for 3a and 3b.

Glass/alumina mixtures were weighed out on a 200, 100, and 50 gram basis to +/- 0.5 grams for 96, 75, and 50 weight percent crystalline alumina addition respectively. The powders were then mixed in 1000 milliliter plastic jars for 24 hours. Each jar contained 30 volume percent additions of alumina balls and water each. The mixed slurry was then poured through a 325 mesh sieve and pan dried in an oven at 100°C for 24 hours.

### **3.2.3. Forming and Sintering**

Pellets of each composition were prepared by pressing two grams of powder in a 1.3 cm (0.5 in) diameter die at 68.9 MPa (10,000 psi) for one minute. This procedure yielded an approximate green density of 55 percent of the theoretical density. This value did not vary as a function of pressing load ( from 10,000 to 40,000 psi).

Two firing/heat treatment experiments were conducted; (1) a preliminary characterization and (2) a detailed crystallization analysis. In both cases two pellets of each composition were prepared to allow for enough material for qualitative and quantitative x-ray diffraction analysis. The preliminary analysis involved the heat treatment of all six compositions in Table 3.2 mixed with 0, 50, and 96 weight percent alumina. Heat treatment temperatures for the preliminary analysis are presented in Table 3.3 indicated without an asterisk. Heating and cooling rates were 3°C/min with a

one hour hold. The preliminary characterization also involved one additional heat treatment of all glass compositions with 96 weight percent alumina addition. This entailed a ramp of 3°C/min to 1640°C with a hold for one hour, followed by a cool down at 3°C/min to 1000°C and a hold for one hour. The samples were then cooled at 3°C/min to room temperature.

Preliminary results indicated that there was little difference between the crystallization behavior of compositions 2a and 2b, and between 4a and 4b. Therefore detailed characterization was performed only on compositions 2a, 3a, 3b, and 4a. The alumina additions investigated included 0, 50, 75, and 96 weight percent. The firing/heat treatment conditions for this characterization are also summarized in Table 3.3, indicated by an asterisk.

Table 3.3 Firing Temperatures (°C)

<i>Weight Percent Crystalline Alumina</i>				
0%	50%	75%	96%	
1000	1000	---	---	
1100	1100	1100*	1100*	
---	1340*	1340*	1340*	
---	1540*	1540*	1540*	
---	---	1640*	1640	

\* Compositions 2a, 3a, 3b, 4a only.

### 3.3. Analytical Methodology: Qualitative X-Ray Diffraction of Samples

Samples were qualitatively examined; (1) to ensure that the glass powders were amorphous, and (2) to study the crystallization that occurred. All samples were prepared for x-ray diffraction in the following manner. The pellets were first ground into fine powder. Approximately 0.5 grams of this powder was then placed on a glass slide with two to three drops of a 1:20 volume percent collodion:methanol solution. The resultant slurry was then evenly distributed on the slide and allowed to dry, forming a film. This method removed errors encountered due to sample thickness and provided repetitive results. The samples were characterized with a computerized Rigaku X-Ray Unit. The samples were exposed to Cu K $\alpha$  radiation and scanned from 10-70 $^{\circ}$  of 2 $\theta$  with a step size of 0.05 $^{\circ}$  2 $\theta$  and a one second count time. Analysis of the phases present after heat treatment was conducted by comparison with x-ray diffraction cards published by the Joint Committee on Powder Diffraction Standards (JCPDS). Also computational search methods of such cards were utilized. The search was provided by Tony Gallagher of Ricerca, Inc., 7528 Auburn Road, P.O. Box 1000, Painsville, Ohio 44077-1000.

### 3.4 Results and Discussion

The x-ray diffraction results indicate that the glass powders were amorphous except for composition 2b. This composition crystallized quite rapidly upon quenching. The crystalline phase does not appear to match any of the JCPDS cards, and this was classified as unknown.

The x-ray diffraction patterns of the fired samples with 0 and 50 weight percent crystalline alumina additions are plotted in Figures 3.1 (a) - (f), and for 96 weight percent crystalline alumina addition in Figure 3.2 (a) - (c). The samples with 0 and 50 weight percent alumina crystallized three main phases: hexacelsian, celsian, and barium silicate( $\text{BaSiO}_3$ ), as shown in Figure 3.1. The crystalline phases present in each of these preliminary compositions are summarized in Table 3.4. Crystalline alumina peaks were observed in the samples without alumina addition, which resulted from ball milling contamination. Hexacelsian was the dominant crystalline phase present. Firing temperature (only considering the range studied), presence of nucleating agent, and alumina addition had no observable effect on the presence of hexacelsian.

Table 3.4 Qualitative Results: Preliminary Analysis

H= Hexacelsian; C=Celsian; M=Mullite; BS=  $\text{BaSiO}_3$ ; A= Alumina; U=Unknown

Composition	1000°C	1100°C	1000°C	1100°C	1640°C	1640/1000°C
	0% $\text{Al}_2\text{O}_3$	0% $\text{Al}_2\text{O}_3$	50% $\text{Al}_2\text{O}_3$	50% $\text{Al}_2\text{O}_3$	96% $\text{Al}_2\text{O}_3$	96% $\text{Al}_2\text{O}_3$
2a	H-A	H-A	H-A	H-A	C-M-A	C-M-A
2b	H-U-A	H-U-A	H-U-A	H-U-A	C-M-A	C-M-A
3a	H-C-A	H-C-A	H-C-A	H-C-A	H-C-M-A	H-C-M-A
3b	H-C-A	H-C-A	H-C-A	H-C-A	C-M-A	C-M-A
4a	H-BS-A	H-BS-A	H-BS-A	H-BS-A	H-A	H-A
4b	H-BS-A	H-BS-A	H-A	H-A	H-A	H-A

In contrast to the 0 and 50 percent alumina samples, the 96 percent alumina samples were not all dominated by hexacelsian. The introduction of a second hold on cooling at 1000°C did not affect the crystallization behavior, and their x-ray diffraction patterns are included in Figures 3.2(a)-(c). In the high silica content glasses (2a and 2b)

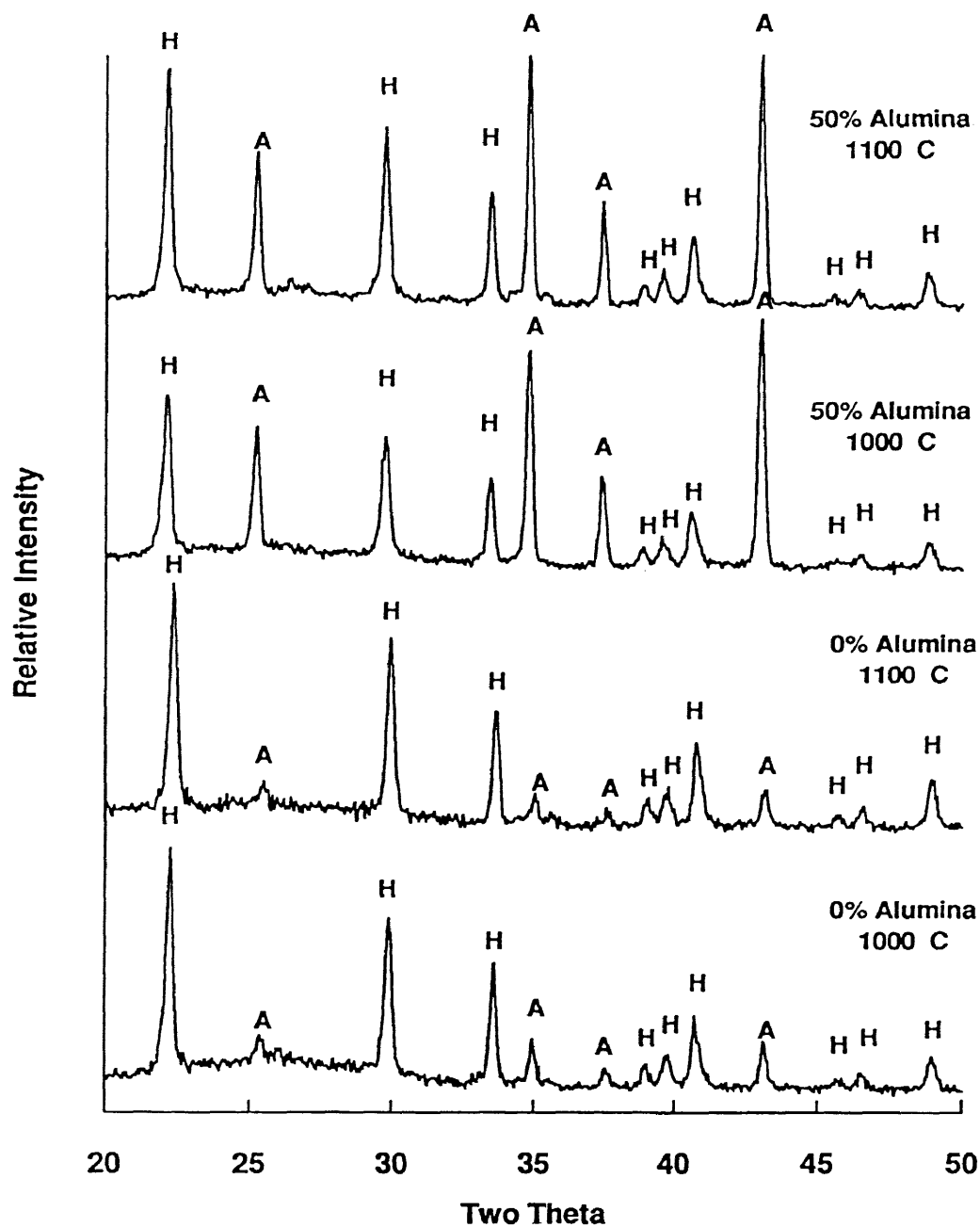


Figure 3.2(a). Qualitative x-ray diffraction patterns for composition 2a with 0 and 50 percent alumina addition. H=Hexacelsian; A=Corundum.

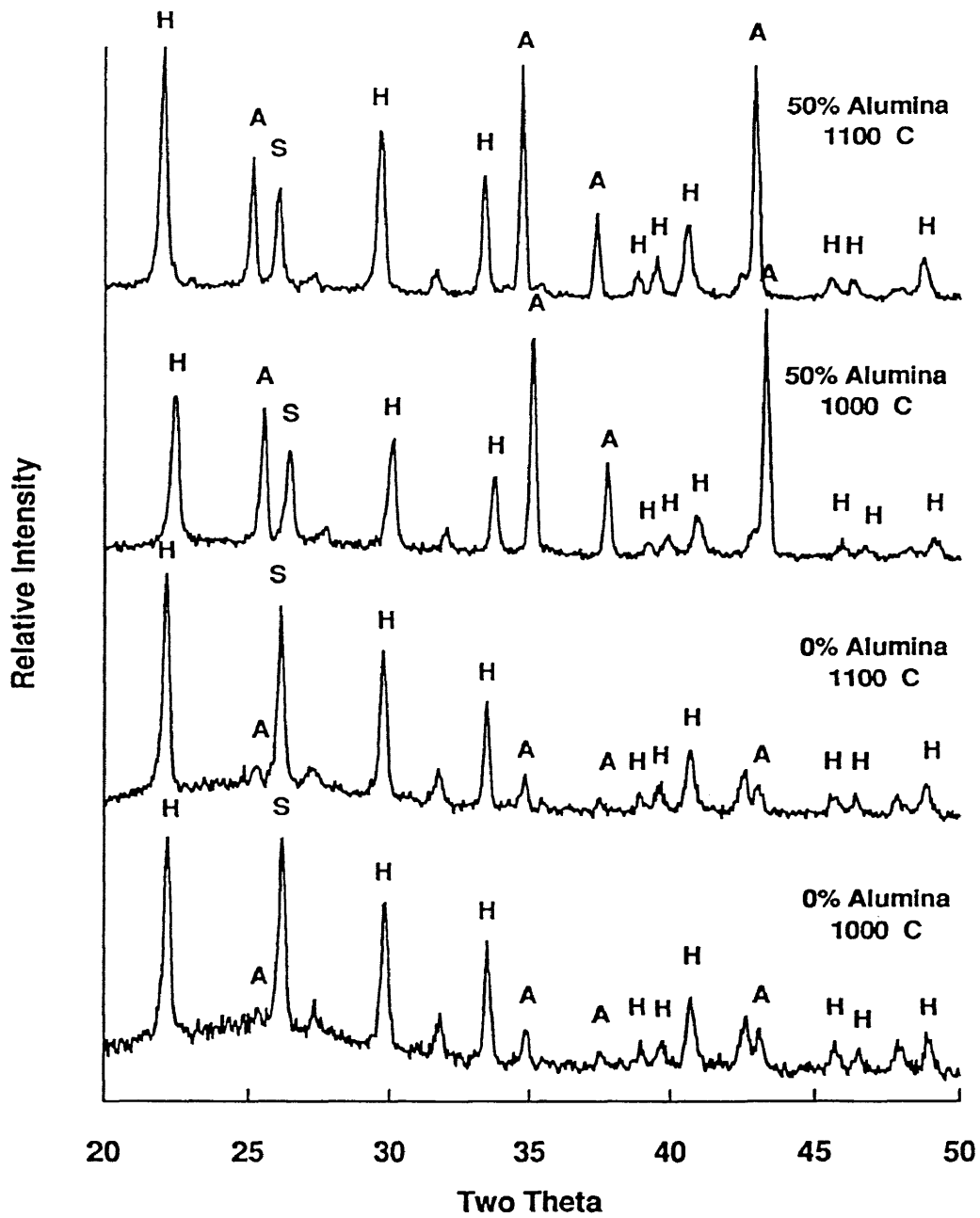


Figure 3.2(b). Qualitative x-ray diffraction patterns for composition 2b with 0 and 50 percent alumina addition. H=Hexacelsian; A=Corundum; S= ?.

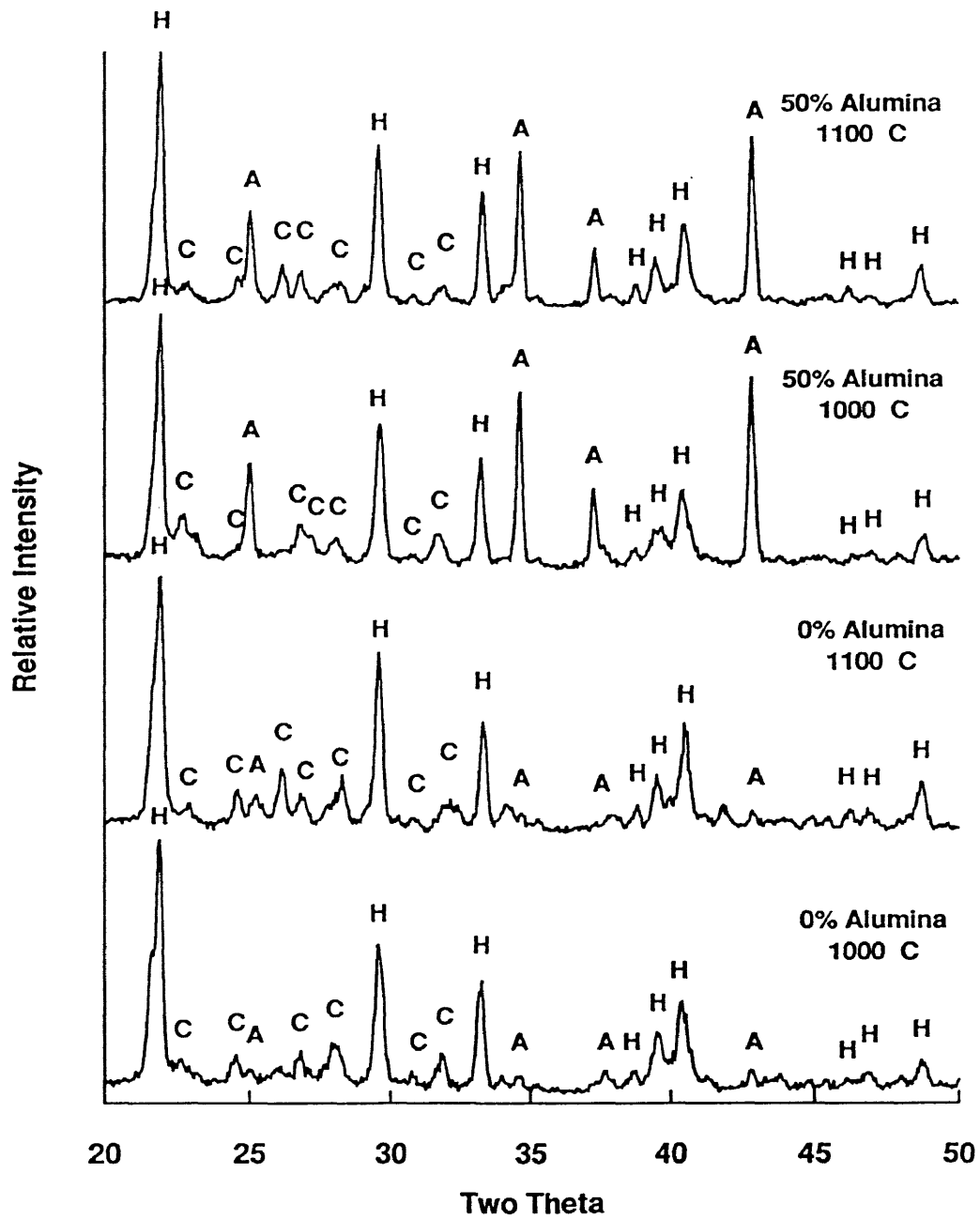


Figure 3.2(c). Qualitative x-ray diffraction patterns for composition 3a with 0 and 50 percent alumina addition. H=Hexacelsian; C=Celsian; A=Corundum.



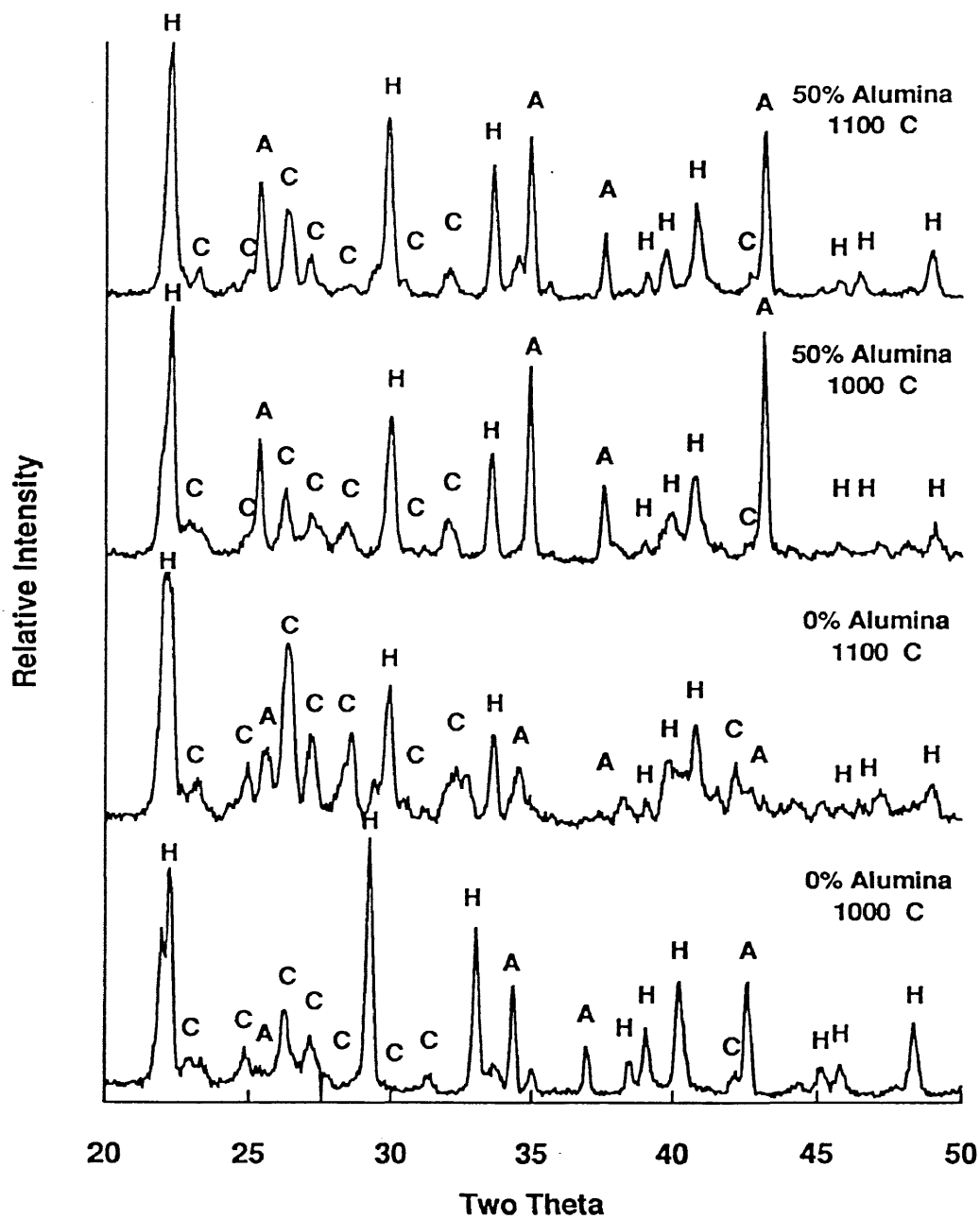


Figure 3.2(d). Qualitative x-ray diffraction patterns for composition 3b with 0 and 50 percent alumina addition. H=Hexacelsian; C=Celsian; A=Corundum.

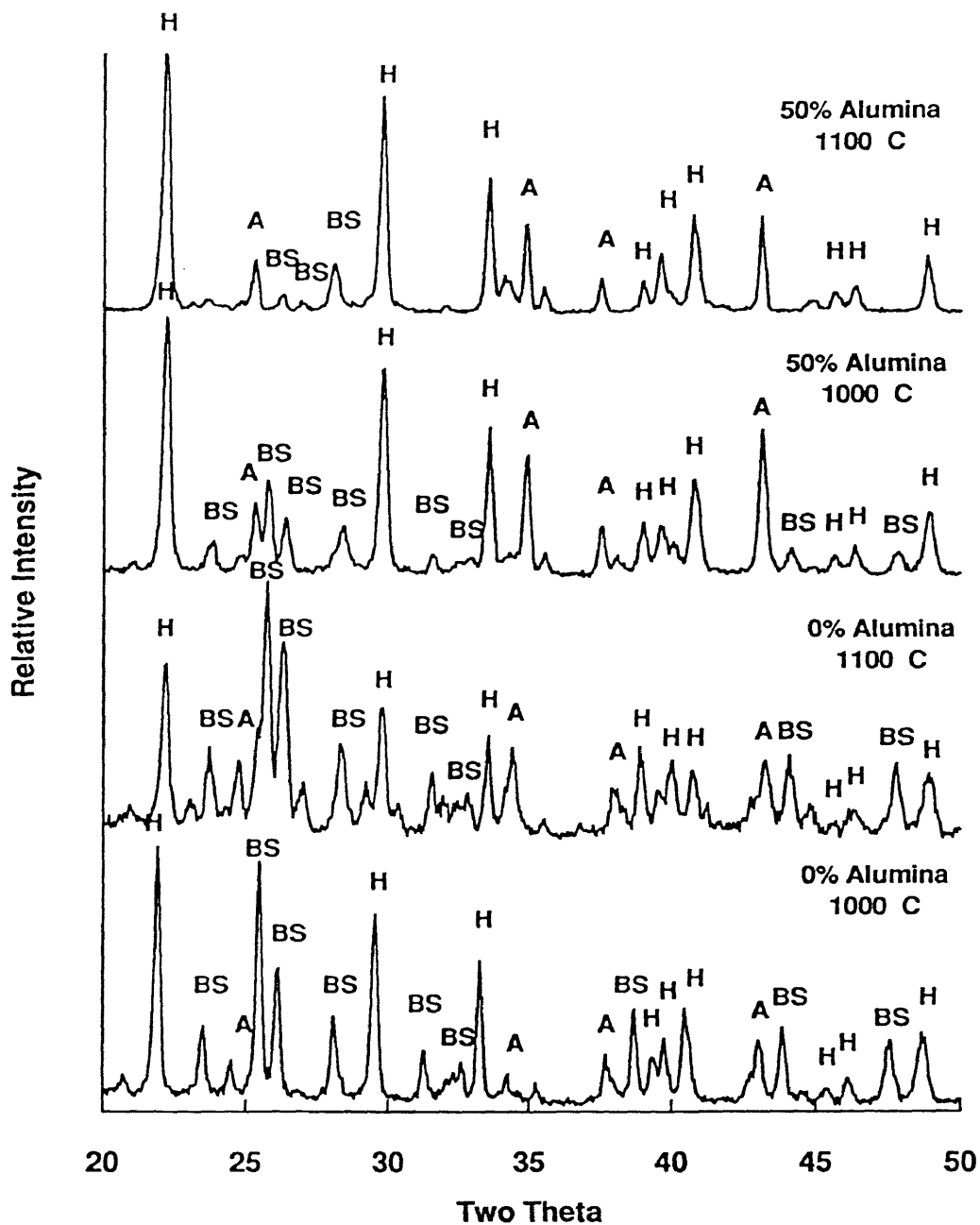


Figure 3.2 (e). Qualitative x-ray diffraction patterns for composition 4a with 0 and 50 percent alumina addition. H=Hexacelsian; BS=BaSiO<sub>3</sub>; A=Corundum.

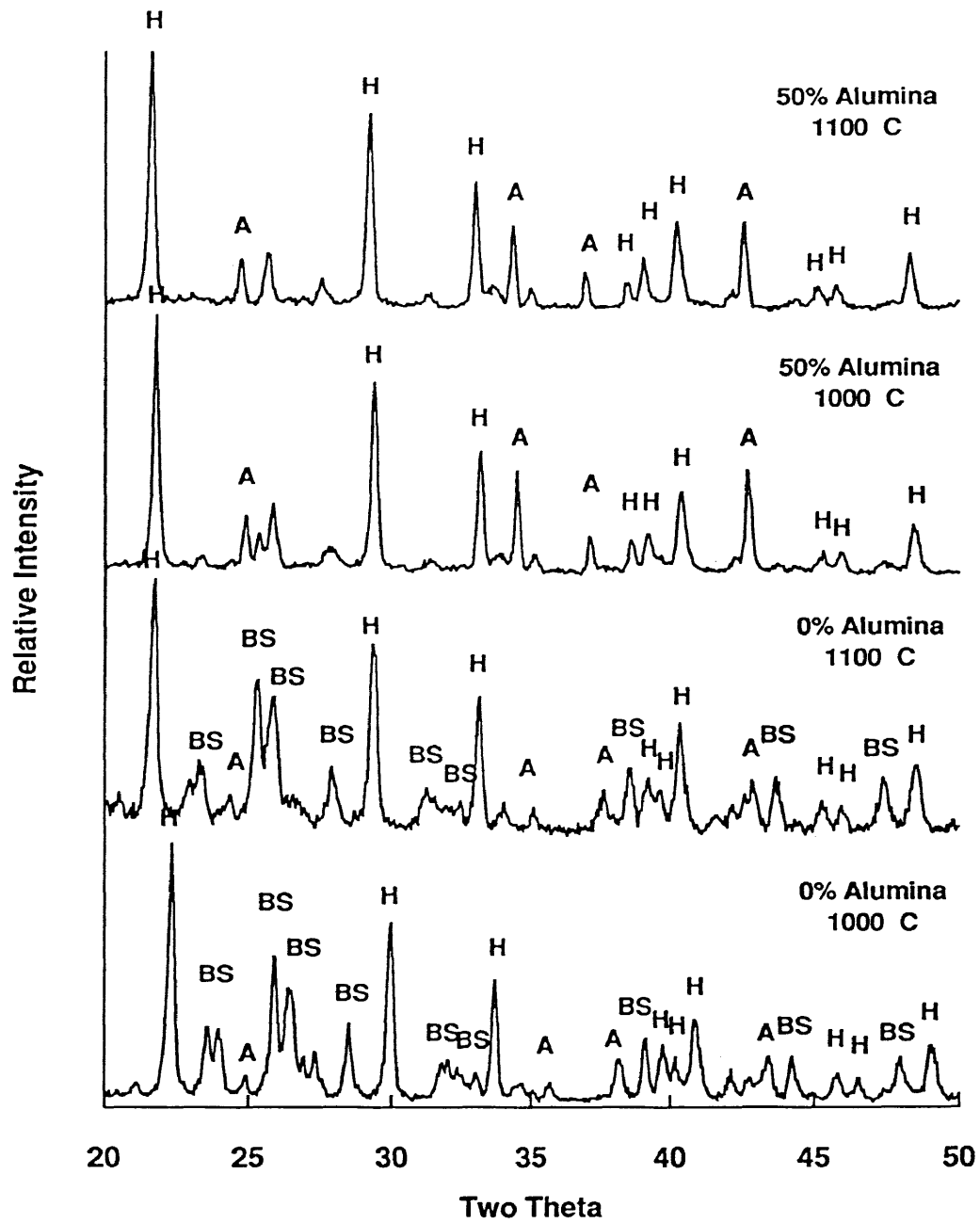


Figure 3.2 (f). Qualitative x-ray diffraction patterns for composition 4b with 0 and 50 percent alumina addition. H=Hexacelsian; BS=BaSiO<sub>3</sub>; A=Corundum.

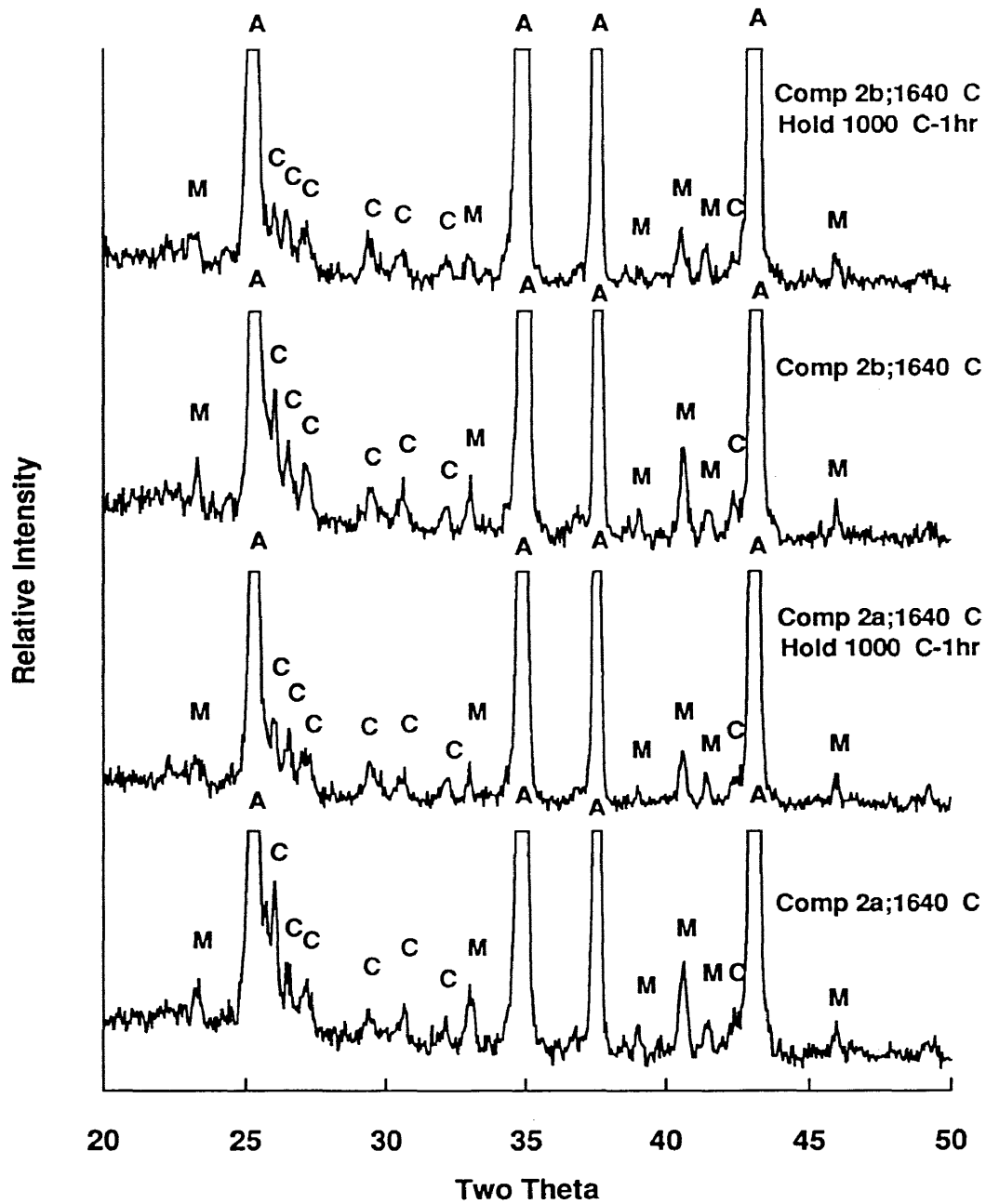


Figure 3.3 (a). Qualitative x-ray diffraction patterns for composition 2 with 96 percent alumina addition. C=Celsian; M=Mullite; A=Corundum.

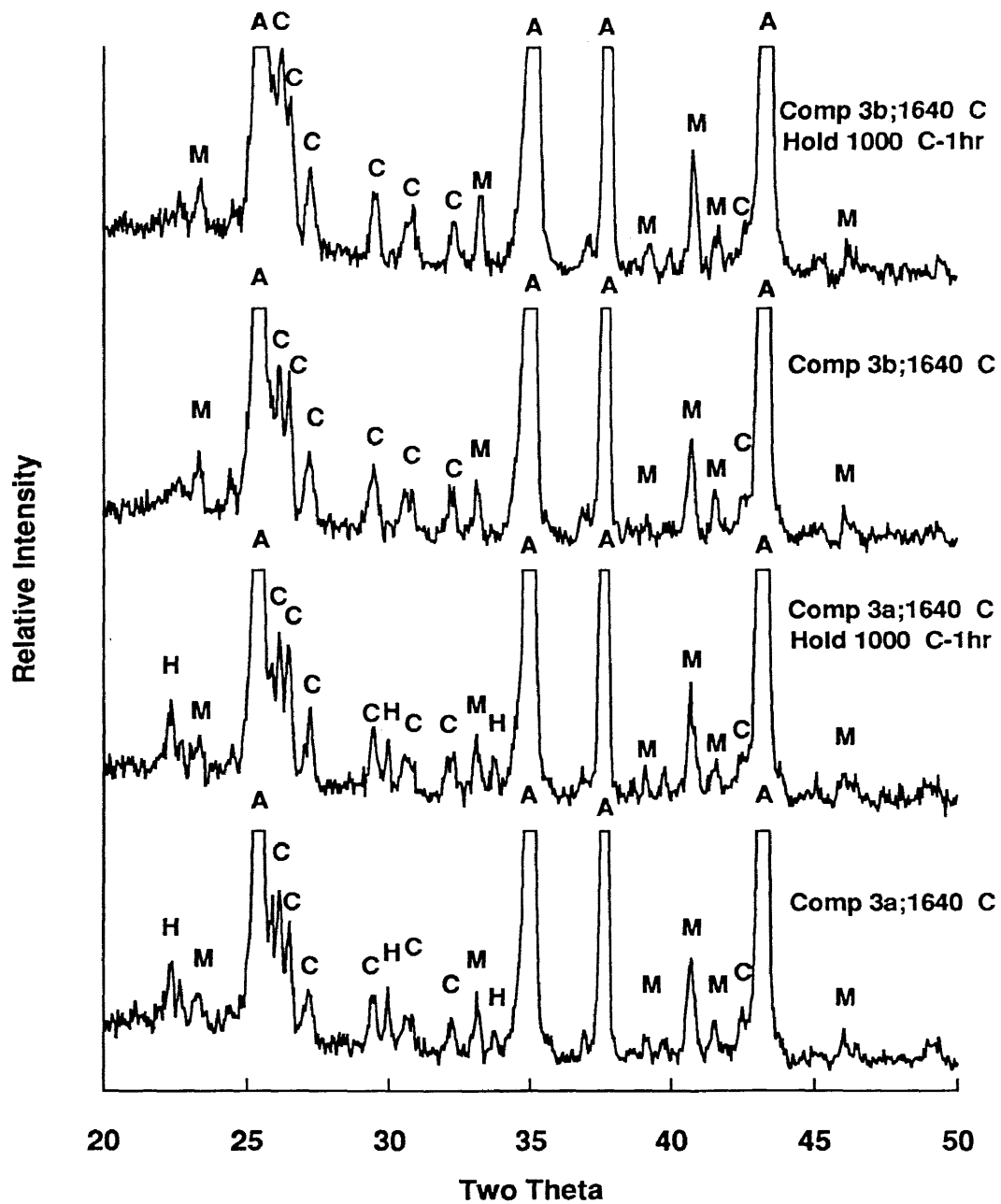


Figure 3.3 (b). Qualitative x-ray diffraction patterns for composition 3 with 96 percent alumina addition. C=Celsian; M=Mullite; A=Corundum; H=Hexacelsian.

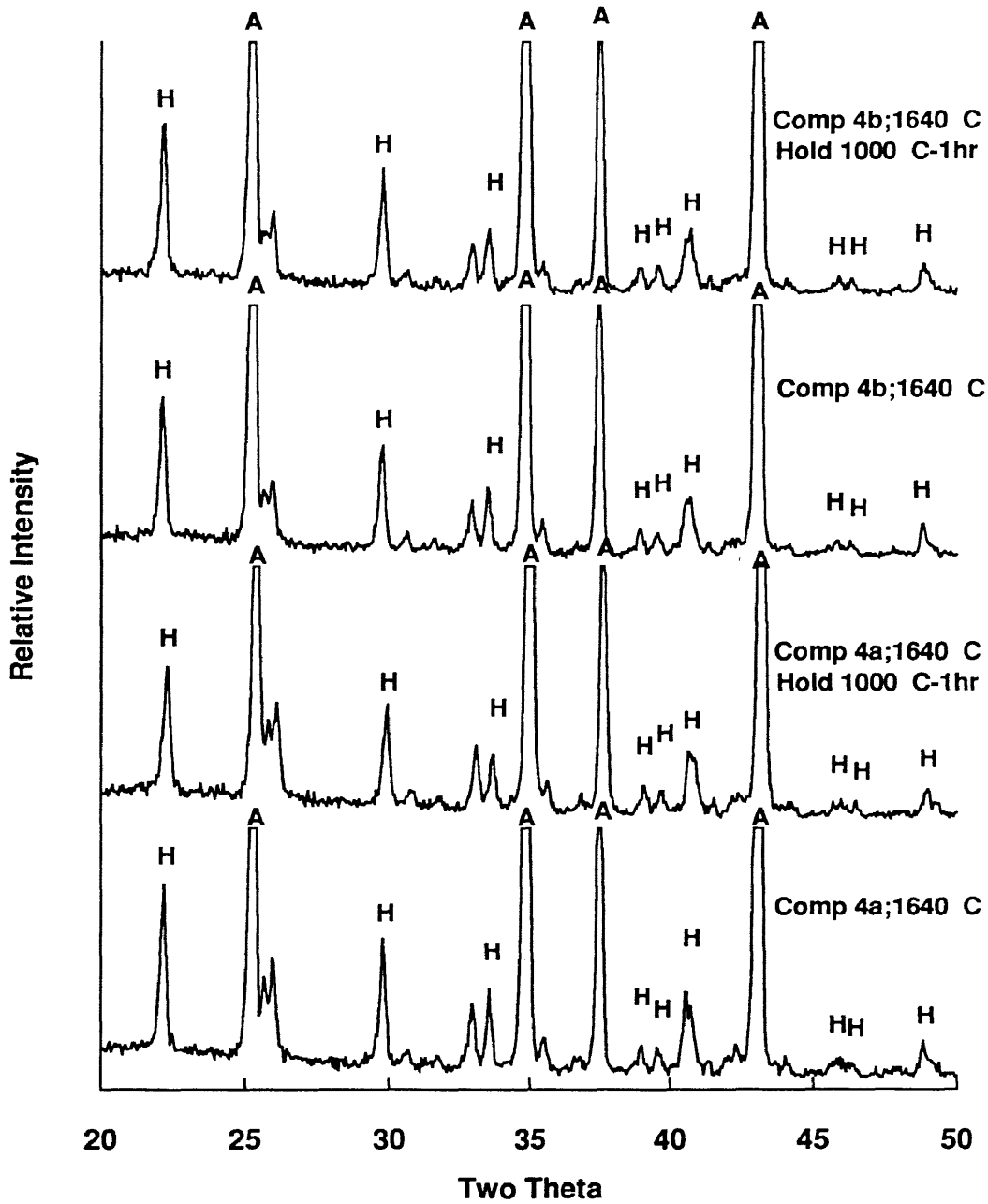


Figure 3.3 (c). Qualitative x-ray diffraction patterns for composition 4 with 96 percent alumina addition. H=Hexacelsian; A=Corundum.

celsian and mullite crystallized, and do not appear to be significantly affected by the addition of the nucleating agent  $\text{MoO}_3$ . In the low silica content glasses (4a and 4b) hexacelsian was the only phase that crystallized, and again the  $\text{MoO}_3$  did not appear to affect the crystallization behavior. In the intermediate silica content glasses (3a and 3b) an interesting phenomenon occurred. In composition 3a, hexacelsian, celsian, and mullite crystallized. In 3b, with  $\text{MoO}_3$  nucleating agent addition, hexacelsian did not crystallize.

These preliminary results indicated that no significant difference in crystallization behavior occurred between compositions 2a and 2b, and 4a and 4b. Therefore, only compositions 2a, 3a, 3b, and 4a were further investigated. Additional characterization of the crystallization behavior of these compositions was performed. This characterization included additional samples with 75 weight percent alumina addition and additional firing temperatures.

Table 3.5 summarizes the results of the crystallization behavior of compositions 2a, 3a, 3b, and 4a from the additional studies and the preliminary analysis.

Table 3.5. Summary of qualitative results, detailed analysis.

H=Hexacelsian; C=Celsian; BS=  $\text{BaSiO}_3$ ; M=Mullite; A=Alumina

Composition	0% Alumina		50% Alumina			
	1000C	1100C	1000C	1100C	1340C	1540C
2a	H-A	H-A	H-A	H-A	H-C-A	H-C-A
3a	H-C-A	H-C-A	H-C-A	H-C-A	C-A	C-A
3b	H-C-A	H-C-A	H-C-A	H-C-A	C-A	C-A
4a	H-BS-A	H-BS-A	H-BS-A	H-BS-A	H-C-A	H-C-A

Table 3.5.(continued) Summary of qualitative results, detailed analysis.  
 H=Hexacelsian; C=Celsian; BS= BaSiO<sub>3</sub>; M=Mullite; A=Alumina

Composition	75 % Alumina				96% Alumina			
	1100C	1340C	1540C	1640C	1100C	1340C	1540C	1640C
2a	H-A	H-C-A	C-A	C-A	C-H-A	C-H-A	C-A	C-M-A
3a	H-C-A	C-A	C-A	H-A	C-H-A	C-H-A	C-A	H-C-M-A
3b	H-C-A	C-A	C-A	C-A	C-H-A	C-H-A	C-A	C-M-A
4a	H-C-A	H-A	H-C-A	H-A	H-A	H-A	C-H-A	H-A

As seen from these results, the only difference between compositions 3a and 3b occurred with 96 weight percent alumina addition fired at a temperature of 1640°C. With less alumina addition and /or lower firing temperatures, the addition of MoO<sub>3</sub> had no significant effect on the crystallization behavior. The alumina addition, firing temperature, and composition on the other hand played a significant role. The detailed x-ray diffraction patterns may be found in Appendix A.

In the high silica content glass (2a) hexacelsian was the dominant phase after firing at low temperatures. As the firing temperature was increased mixtures of celsian and hexacelsian crystallized. At 1540°C celsian was the only crystalline phase present (with alumina), and at 1640°C celsian and mullite crystallized. Alumina additions less than 96 weight percent did not effect the crystallization behavior. With 96 weight percent alumina the samples fired at 1100 and 1640°C crystallized additional phases as indicated in Table 3.5.

In the intermediate silica content glass (3a) both celsian and hexacelsian crystallized. As the firing temperature was increased celsian dominated at 1340-1640°C



for all alumina additions except 96 weight percent. In the 96 weight percent alumina samples celsian crystallized along with hexacelsian and mullite at 1640°C.

The crystallization behavior of the low silica content glass (4a) was dominated throughout by hexacelsian. At low firing temperatures and alumina addition  $\text{BaSiO}_3$  also crystallized. The  $\text{BaSiO}_3$  disappeared as the firing temperature and alumina content increased. This indicated that the presence of alumina in the glass, supplied through dissolution, inhibits the crystallization of  $\text{BaSiO}_3$ . After firing at 1540°C both celsian and hexacelsian crystallized but hexacelsian dominated at 1640°C. As the alumina content was increased, the presence of hexacelsian also increased.

### 3.5. Summary and Conclusions

X-ray diffraction was used to qualitatively analyze the crystallization behavior of various compositions as a function of firing temperature and alumina addition. The effect of the addition of a nucleating agent was also analyzed. The results show that the nucleating agent,  $\text{MoO}_3$ , did not change the crystallization characteristics of the base compositions. In the low  $\text{SiO}_2$  content glass fired at low temperatures, hexacelsian was the dominant crystalline phase. Firing between 1340 and 1640°C resulted in celsian as the dominant phase, especially for the intermediate  $\text{SiO}_2$  content glasses. Above 1640°C hexacelsian was the dominant phase in the low  $\text{SiO}_2$  glasses, while mullite and celsian dominated in all other compositions.

The results show that there is potential use of these compositions in thermal mismatch modeling. In 96 weight percent alumina samples crystalline phases with thermal expansion coefficients higher or lower (hexacelsian or celsian) than that of alumina may be

attained. The thermal expansion of the glass phase in these high alumina samples is not known. Quantitative x-ray diffraction analysis will provide a method of determining the composition of the glass phase, whereby the thermal expansion can be calculated. The next chapter describes quantitative x-ray diffraction analysis conducted for this purpose.

## **CHAPTER 4**

### **PHASE 2: QUANTITATIVE CRYSTALLIZATION AND ALUMINA DISSOLUTION BEHAVIOR OF BaO-Al<sub>2</sub>O<sub>3</sub>-SiO<sub>2</sub> GLASSES IN ALUMINA CERAMICS**

In phase one of this research the crystallization behavior of various barium aluminosilicate compositions was qualitatively analyzed as discussed in Chapter Three. The data obtained indicated the potential of forming a variety of crystalline phase and residual glass combinations that could be used as a basis for thermal expansion mismatch modeling. Thus phase two of this research was conducted to quantify the crystallization behavior and residual glass compositions along with the dissolution of alumina as a function of temperature, alumina addition, and SiO<sub>2</sub>/Al<sub>2</sub>O<sub>3</sub> ratio. By determining the amount of alumina dissolution into the glass and crystalline phases, the composition and TCE of the glass phase was attained for modeling the types of TCE mismatch. In the first section of this chapter the compositions and experimental methodology by which these compositions were attained and prepared for analysis will be presented. In sections two to four the analytical methodologies of quantitative x-ray diffraction, alumina dissolution analysis, and density evaluation will be discussed respectively. The analytical results will be presented in section five followed by conclusions and a subsection discussing transient glass phase processing in section six.

#### 4.1 Compositions Evaluated and Experimental Methodology

The crystallization behavior of compositions 2a, 3a, 3b and 4a was characterized by quantitative x-ray diffraction. The qualitative work, described in the last chapter, analyzed the crystallization behavior of the above compositions as a function of composition, alumina addition, processing temperature, and presence of nucleating agent. The crystallization behavior was mainly dependent upon composition, temperature, and alumina addition. This work showed that there was little difference in the crystallization behavior of compositions with and without the addition of  $\text{MoO}_3$  as a nucleating agent, except for composition 3 with 96 weight percent alumina addition fired at high temperatures. Therefore the quantitative x-ray diffraction was conducted on compositions 2a, 3a, 3b, and 4a.

To study the quantitative crystallization behavior of each composition as a function of crystalline alumina addition, mixtures of glass powders with 0, 50, 75 and 96 weight percent crystalline alumina were prepared as described in Section 3.2. The crystallization was also studied as a function of composition ( $\text{SiO}_2/\text{BaO}$  ratio). For compositions 2, 3, and 4 the  $\text{SiO}_2/\text{BaO}$  ratios are 4.0, 2.0, and 1.4 respectively. The samples were then fired at temperatures presented in Table 3.3 for one hour, with heating and cooling rates of  $3^\circ\text{C}/\text{min}$ . This allowed for the study of crystallization as a function of temperature.

## 4.2. Analytical Methodology: Quantitative X-Ray Diffraction

### 4.2.1. The Matrix - Flushing Method

The method by which the phase percentages of most crystalline mixtures are quantitatively evaluated is known as the internal standard method [46]. This method shows that the intensity ratio of two crystalline phases is a linear function of the weight fraction of the crystalline phase being determined. The working equation is as follows.

$$I_{\alpha}/I_s = kW_{\alpha} \quad (\text{Eqn. 4.1})$$

$I_{\alpha}$  = Intensity of strongest peak of phase being determined.

$I_s$  = Intensity of strongest peak of standard.

$k$  = constant.

$W_{\alpha}$  = Weight fraction of phase being determined.

In order to observe this, a detailed calibration curve must be constructed from standards. This is a very time consuming process, and was deemed impractical for this work. Thus this research utilized a simple, modified internal standard method known as the matrix-flushing method [47].

The matrix-flushing method derives its simplicity from the fact that no complex calibration curves are needed. The intensity ratios are derived from the JCPDS cards. On many cards is a reference intensity ratio ( $I / I_{\text{COR}}$ ) of that phase compared to corundum ( $\alpha$  - alumina). By utilizing the respective  $I / I_{\text{COR}}$  values, an intensity ratio of two other crystalline phases can be determined since  $I_{\text{COR}}$  will cancel out as shown in Equation 4.2.

$$(I_{\alpha}/I_{\text{COR}})/(I_{\beta}/I_{\text{COR}}) = I_{\alpha}/I_{\beta} \quad (\text{Eqn. 4.2})$$

This ratio of reference intensities is equivalent to the linear constant in the internal standard method. This value may be utilized over a wide range of values due to the assumption that the calibration curve is linear and passes through the origin. Thus, the matrix-flushing method develops an exact relationship between intensity and concentration. The working equation is as follows.

$$X_i = X_f (k_f / k_i) (I_i / I_f) \quad (\text{Eqn. 4.3.})$$

$X_i$  = Weight fraction of the unknown phase.

$X_f$  = Quantity of standard.

$k_i$  = The intensity ratio ( $I/I_{\text{COR}}$ ) of the 100% peaks of the binary mixture of pure crystal phase and  $\alpha$  -  $\text{Al}_2\text{O}_3$ .

$k_f$  = The intensity ratio ( $I/I_{\text{COR}}$ ) of the 100% peaks of the binary mixture of pure standard and  $\alpha$  -  $\text{Al}_2\text{O}_3$ .

$I_i/I_f$  = Intensity ratio of the crystal phase to the standard in the given sample.

#### ***4.2.1a Multicomponent Analysis***

The primary utilization of this method was in the analysis of multicomponent samples. In such an analysis, a standard was selected and mixed in known quantity with the sample. Several x-ray diffraction runs were completed on the mixture. Utilizing the 100% peaks of all the samples, subsequent equations were set up (Eqn. 4.3.) for each sample, against the standard. In this manner a very difficult and time consuming project was simplified.

#### **4.2.1b Amorphous Phase Content Analysis**

An interesting feature of this matrix-flushing method is that it can be used to detect and determine the total amorphous material in a sample. The matrix-flushing method generally shows a large intensity imbalance between the crystalline phases when an amorphous phase is present. From Equation 4.3 and material balance, the amount of amorphous material can be obtained.

#### **4.2.1c Binary Mixture Analysis (Auto-Flushing)**

For any binary system an auto-flushing phenomenon emerges. The term auto-flushing means that no standard is needed to evaluate the quantity of crystalline phases present. In essence, each component serves as a standard for the other component. Let the weight fraction of two components of a binary mixture be  $X_1$  and  $X_2$ . From matrix-flushing theory we obtain the following equations.

$$X_1 + X_2 = 1 \quad (\text{Eqn. 4.4})$$

$$I_1/I_2 = (k_1/k_2) (X_1/X_2) \quad (\text{Eqn. 4.5})$$

Solving both equations simultaneously we find the following equation.

$$X_1 = \frac{1}{1 + (k_1/k_2) (I_2/I_1)} \quad (\text{Eqn. 4.6})$$

Therefore the quantitative composition of a binary system can easily be calculated from a function of the ratios of the reference intensities of each phase, as well as a function of the ratios of the relative intensities of the 100% peaks of each phase. The auto-flushing phenomenon was used in the 96 weight percent alumina samples to obtain the relative ratios of non-alumina crystalline phases. This is discussed in more detail in Section 4.5.1d.

#### 4.2.2 Analytical Procedure

The procedure utilized to prepare samples for quantitative x-ray diffraction was as follows. Pellets obtained were first ground into powder. The powder and a quartz standard were weighed out to a total weight of 0.1 grams. The percentages of powder and quartz weighed out are shown in Table 4.1.

Table 4.1 Weight Percent Sample and Quartz Standard

Alumina Addition	Weight Percent Sample	Weight Percent Quartz
0 wt. percent	95 wt. percent	5 wt. percent
50 wt. percent	90 wt. percent	10 wt. percent
75 wt. percent	95 wt. percent	5 wt. percent

The crystalline quartz content is very low because the resultant peak intensities of quartz are four times larger than alumina when combined in a 1:1 ratio. Therefore four times less must be added to avoid extreme experimental error. The sample and quartz standard mixture was weighed out and mixed, for about one minute, in acetone utilizing a small mortar and pestle. Care was taken to keep as much powder in the slurry, and not on the



pestle by rinsing with acetone. The mixture was then poured in a drying dish, and allowed to dry at room temperature for four hours. The entire amount of powder was divided on two glass slides. Two to three drops of a 1:20 volume percent collodion:methanol solution was added to the powder on the slides, and the resultant slurry was evenly distributed. The slurry was allowed to dry for five minutes, forming a uniform film. The samples were characterized with CuK $\alpha$  radiation on a computerized Rigaku x-ray diffractometer by scanning from 10-70° of 2 $\theta$  with a step size of 0.05° 2 $\theta$  and a one second count time. After scanning the background signal was removed, utilizing the data analysis software to provide uniform representation of the x-ray results.

The quantity of each of the crystalline and amorphous phases present was obtained by using Equation 4.3. The  $I/I_{COR}$  value and the d-spacing of the peaks used for the relative intensities of each phase are provided in Table 4.2. The details of how these  $I/I_{COR}$  values were obtained are provided in the next section.

Table 4.2.  $I/I_{COR}$  Values and Peaks Used for Analysis

Phase	$(I/I_{COR})$	d spacing (Å)
Al <sub>2</sub> O <sub>3</sub>	1.00	2.09
Hexacelsian	3.32	3.90
Mullite	0.65	2.20
Celsian	0.80	3.35, 3.27
BaSiO <sub>3</sub>	2.60	3.42
Quartz	4.00	4.30, 3.38

The amount of glass was obtained utilizing the following equation.

$$\text{Wt\% Glass} = 100 - (\text{wt\% alumina} + \text{wt\% crystalline phases}) \quad (\text{Eqn. 4.7})$$

The results obtained from the two slides of each sample were then averaged to provide the amount of each phase for that sample. The experimental error obtained for all of the quantitative results was +/- 10 weight percent.

#### 4.2.3. $I/I_{\text{COR}}$ Verification

To assure that the  $I/I_{\text{COR}}$  values provided by the JCPDS cards were correct, binary mixtures of pure crystalline phases and corundum were made to confirm the values. Also, the  $I/I_{\text{COR}}$  values for hexacelsian and mullite were calculated using such binary mixtures because these phases did not have reported  $I/I_{\text{COR}}$  values. Three steps are involved in determining the  $I/I_{\text{COR}}$  values of a crystalline material. (1) A pure crystalline material must be bought or prepared, and combined with corundum in a 1:1 ratio. (2) The mixture is then analyzed, and the  $I/I_{\text{COR}}$  value is calculated from the ratio of the 100% crystalline peak to the 100% corundum peak. (3) A known mixture other than 1:1 is made and analyzed utilizing the calculated  $I/I_{\text{COR}}$  value. If the  $I/I_{\text{COR}}$  value used satisfies the test, the value is confirmed. If not, a new one must be obtained. Table 4.3 provides the origin of all pure crystalline materials used in this research.

Hexacelsian and celsian were prepared by the author at the Colorado School of Mines. Hexacelsian was made by mixing stoichiometric amounts of  $\text{BaCO}_3$ ,  $\text{Al}_2\text{O}_3$ , and  $\text{SiO}_2$ . The mixture was calcined in a 99% alumina crucible at  $1690^\circ\text{C}$  for five hours, and then rapidly removed from the furnace. This allowed the material to air quench capturing

the metastable hexacelsian phase. Celsian was made by taking the same stoichiometric mixture as used for hexacelsian and heating to a temperature of 1590°C for eight hours followed by a slow cool of about 3°C/min.

Table 4.3. Sources of Crystalline Materials

SiO <sub>2</sub>	Alfa Research Chemicals
Mullite	Johnson Matthey Electronics
Celsian	CSM
Hexacelsian	CSM
Corundum	Coors Ceramics (Lot# BM-2206)

The JCPDS cards provided the  $I/I_{COR}$  values for celsian and quartz. The values obtained experimentally for a 1:1 ratio of each crystalline phase with corundum are compared to the JCPDS values in Table 4.4. The experimental values agree very well with those of the JCPDS cards.

Table 4.4. Comparison of Experimental and JCPDS ( $I/I_{COR}$ ) Values

	Experimental	JCPDS
Celsian	0.85	0.8
Quartz	4.0	3.6

To confirm the value for quartz additional mixtures of corundum and quartz were prepared by several different procedures by the author, C. Y. Kim. and C. T. Reed [48]. Based on this research the value of  $I/I_{\text{COR}}$  for quartz lies between 4.0 -4.2.

Table 4.5 provides a summary of the qualification results for hexacelsian and mullite. In determining and qualifying the  $I/I_{\text{COR}}$  values for each crystalline phase, the three procedural steps mentioned earlier were followed. Utilizing a 1:1 ratio of each crystalline phase with corundum, experimental  $I/I_{\text{COR}}$  values of 0.65 and 0.8 were determined for mullite and hexacelsian respectively. Arbitrary mixtures of each crystalline phase and corundum were then prepared in order to qualify the experimental  $I/I_{\text{COR}}$  values. The calculated weight percent for a 59/41 mullite/corundum mixture was 58 weight percent, indicating that the experimental  $I/I_{\text{COR}}$  value was linear in the experimental range of interest. The calculated weight percent hexacelsian for a 15/85 hexacelsian/corundum mixture was 46 weight percent, which indicates that the calibration curve is not linear. Therefore the calibration curve for hexacelsian had to be calculated in order to provide the acceptable  $I/I_{\text{COR}}$  value.

Table 4.5. Qualification Results of Hexacelsian and Mullite

	Exp. $I/I_{\text{COR}}$	Actual Wt%	Calculated Wt%
Mullite	0.65	59	58
Hexacelsian	0.8	15	46

In order to find the  $I/I_{\text{COR}}$  value of hexacelsian equation 4.3 was simplified to the following

$$X_h = X_c(1/K_h) (I_h/I_c) \quad (\text{Eqn. 4.8})$$

where,

$X_h$  = Weight percent hexacelsian,

$X_c$  = Weight percent corundum,

$K_h = I/I_{COR}$  value of hexacelsian,

$I_h$  = Relative intensity of 100% peak of hexacelsian, and

$I_c$  = Relative intensity of 100% peak of corundum.

The equation was then transformed into the form  $y = mx + b$  where  $1/K_h$  is the slope.

$$X_h/X_c = (1/K_h)(I_h/I_c) \quad (\text{Eqn 4.9})$$

In order to generate the calibration curve for hexacelsian binary mixtures of corundum and hexacelsian were made for 5, 10, 20, 25 and 50 weight percent hexacelsian. The ratios  $X_h/X_c$  and  $I_h/I_c$  were calculated for each mixture, and a plot of  $X_h/X_c$  vs  $I_h/I_c$  was generated. This plot was the calibration curve for hexacelsian and is shown in Figure 4.1. The inverse of the slope ( $1/K_h$ ) was then calculated to be  $K_h = 3.32$  for values of 0-20 weight percent hexacelsian. The qualification was reiterated and the  $I/I_{COR}$  agreed within 1% of the actual value.

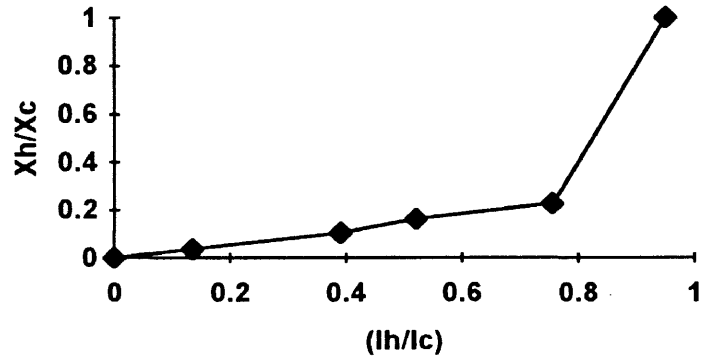


Figure 4.1. Calibration Curve of Hexacelsian

#### 4.3. Analytical Methodology: Alumina Dissolution

The dissolution of the alumina into the residual glass and crystal phases was analyzed as follows. At first, the alumina content for each sample was obtained through direct analysis of the x-ray diffraction patterns utilizing Equation 4.3. From the direct alumina content, the amount of alumina dissolving into the glassy and crystalline phases could be determined by the following equation.

*Wt% Alumina in Residual Glass and Crystal Phases =*

$$\frac{(\text{Wt}\% \text{ Al}_2\text{O}_3 \text{ addition}) - (\text{Wt}\% \text{ Final Al}_2\text{O}_3 \text{ content})}{(\text{Wt. fract. glass in sample})} + (\text{Wt}\% \text{ Al}_2\text{O}_3 \text{ in glass}) \quad (\text{Eqn. 4.10})$$

The resulting weight percent is normalized to eliminate the alumina addition.

#### 4.4. Analytical Methodology: Density Evaluation

The density of the experimental samples was evaluated as follows. The quantitative x-ray diffraction results were used to calculate the composition of the residual glass in each case. The density of the glass was then obtained utilizing a simple additive model as discussed in the next section[49]. The bulk density of the samples was measured utilizing the Archimedes method. The glass density, theoretical densities of the crystalline phases, and the bulk density were then utilized to obtain the theoretical and percent theoretical densities of the samples.

##### 4.4.1. Residual Glass: Composition and Density

The composition of the residual glass was calculated from the quantitative analysis of the percentages of the alumina, crystalline phases, and residual glass. The weight percent of a given oxide constituent in the residual glass was calculated by subtracting the amount of the oxide constituent in the crystalline phases from the content of the oxide constituent in the initial glass composition. The calculation was done by using a computer spreadsheet and the following equation.

*Wt % Oxide in Residual Glass =*

$$(\text{Wt}\% \text{ oxide in starting glass}) - \sum(\text{Wt fraction crystal A-X})(\text{Wt}\% \text{ oxide in crystal A-X})$$

(Eqn. 4.11)

The following equation was used for all constituent except alumina. The alumina content of the residual glass was calculated with the following equation, accounting for the amount of alumina dissolving into the glass.

*Wt% Alumina in Residual Glass =*

$$[(\text{Wt}\% \text{ Al}_2\text{O}_3 \text{ addition}) + (\text{Wt}\% \text{ Al}_2\text{O}_3 \text{ in glass})(\text{Wt. fract. glass in sample})] - [\Sigma(\text{Wt. fract. crystal A-X})(\text{Wt}\% \text{ crystalline Al}_2\text{O}_3 \text{ in A-X})] - (\text{Wt}\% \text{ Final Al}_2\text{O}_3 \text{ content})$$

(Eqn. 4.12)

The composition of the residual glass was then normalized so that the sum of all oxide constituents in the residual glass totaled one hundred weight percent.

Once the weight percentage of the residual glass components were obtained, the density of the glass was calculated by the additive method[49]. With this method, the density ( $\rho_g$ ) is calculated from the specific volume ( $V_g$ ) by the following formula:

$$1/\rho_g = V_g = X_1 V_1 + X_2 V_2 + \dots \quad (\text{Eqn. 4.13})$$

$X_n$  is the weight fraction of each constituent  $n$ , and  $V_n$  is the specific volume factor of each constituent which is equal to the volume that one gram of this constituent contributes to the glass[49]. The specific volume factors were determined empirically from density data for a wide range of glass compositions [49].



#### 4.4.2 Bulk, Theoretical, and Percent Theoretical Density

The bulk density of the samples was calculated by the Archimedes method with the following relation:

$$\rho_b = W_D \rho_L / (W_S - W_{SS}) \quad (\text{Eqn. 4.14})$$

$\rho_L$  = density of the saturating and submerging liquid.

$W_D$  = dry weight of the sample.

$W_S$  = saturated weight of the sample with all open pores filled with liquid.

$W_{SS}$  = weight of the sample submerged in liquid.

Literature values of x-ray densities of the crystalline phases were combined with the calculated residual glass density in order to calculate the theoretical density of each sample. Table 4.6 presents the x-ray densities of the crystalline phases present, for the exception of BaSiO<sub>3</sub>.

Table 4.6. X-Ray Densities of the Crystalline Phases

Phase	X-Ray Density (g/cc)
Al <sub>2</sub> O <sub>3</sub>	3.99
Celsian	3.39
Hexacelsian	3.30

The following relation was used to calculate the theoretical density:

$$\rho_{th} = 1/[(X_g/\rho_g + X_a/\rho_a) + \Sigma X_c/\rho_c] \quad (\text{Eqn. 4.15})$$

where  $X_g$ ,  $X_a$ , and  $X_c$ , are the weight fractions of residual glass, crystalline alumina, and crystalline phases respectively, and  $\rho_g$ ,  $\rho_a$ , and  $\rho_c$  the respective value of density for each constituent. The percent theoretical density was then calculated from the ratio of the measured bulk densities to the theoretical densities.

## 4.5 Results and Discussion

### 4.5.1 Quantitative X-ray Diffraction Analysis and Alumina Dissolution

The samples with 0, 50 and 75 weight percent alumina addition were quantitatively analyzed. Two major phases crystallized, celsian and hexacelsian and one minor phase  $\text{BaSiO}_3$ . Since  $\text{BaSiO}_3$  was relatively small in content it was not represented in the quantitative plots that follow. However, a summary of the amount of  $\text{BaSiO}_3$  crystallization as well as the raw data for the quantitative plots is provided in Appendix B.

Three major variables effected the crystallization behavior. These were firing temperature,  $\text{SiO}_2/\text{BaO}$  ratio or composition, and crystalline alumina addition. Composition 3 was also analyzed with and without  $\text{MoO}_3$  addition (3b and 3a respectively). To simplify the discussion the quantitative results will be discussed as functions of composition and temperature with alumina addition held constant for compositions 2a, 3a, and 4a without  $\text{MoO}_3$  addition. The amount of alumina dissolving into the crystalline phases and residual glass as well as the composition of the residual

glass will be discussed in the same manner. Following this discussion the effect of  $\text{MoO}_3$  addition on the quantitative crystallization behavior of composition 3 will be discussed. It is important to note that the results do not necessarily reflect the crystallization behavior at a given equilibrium temperature, but do reflect the crystalline species present after a given firing cycle with a given hold temperature and time. In order to provide for consistent results all plots for the exception of those with 0 weight percent alumina have been normalized with respect to alumina addition. Even though crystalline alumina impurities were present in the 0 weight percent alumina samples, the amount of crystalline alumina present was assumed to be zero.

#### ***4.5.1a 0% Alumina Addition***

Figure 4.2(A-D) summarizes the quantitative x-ray diffraction results of the percentages of all major crystalline phases for samples with 0 weight percent alumina addition. Figure 4.2(E-G) summarizes the composition of the residual glass for samples with 0 weight percent alumina addition, while Figure 4.2(H) provides the amount of alumina present in the residual glass plus crystalline phases. Crystalline alumina exists as an impurity from ball milling in the samples without alumina addition. Therefore the data at  $800^\circ\text{C}$  represents the original glass composition plus the amount of alumina present from contamination. This crystalline alumina content did not vary significantly as a function of either composition or temperature as shown in Figure 4.2(D,H).

The crystallization of celsian [Figure 4.2(A)] only occurred in composition 3a, which has the stoichiometric  $\text{SiO}_2/\text{BaO}$  ratio (=2) of celsian. The amount of celsian crystallization reached a maximum after heat treatment at  $1000^\circ\text{C}$ , and did not vary with heat treatment at  $1100^\circ\text{C}$ . This corresponds to the depletion of alumina from the glass

[see Figure 4.2(F)]. Thus, the alumina content limited the crystallization of celsian in composition 3a with 0 weight percent alumina addition. Celsian crystallization did not occur in compositions 2a ( $\text{SiO}_2/\text{BaO} = 4$ ) or 4a ( $\text{SiO}_2/\text{BaO} = 1.4$ ). In composition 2a the limiting constituent was BaO [see Figure 4.2(E)], while  $\text{SiO}_2$  is assumed to be the limiting constituent in composition 4a. The residual glass content of composition 4a ( $\text{SiO}_2/\text{BaO} = 1.4$ ) could not be calculated because minor amounts of barium silicate crystallized, for which the density was not known.

The crystallization of hexacelsian [Figure 4.2(B)] occurred in all compositions. In compositions 2a and 4a, with 0 weight percent alumina addition, hexacelsian was the only phase that crystallized after heat treatment at 1000 and 1100°C, while composition 3a crystallized both hexacelsian and celsian. The residual glass content is shown, in Figure 4.2(C), to decrease after heat treatment corresponding to crystallization.

#### ***4.5.1b 50% Alumina Addition***

Figure 4.3 summarizes the quantitative x-ray diffraction results of the percentages of all major crystalline phases, the compositions of the residual glasses, and the amount of alumina in the glass plus crystalline phases for samples with 50 weight percent alumina addition. The crystalline alumina [see Figure 4.3(D)] content remained fairly constant, within experimental error, with heat treatment temperature up to 1340°C. The alumina content then decreased at 1540°C corresponding to dissolution of alumina into the residual glass and crystalline phases [ see Figure 4.3(H)]. The amount of alumina dissolution was greatest in composition 4a ( $\text{SiO}_2/\text{BaO} = 1.4$ ), and the least in composition 2a ( $\text{SiO}_2/\text{BaO} = 4$ ). This is due to the increased glass viscosity of composition 2a compared to that of composition 4a, because of the larger  $\text{SiO}_2$  content.

Composition	SiO <sub>2</sub> /BaO Ratio
2a	4.0
3a, 3b	2.0
4a	1.4

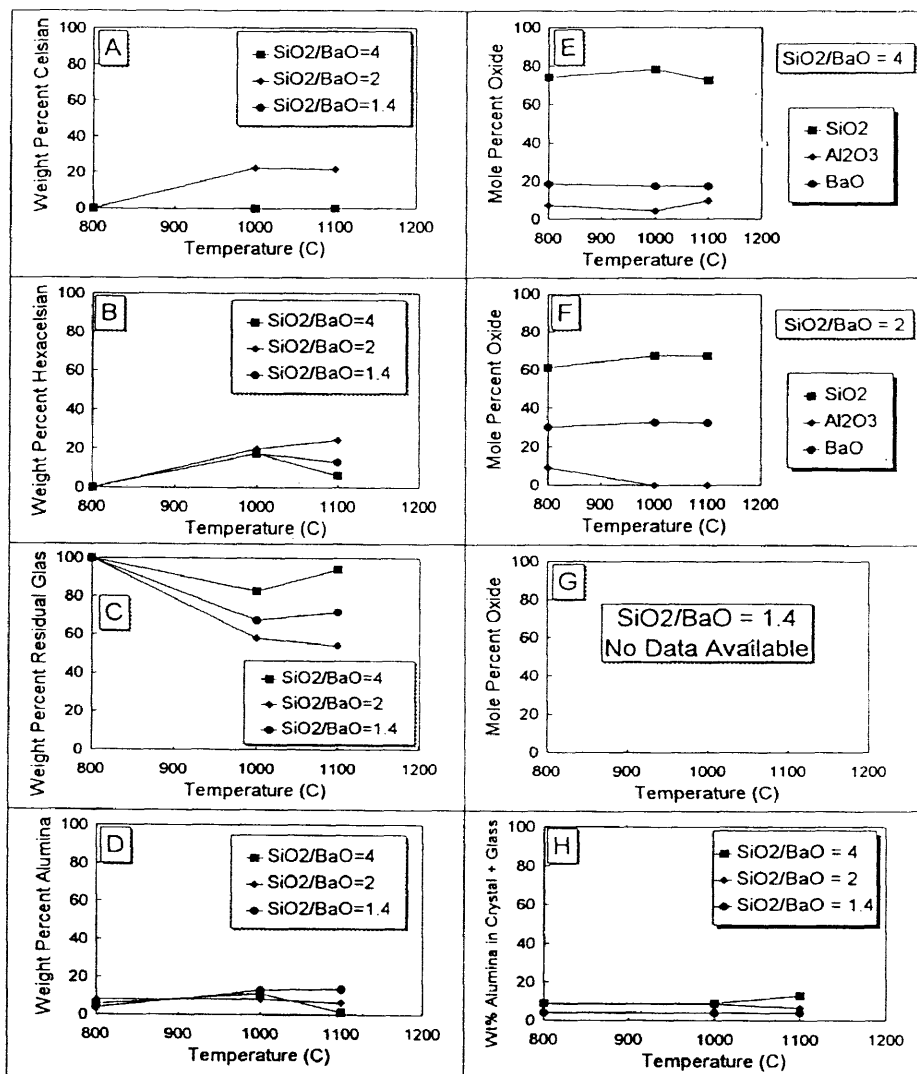


Figure 4.2. Weight percent celsian (A), hexacelsian (B), residual glass (C), and crystalline alumina (D) plotted versus temperature. Residual glass composition of SiO<sub>2</sub>/BaO=4 (E), SiO<sub>2</sub>/BaO=2 (F), SiO<sub>2</sub>/BaO=1.4 (G), and alumina in glass + crystalline phases (H) plotted versus temperature. All plots for 0% alumina addition. The data plotted in figures A, B, and C was renormalized after subtracting the crystalline alumina content.

The crystallization of celsian [Figure 4.3(A)] occurred in all compositions, but was a maximum in the stoichiometric ( $\text{SiO}_2/\text{BaO} = 2$ ) composition (3a). The maximum being 100% crystallization of the residual glass with heat treatment at  $1340^\circ\text{C}$ . The crystallization of celsian in composition 2a was limited due to the exhaustion of alumina in the residual glass[ see Figure 4.3 (E)]. Composition 4a was not limited by such glass phase constituents, and crystallized celsian quite easily at temperatures above  $1100^\circ\text{C}$ . The amount of crystallization increased as the heat treatment temperature was increased up to  $1340^\circ\text{C}$ . Heat treatment at  $1540^\circ\text{C}$  decreased the amount of crystalline phases potentially because of increased dissolution of alumina, celsian, and/or hexacelsian into the amorphous phase.

The crystallization of hexacelsian [Figure 4.3(B)] was dominant at temperatures below  $1340^\circ\text{C}$ , and prevalent in compositions with low  $\text{SiO}_2/\text{BaO}$  ratio ( $\text{SiO}_2/\text{BaO} = 1.4$ ). As the  $\text{SiO}_2/\text{BaO}$  ratio increased, the amount of hexacelsian tended to decrease. This corresponds to the deviation of the composition away from the hexacelsian phase field. It is also important to note that as the amount of celsian increased hexacelsian decreased, signifying the transformation to the more stable celsian phase.

The residual glass was exhausted in all compositions [Figure 4.3(C)]. In the  $\text{SiO}_2/\text{BaO} = 4$  composition this occurred at  $1340^\circ\text{C}$ ; with  $\text{SiO}_2/\text{BaO} = 2$  at  $1000^\circ\text{C}$ ; and with  $\text{SiO}_2/\text{BaO} = 1.4$  at  $1100^\circ\text{C}$ . This signifies that within the limits of quantitative x-ray diffraction 100% crystallization was attainable. The high silica composition (2a) was able to obtain 100% crystallization through the formation of a solid solution of silica with the celsian and hexacelsian crystal phases. When the silica entered into solid solution, the glass composition was driven toward the stoichiometric composition, allowing increased crystallization of the celsian polymorphs to occur, resulting in 100% crystallization.

Composition	SiO <sub>2</sub> /BaO Ratio
2a	4.0
3a, 3b	2.0
4a	1.4

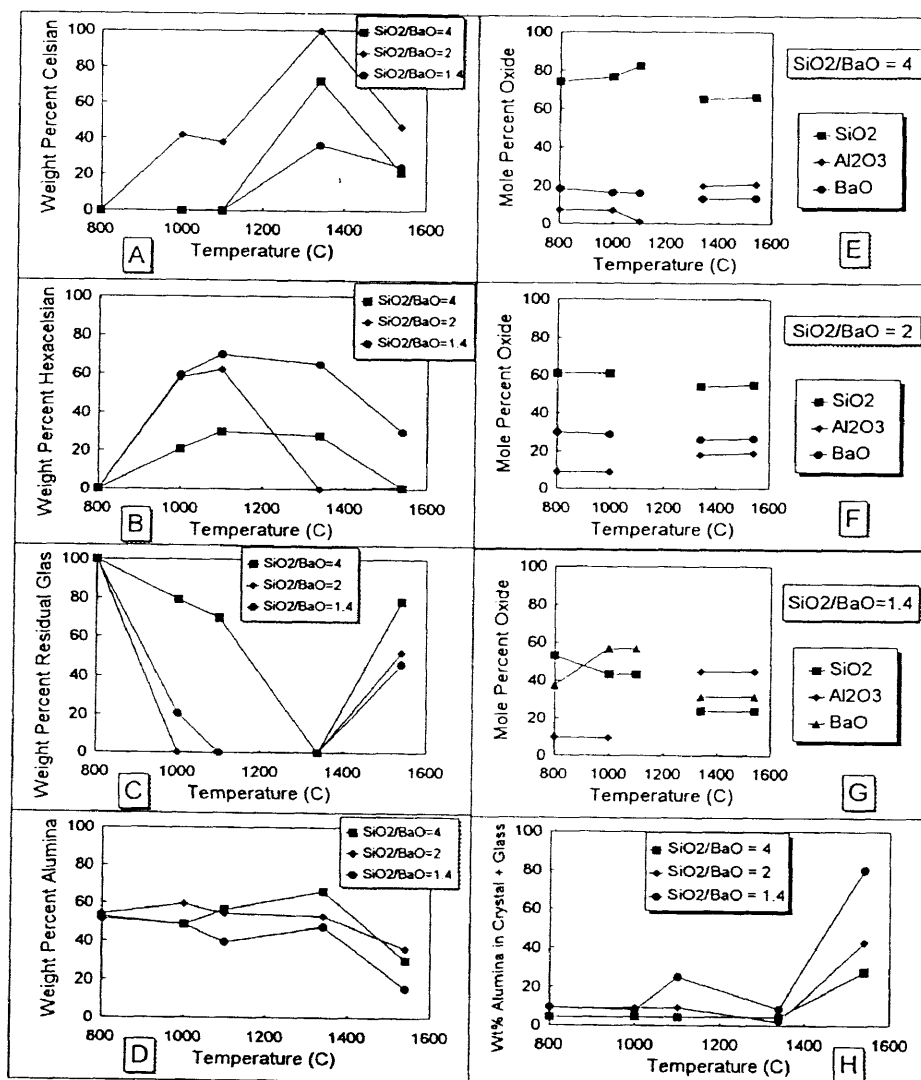


**Figure 4.3.** Weight percent celsian (A), hexacelsian (B), residual glass (C), and crystalline alumina (D) plotted versus temperature. Residual glass composition of SiO<sub>2</sub>/BaO=4 (E), SiO<sub>2</sub>/BaO=2 (F), SiO<sub>2</sub>/BaO=1.4 (G), and alumina in glass + crystalline phases (H) plotted versus temperature. All plots for 50% alumina addition. The data plotted in figures A, B, and C was renormalized after subtracting the crystalline alumina content.

Composition 4a, or the high barium content glass, crystallized barium silicate (not shown) at low temperatures. This reduced the barium content, driving the glass toward the stoichiometric composition. This decrease in BaO allowed the celsian polymorphs to crystallize, and resulted in 100% crystallization. The stoichiometric phase shows the widest window of complete crystallization (1000 to 1340°C), with celsian as the only crystalline phase present at 1340°C. As temperature increased however, so did the residual glass composition. In Figures 4.3 E - G, a discontinuity occurs in the plots of the oxide constituents. This occurs, because at such temperatures 100% crystallization occurs, and no residual glass is present.

#### ***4.5.1c 75% Alumina Addition***

Figure 4.4 summarizes the quantitative x-ray diffraction results of the percentages of all major crystalline phases, the compositions of the residual glasses, and the amount of alumina in the glass plus crystalline phases for samples with 75 weight percent alumina addition. The crystalline alumina content [Figure 4.4(D,H)] varied in a similar manner as the samples with 50% alumina addition, but the increased dissolution of alumina generally occurs above 1540°C.

The crystallization of celsian [Figure 4.4(A)] was found to be the major constituent of both the high stoichiometric SiO<sub>2</sub>/BaO compositions, with maximums occurring at 1540°C. The shift of this maximum from 1340°C for the 50 weight percent alumina addition samples signifies that increased alumina addition inhibits crystallization. The amount of celsian increased with increasing temperature to each maximum and decreased thereafter. As shown in Figure 4.4(E-H), this corresponds to both the increased dissolution of alumina into the glass as well as dissolution of celsian back into the glass.



Composition	SiO <sub>2</sub> /BaO Ratio
2a	4.0
3a, 3b	2.0
4a	1.4

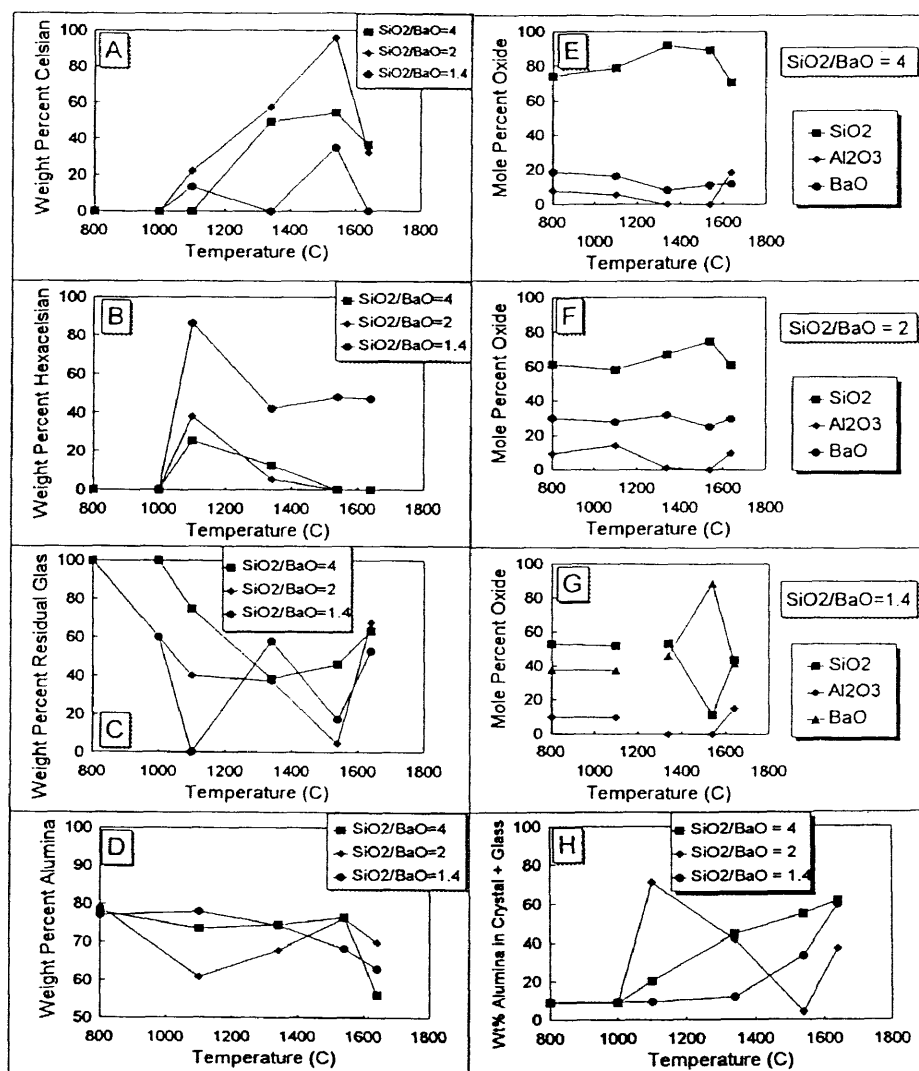


Figure 4.4. Weight percent celsian (A), hexacelsian (B), residual glass (C), and crystalline alumina (D) plotted versus temperature. Residual glass composition of SiO<sub>2</sub>/BaO=4 (E), SiO<sub>2</sub>/BaO=2 (F), SiO<sub>2</sub>/BaO=1.4 (G), and alumina in glass + crystalline phases (H) plotted versus temperature. All plots for 75% alumina addition. The data in figures A, B, and C was renormalized after subtracting the crystalline phase alumina content.

Hexacelsian followed the opposite trend of celsian [Figure 4.4(B)]. This indicates that the transformation from hexacelsian to celsian was occurring. Hexacelsian dominated in the low  $\text{SiO}_2/\text{BaO}$  composition corresponding to the proximity of the hexacelsian phase field. The residual glass [Figure 4.4(C)] decreased with temperature to  $1540^\circ\text{C}$  and then increased. Nearly 100% crystallization was attained in the stoichiometric composition at  $1540^\circ\text{C}$  with celsian the only crystalline phase (in addition to alumina). Above  $1540^\circ\text{C}$  all compositions showed an increase in residual glass apparently because of alumina and celsian phase dissolution.

#### ***4.5.1d 96% Alumina Addition***

Quantitative x-ray diffraction analysis of the percentages of intergranular crystalline phases in the 96 weight percent alumina samples was not possible because of the experimental error involved. However, using the binary auto-flushing method discussed earlier, the ratios of celsian to mullite were obtained as summarized in Table 4.7. The results are reported only for those samples having only two phases other than that of crystalline alumina. Therefore the only resultant phase relationships are that of celsian and mullite. As will be shown in the following temperature, only samples heat treated at  $1640^\circ\text{C}$  are of interest.

Table 4.7 Ratio of Crystalline Phases in 96% Alumina at 1640°C

Sample	Phases	Ratio
2a	Mullite:Celsian	1.5
2b	Mullite:Celsian	1.5
3a	Mullite:Hexacelsian:Celsian	-----
3b	Mullite:Celsian	1.5
4a	Hexacelsian	1
4b	Hexacelsian	1

As Table 4.7 shows, the relative ratio of mullite to celsian was equivalent in all compositions and did not vary with composition.

#### 4.5.1e *MoO<sub>3</sub> Addition*

The quantitative crystallization behavior of composition 3 was analyzed with and without the addition of MoO<sub>3</sub> as a nucleating agent. Compositions with MoO<sub>3</sub> additions were labeled as 3b, while those without were categorized 3a. Figures 4.5, 4.6, and 4.7 show the crystallization behavior of these compositions with 0, 50, and 75 weight percent alumina addition, respectively. As the results show, similar crystallization behavior occurs between those with and without MoO<sub>3</sub> addition. This correlates with the qualitative x-ray diffraction results. However, the addition of MoO<sub>3</sub> to composition 3 with 50 and 75 weight percent alumina addition tends to increase the amount of crystallization and the transformation of hexacelsian to celsian.

#### 4.5.2 Densification Analysis

The percent theoretical density was calculated as presented in the previous section. Figure 4.8(A-D) provides the percent theoretical density as a function of temperature for 0, 50, 75, and 96% alumina addition. From these results one can see that as the alumina content increases, the tendency for the density to vary with composition decreases. With low alumina addition compositions rich in  $\text{SiO}_2$  tend to densify to near theoretical values, and the density decreases as the  $\text{SiO}_2$  content decreases. With low  $\text{SiO}_2$  content the viscosity is low and the crystallization rate is high. Increased crystallization hampers the densification of the glass, resulting in lower density.

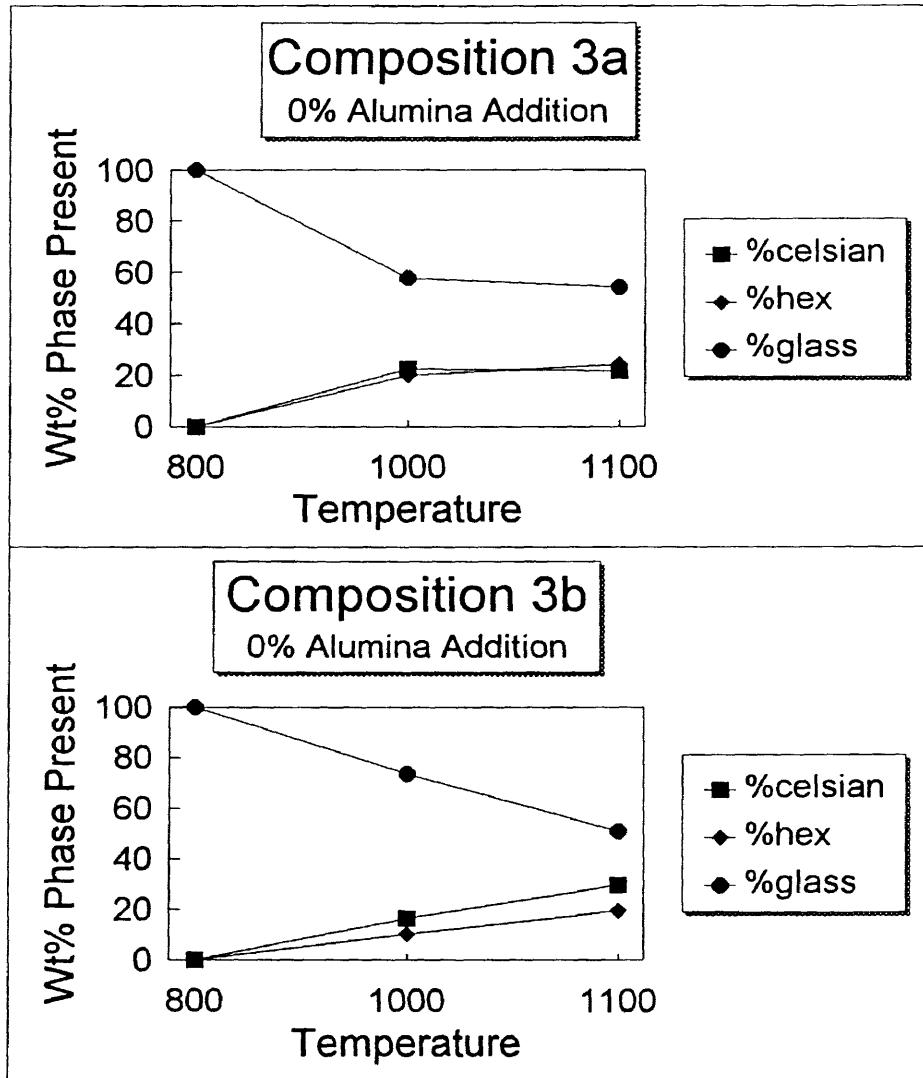


**Figure 4.5:** Quantitative crystallization results comparing composition 3a and 3b with 0% alumina addition. The data were not renormalized with respect to crystalline alumina impurity.

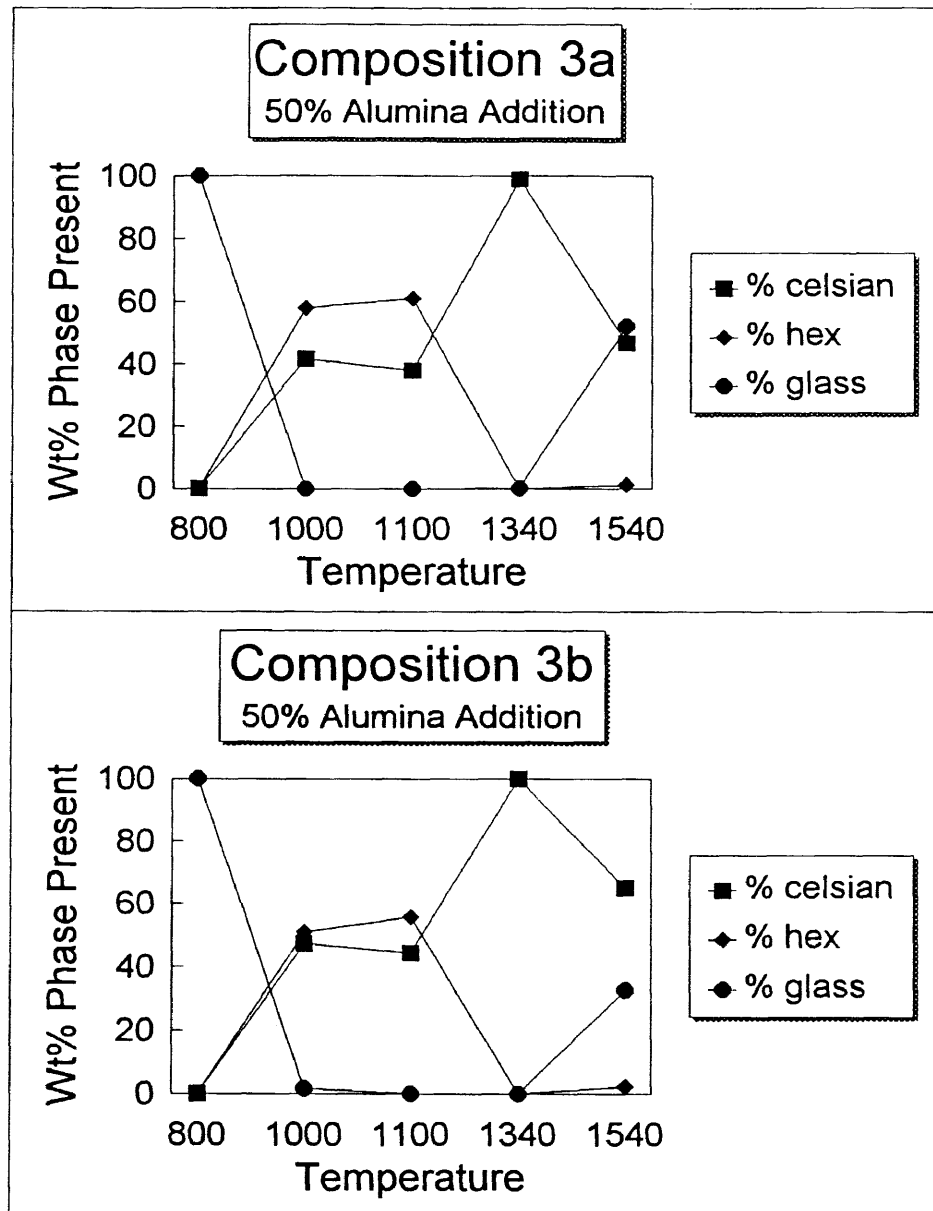


**Figure 4.6:** Quantitative crystallization results comparing composition 3a and 3b with 50% alumina addition. The data were renormalized after subtracting the crystalline alumina content.

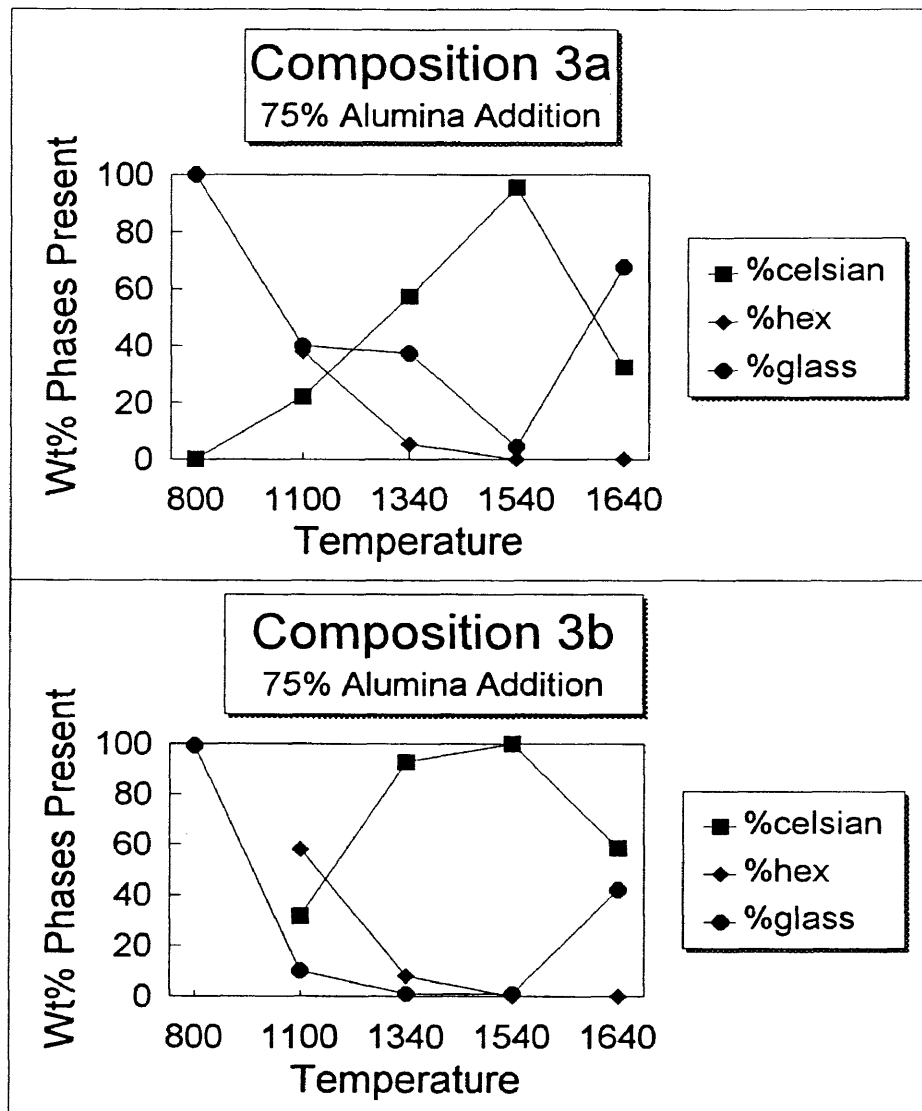


**Figure 4.7:** Quantitative crystallization results comparing composition 3a and 3b with 75% alumina addition. The data were renormalized after subtracting the crystalline alumina content.

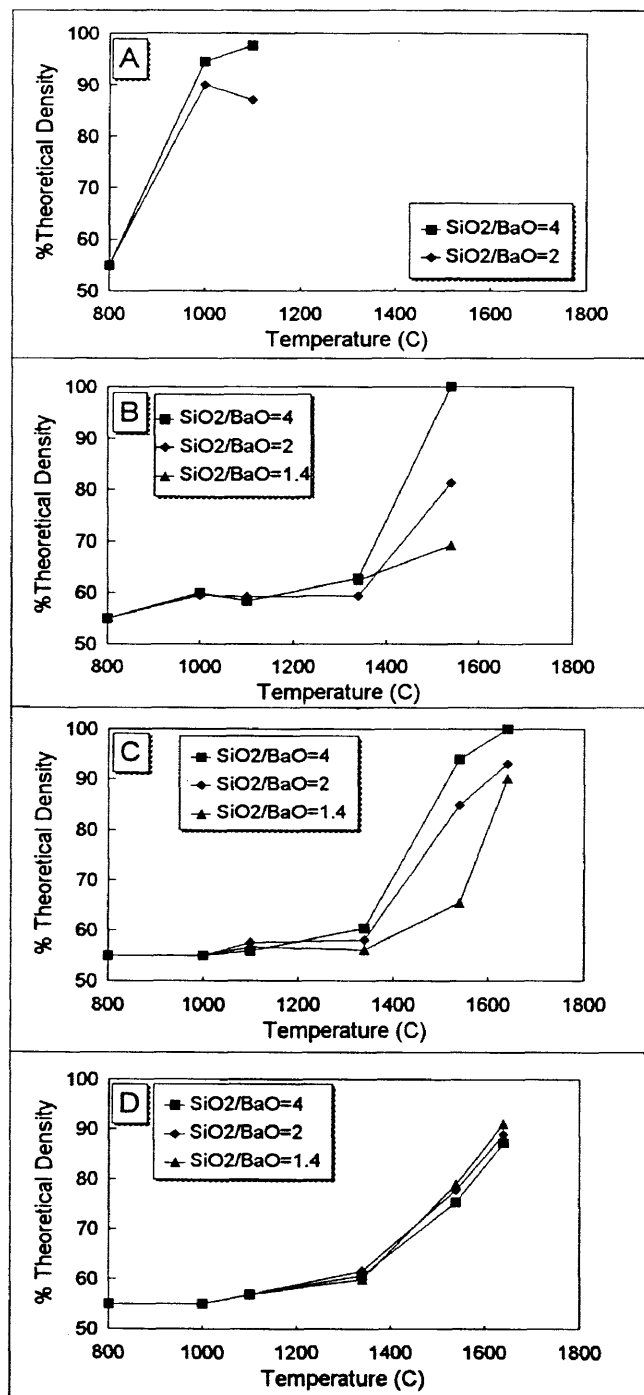


**Figure 4.8:** The percent theoretical density plotted versus temperature for 0 (A), 50 (B), 75(C), and 96 weight percent (D) alumina addition.



#### 4.6. Summary and Conclusions

X-ray diffraction was used to quantitatively analyze the crystallization behavior of various barium aluminosilicate glass compositions as a function of firing temperature, alumina addition, and  $\text{SiO}_2/\text{BaO}$  ratio. Also the effect of  $\text{MoO}_3$  additions as a nucleating agent on the crystallization behavior was also investigated. Utilizing the quantitative results, the percent theoretical density of all samples was evaluated as a function of temperature, alumina addition, and  $\text{SiO}_2/\text{BaO}$  ratio.

The results show that in all compositions, the amount of alumina dissolution increases with temperature. Areas of 100% crystallization are attainable in the 50 and 75 weight percent alumina additions, occurring at 1340 and 1540°C, respectively. This temperature increase signifies that increased alumina additions decrease the rate of crystallization. The amount of residual glass was found to reach a minimum at the maximum crystallization temperatures, and then increases with higher temperature heat treatment. The increase in residual glass is attributed to the increased dissolution of both the alumina and celsian phases back into the glass and is confirmed by the residual glass compositions. In general the stoichiometric composition ( $\text{SiO}_2/\text{BaO}=2$ ) crystallized more than the nonstoichiometric compositions with  $\text{SiO}_2/\text{BaO}$  ratios of 4 and 1.4. Crystallization was limited in these nonstoichiometric compositions, because of the depletion of oxide constituents from the glass compositions. The crystallization of the high  $\text{SiO}_2/\text{BaO}$  composition was limited by the amount of BaO, while the low  $\text{SiO}_2/\text{BaO}$  composition was limited by the amount of  $\text{SiO}_2$ . However solid solutions of celsian phases with silica as well as the crystallization of non-celsian phases could increase the crystallization of these nonstoichiometric compositions to near 100%.

Additions of  $\text{MoO}_3$  did not have an impact on the quantitative crystallization behavior of compositions 2 and 4, supporting the results obtained in Phase 1 of this work. However, the addition of  $\text{MoO}_3$  to composition 3 with 50 and 75 weight percent alumina addition tends to increase the amount of crystallization and the transformation of hexacelsian to celsian. The density results show that as the alumina content increases, the density of the intergranular crystalline and glassy phases have less effect on the overall density of the sample. However with low alumina addition the density increases as the firing temperature increases with increasing  $\text{SiO}_2$  content in the glass.

Quantitative x-ray diffraction analysis was also used to find the ratio of crystalline phases present in 96 weight percent alumina. The ratio found between mullite and celsian was 1.5 and did not vary with composition. The residual glass content could not be directly calculated because the amount of alumina dissolution was unknown. The residual glass content and composition need to be calculated in order to obtain the TCE of the glasses forming in 96 weight percent alumina bodies. The next chapter details a method by which the residual glass compositions were approximated.

### ***Transient Glass Phase Processing (TGPP)***

An interesting result that was observed through the evaluation of the quantitative x-ray diffraction data was a novel processing route known as transient glass phase processing (TGPP). TGPP can most readily be seen when 100% crystallization of the residual glass occurs. In this work, this occurred in the 50 and 75 weight percent alumina additions, thus forming a composite of crystalline material and alumina. TGPP is envisioned as a novel processing route by which crystal-alumina composites may be

manufactured, as well as pure crystalline material with the appropriate and controlled addition of alumina.

Transient glass phase processing, as observed by the author, combines aspects of two common ceramic processes: (1) glass-ceramic processing and (2) viscous phase sintering. The aspect utilized from viscous phase sintering is the viscous transport mechanism provided by the glass phase, while glass-ceramic processing donates the aspect of crystallization from a glass. These two aspects come together in the following discussion of the TGPP process. Taking a 50:50 glass:alumina composition and heating to low temperatures an alumina microstructure consisting of alumina grains and glassy triple points is produced. Upon further heating the alumina begins to dissolve, driving the original glass composition toward the alumina rich side of the phase diagram as represented in Figure 4.9 by the arrow. At some point crystallization occurs consuming the alumina and driving the glass composition back toward its original composition. This give and take of alumina between crystallization and dissolution keeps the overall process at 200-300°C less than normal processing temperatures, thus creating a distinct advantage in the manufacture of such materials.

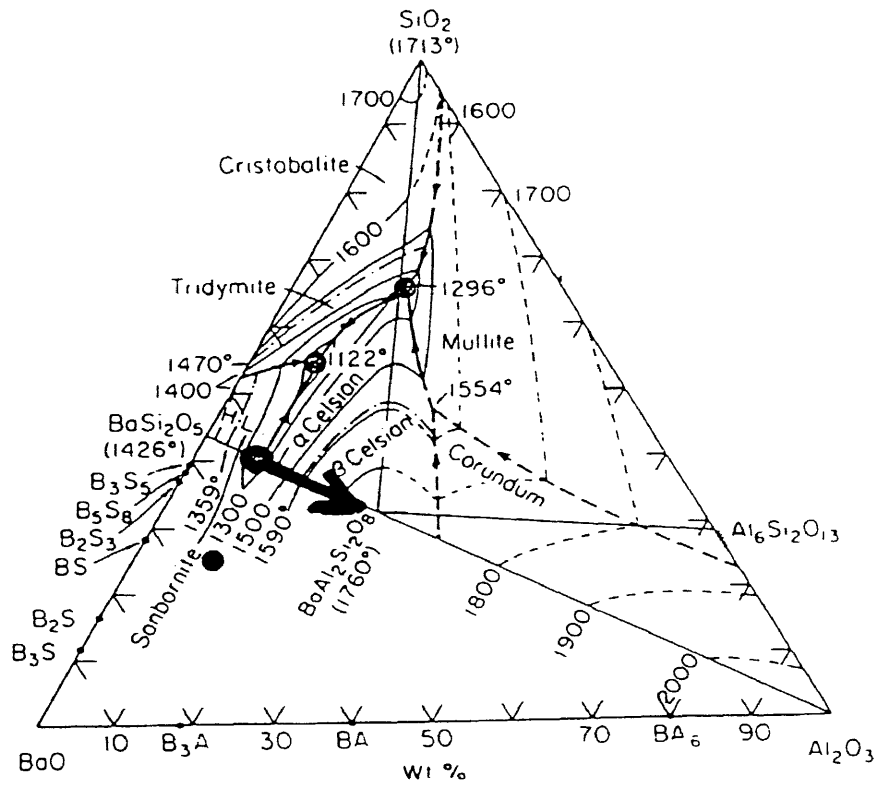


**Figure 4.9.** Schematic representation of glass composition as it increases in alumina content due to transient glass phase processing.

## **CHAPTER 5**

### **PHASE 3: 96% ALUMINA - ALUMINA DISSOLUTION, RESIDUAL GLASS THERMAL EXPANSION, AND COMPOSITIONAL MODELING FOR MISMATCH ANALYSIS**

The research in phase one has provided a variety of crystalline bases for thermal expansion mismatch analysis of 96 weight percent alumina ceramics. In phase two the relative quantitative ratios of the phases crystallizing in such high alumina ceramics was determined from x-ray diffraction data, as well as the quantitative behavior of alumina dissolution and residual glass content for lower alumina content mixtures. Phase three of this research was focused on deriving the amount of alumina dissolution, the thermal expansion of the resultant residual glasses, and compositional modeling of 96 weight percent alumina ceramics. The amount of alumina dissolution was used to calculate the thermal coefficient of expansion of the residual glass. Once the alumina dissolution and thermal expansion were known, models for TCE mismatch analysis were satisfied through modeling and direct observation. All of the methods used in this phase of the research were computational and dependent upon each previous section of work. For simplicity each section will present methodologies as well as results so as not to disrupt the logical experimental flow. In section one the procedure used to approximate the quantitative dissolution behavior of alumina for 96 weight percent alumina samples will be discussed. In section two the derivation of the state of thermal expansion of the residual glass for each composition will be presented, while in section three the methods and results of

compositional modeling will be detailed. The results will then be summarized in section four.

### 5.1. Alumina Dissolution

In previous phases of this research 96 weight percent aluminas were investigated with three barium aluminosilicate glass compositions. The crystallization behavior of these samples was analyzed with and without MoO<sub>3</sub> addition after heat treatment at 1340 - 1640°C. Because ultimately dense alumina bodies are required, only the data on samples fired at 1640°C was considered in this phase of research. Since a distinct thermal expansion mismatch between the alumina and crystalline phase (crystalline phase TCE is either higher or lower than alumina) was desired for mismatch analysis, only those samples with results meeting these criteria were considered. Table 5.1 summarizes the compositions used for this phase of the work, their resultant crystalline composition after firing at 1640°C, and their SiO<sub>2</sub>/BaO ratio.

Table 5.1. Compositions Used in Phase 3

Composition	Crystalline Composure	SiO <sub>2</sub> /BaO
2a	celsian, mullite	4.0
3b	celsian, mullite	2.0
4a	hexacelsian	1.4

### 5.1.1. Methodology

The amount of alumina dissolution in 96 weight percent alumina samples is equivalent to the amount of alumina entering the crystalline phases plus residual glass minus the starting alumina content in the glass. As was presented in phase two, the amount of alumina entering both the crystalline phases and the glass was directly calculated from the quantitative analysis of 0, 50, and 75 weight percent alumina additions. The dissolution of alumina in the 96 weight percent alumina samples could not be directly calculated, because of the small amount of glass and crystalline phases and the experimental error of the quantitative x-ray diffraction procedure. Therefore, an extrapolation method was utilized to determine upper and lower bounds based on existing quantitative data.

As was discovered through quantitative analysis, the amount of alumina dissolution decreased with increasing alumina addition. It was therefore assumed that the amount of alumina entering the crystalline and glassy phases in 96 weight percent alumina samples was less than that of the 75 weight percent samples. As a result the amount of alumina dissolution occurring in the 75 weight percent alumina samples at 1640°C was used as an upper limit. The lower limit was taken to be the amount of alumina present in the original glass composition. The resultant range is believed to contain the appropriate value for alumina dissolution occurring in 96 weight percent alumina. The utilization of this range will be discussed in the next section.

### 5.1.2. Results and Discussion

Figures 5.1, 5.2, and 5.3 provide the weight percent alumina in the crystalline plus glassy phases versus temperature for  $\text{SiO}_2/\text{BaO}$  ratios equal to 4, 2, and 1.4 respectively. The weight percent alumina in the crystalline and glassy phases is the same data provided in Chapter Four. In each of these plots are two dashed lines representing the upper and lower limits of dissolution. The determination of these bounds was explained in Section 5.1.1. By comparing these three figures, one can see that the amount of dissolution is least in the stoichiometric phase ( $\text{SiO}_2/\text{BaO} = 2$ ) and greatest in both non-stoichiometric compositions. Table 5.2 provides a summary of the results in Figures 5.1 - 5.3. Approximate values of alumina in the crystalline and glassy phases were utilized in Table 5.2, because the results of quantitative analysis could only be calculated to +/- 10 weight percent.

Table 5.2. Results of Alumina Dissolution in 96% Alumina Ceramics

$\text{SiO}_2/\text{BaO}$	Upper Limit	Lower Limit
4.0	60%	10%
2.0	30%	10%
1.4	60%	10%



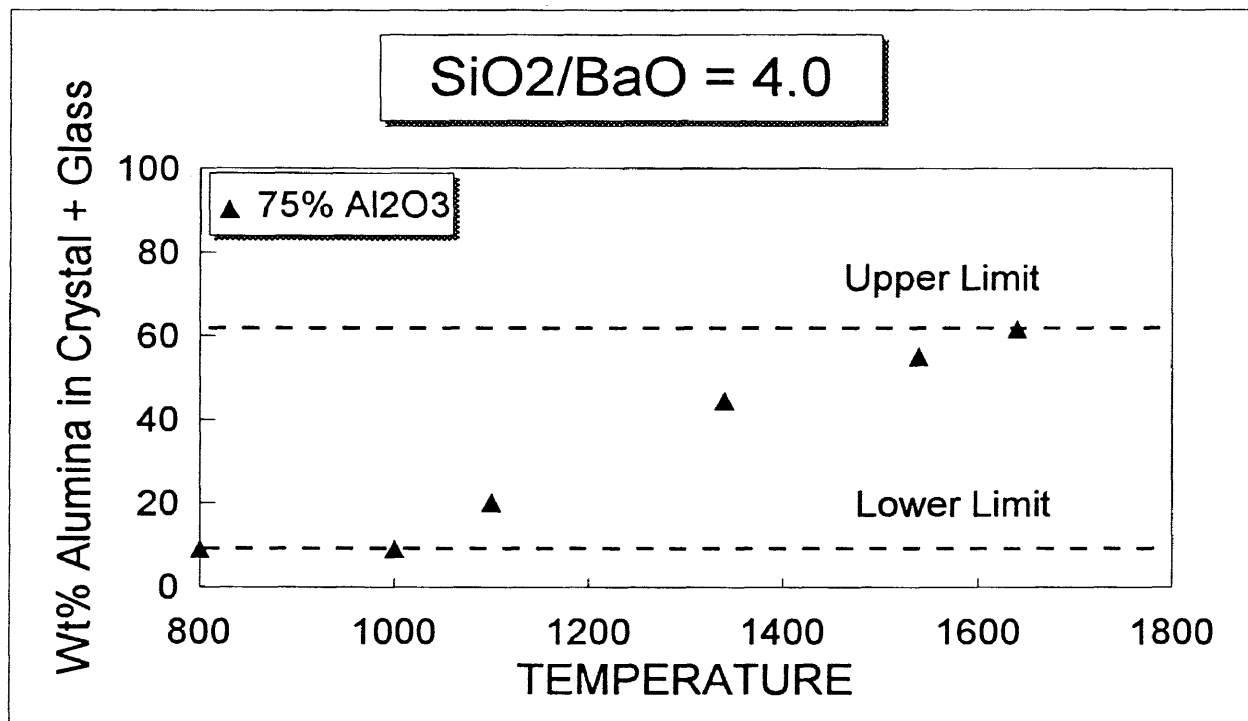


Figure 5.1. The weight percent alumina in crystal + glass plotted versus the firing temperature for composition 2a with  $\text{SiO}_2/\text{BaO}=4$ .

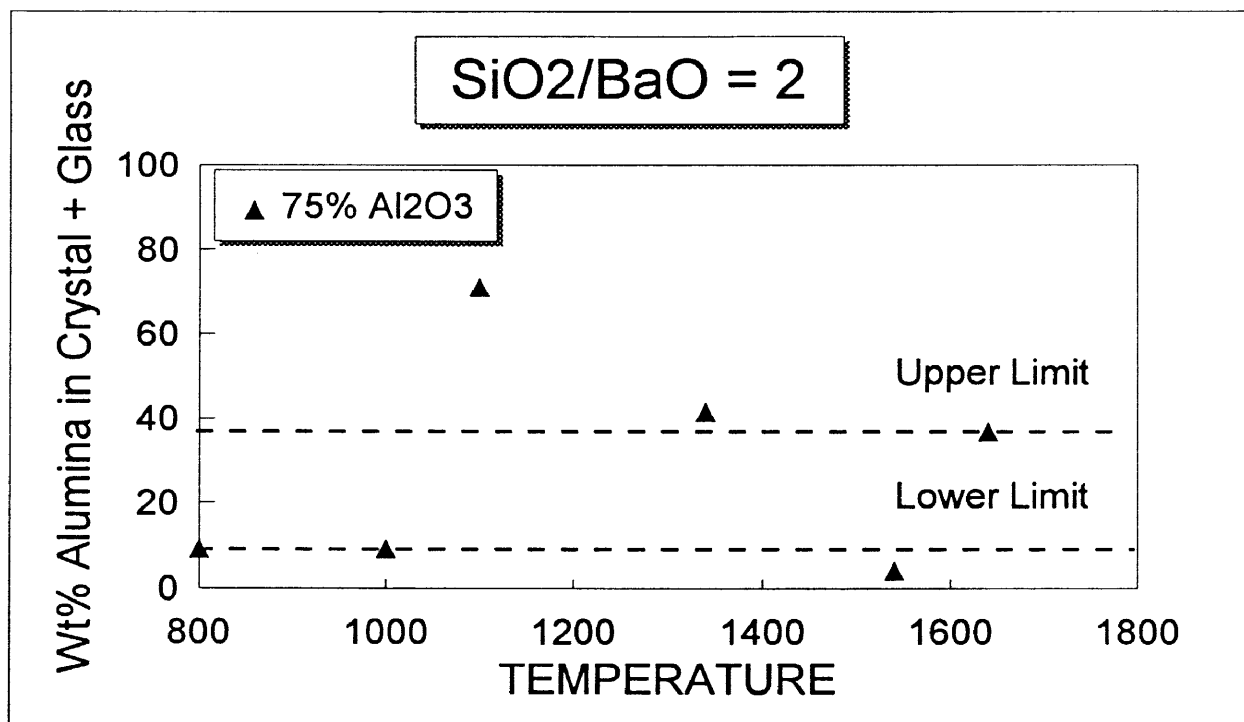


Figure 5.2 The weight percent alumina in crystal + glass plotted versus the firing temperature for composition 3b with  $\text{SiO}_2/\text{BaO}=2$ .

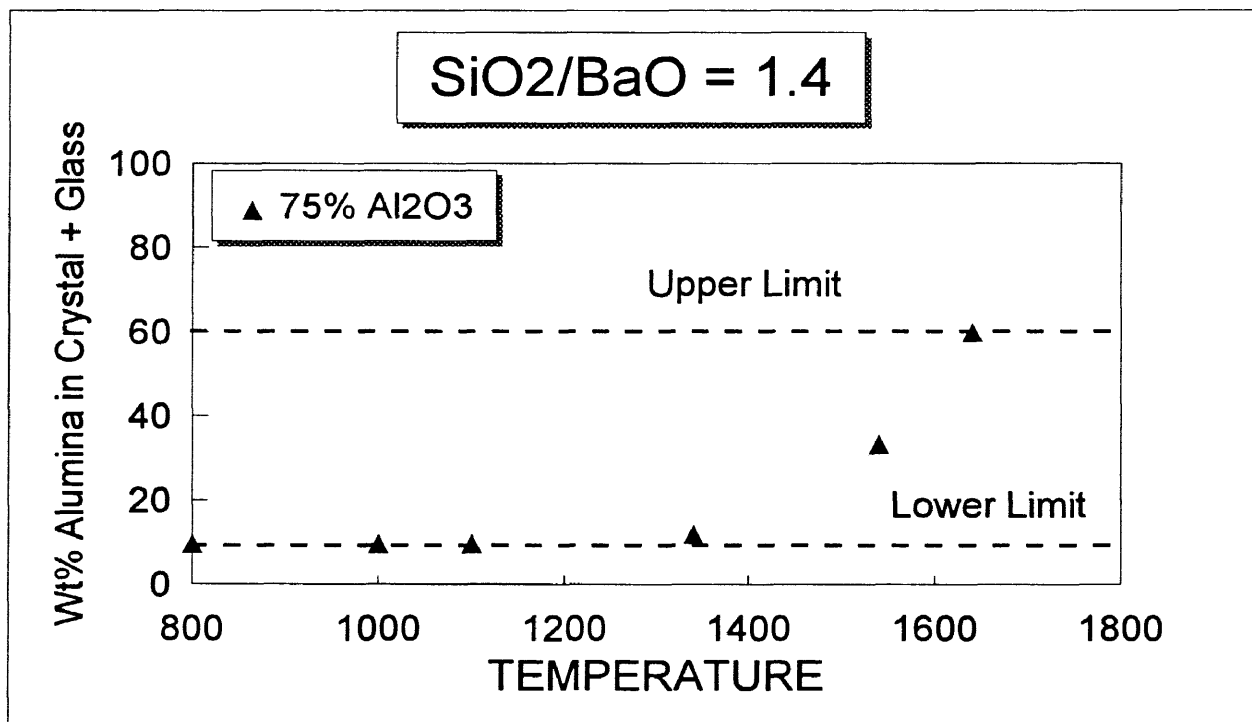


Figure 5.3. The weight percent alumina in crystal + glass plotted versus the firing temperature for composition 4a with  $\text{SiO}_2/\text{BaO}=1.4$ .

## 5.2. The Thermal Expansion of the Residual Glass

### 5.2.1. Estimation of the Thermal Expansion of Oxide Glasses

Several models have been used in the past for the estimation of the thermal expansion of oxide glasses [50,51]. In this section an empirical model proposed by J.Hormadaly [52] to estimate the TCE of glass compositions is presented. In this model only the modifiers in the glass are treated as parameters. The modifiers are considered as a perturbation to the glass network. The TCE is related to the ionic radius ( $r$ ), charge ( $Z$ ), and electronegativity (EN) of the modifiers.

In some compositions, the electrostatic ( $Z/r$ ) ratio is satisfactory for the estimation of thermal expansion. However, this does not seem to hold over wide compositional ranges. Hormadaly therefore proposed a model that accounted for both electrostatic ( $Z/r$ ) as well as covalent (EN) contributions of the modifiers ( $i$ ) through a new parameter,  $\beta_i$ , defined below.

$$\beta_i = Z_i (\text{EN})_i / r_i \quad (\text{Eqn. 5.1})$$

Hormadaly utilized the  $\beta$  parameter combined with an empirical approach for the calculation of TCE of a glass by utilizing a standard modifier in the glass for which the TCE is known. The TCE of an unknown glass containing modifiers other than those of the standard can be estimated by quantifying the difference of the  $\beta$  parameter between the unknown and standard glasses. Hormadaly chose lead as the standard modifier.

The effect of partial or complete substitution for lead in the glass can be evaluated by using the value of the parameter  $\gamma$  which is defined by

$$\gamma_i = (\beta_i - \beta_{Pb}) / \beta_{Pb} \quad (\text{Eqn. 5.2})$$

For complete substitution of a modifier for PbO, the thermal expansion can be calculated as

$$\alpha_s = (1 - \gamma_i) \alpha_0 \quad (\text{Eqn. 5.3})$$

where  $\alpha_0$  = the linear thermal expansion of the lead glass.  
 $\alpha_s$  = the linear thermal expansion for the modified glass.

For the partial substitution for PbO in the glass

$$\frac{\Delta \alpha}{\alpha_0} = \frac{\alpha_s - \alpha_0}{\alpha_0} = - \sum \frac{X_i}{X_{PbO}^0} \gamma_i \quad (\text{Eqn. 5.4})$$

where  $X_{PbO}^0$  = mole percent PbO in the lead glass before substitution

Rearranging equation 5.4 gives

$$\alpha_s = \left[ 1 + \left( - \sum \frac{X_{MO}^i}{X_{PbO}^0} \gamma_i \right) \right] \alpha_0 \quad (\text{Eqn. 5.5})$$

where  $X_{MO}^i$  = mole percent for the  $i$ th modifier oxide substituting for PbO.

Utilizing the above equations, the thermal expansions of glasses containing metal oxides could be estimated to roughly +/- 10% of their actual value [52]. This model only holds for silica based glasses, and treats alumina as a glass former rather than a modifying oxide.

### **5.2.2. Methodology: TCE Calculation of Residual Glasses in 96% Alumina**

Similar to the dissolution of alumina, the thermal expansion of the residual glass in 96 weight percent alumina could not be directly calculated. Again an extrapolation method was used to approximate upper and lower bounds. Utilizing the ranges of alumina dissolution, quantitative ratios of the crystalline phases present in the 96 weight percent samples, and knowledge of the crystallization potential of the barium aluminosilicate samples at high alumina addition, the TCE of the residual glasses was approximated.

Quantitative analysis of 0, 50, and 75 weight percent alumina samples found that as alumina addition increased, the temperatures at which complete crystallization occurred also increased. In samples with 50 weight percent alumina addition, this maximum occurred at 1340°C, while for 75 weight percent alumina samples maximum crystallization occurred at 1540°C. Therefore it was assumed that the 96 weight percent alumina samples fired at 1640°C crystallize to near completion. This assumption is not only important in the calculation of the thermal expansion of the residual glass, but will be needed in the modeling of new glass compositions.

The thermal expansion of the residual glass was calculated with the aid of a computer spreadsheet. In this spreadsheet, an increment of the maximum amount of alumina dissolution was added to the original alumina content of a given composition. The other constituents were then normalized with respect to this addition. The resultant

composition was assumed to be that of the glass before the onset of crystallization. The amounts of the crystalline phases present were introduced as functions of the percent crystallization. This was done in a manner by which the calculated quantitative ratio of these phases was kept constant based on that determined from the x-ray diffraction data. The percent crystallization was used in the spreadsheet to calculate the relative amounts of each crystal phase and residual glass, as well as the composition and thermal expansion of the residual glass. The composition was calculated as described in Section 4.4.1., and the TCE by Hormadaly's model. The percent crystallization was continually and incrementally adjusted for a particular alumina increment until the residual glass had become deficient in a constituent. At this point maximum crystallization was theoretically attained. The TCE and percent crystallization were recorded, and the process reiterated for the next increment of alumina dissolution. This process was continued until the entire range of dissolution had been addressed.

### **5.2.3. Results and Discussion**

Figures 5.4, 5.5, and 5.6 provide the percent maximum crystallization and TCE of the residual glass plotted versus the amount of alumina in the glass and crystalline phases for compositions 2a, 3b, and 4a with an  $\text{SiO}_2/\text{BaO}$  ratios equal to 4, 2, and 1.4, respectively. A shaded region representing the bounds from the alumina dissolution, and a line showing the thermal expansion of alumina when compared to glassy phases are also indicated. Hormadaly's glass TCE model is based on room temperature to 300°C data, and thus a value of 6.2 ppm/°C for alumina over the same temperature range was used for comparison.

Figure 5.4 shows that for glass composition 2a with  $\text{SiO}_2/\text{BaO}=4$ , the amount of crystallization of mullite and celsian in a 3 to 2 ratio is a minimum at the lower bound of alumina dissolution and a maximum near the upper limit. The thermal expansion of the residual glass over the range of alumina dissolution is slightly lower than that of alumina except near the peak of maximum crystallization where the glass TCE becomes greater than alumina.

Figure 5.5 shows that the stoichiometric glass (3b) results in a residual glass with a thermal expansion significantly greater than that of alumina. However, within the limits of alumina dissolution the amount of crystallization of mullite and celsian in a 3 to 2 ratio is limited to no greater than 60 percent. Figure 5.6 shows that the thermal expansion of the residual glass of the high barium content composition 4a ( $\text{SiO}_2/\text{BaO} = 1.4$ ) is greater than alumina and the crystalline phase hexacelsian. The crystallization of hexacelsian reaches a maximum of 80 percent approximately between both bounds. Both the thermal expansion and crystallization results will be utilized in the computational modeling of new compositions.



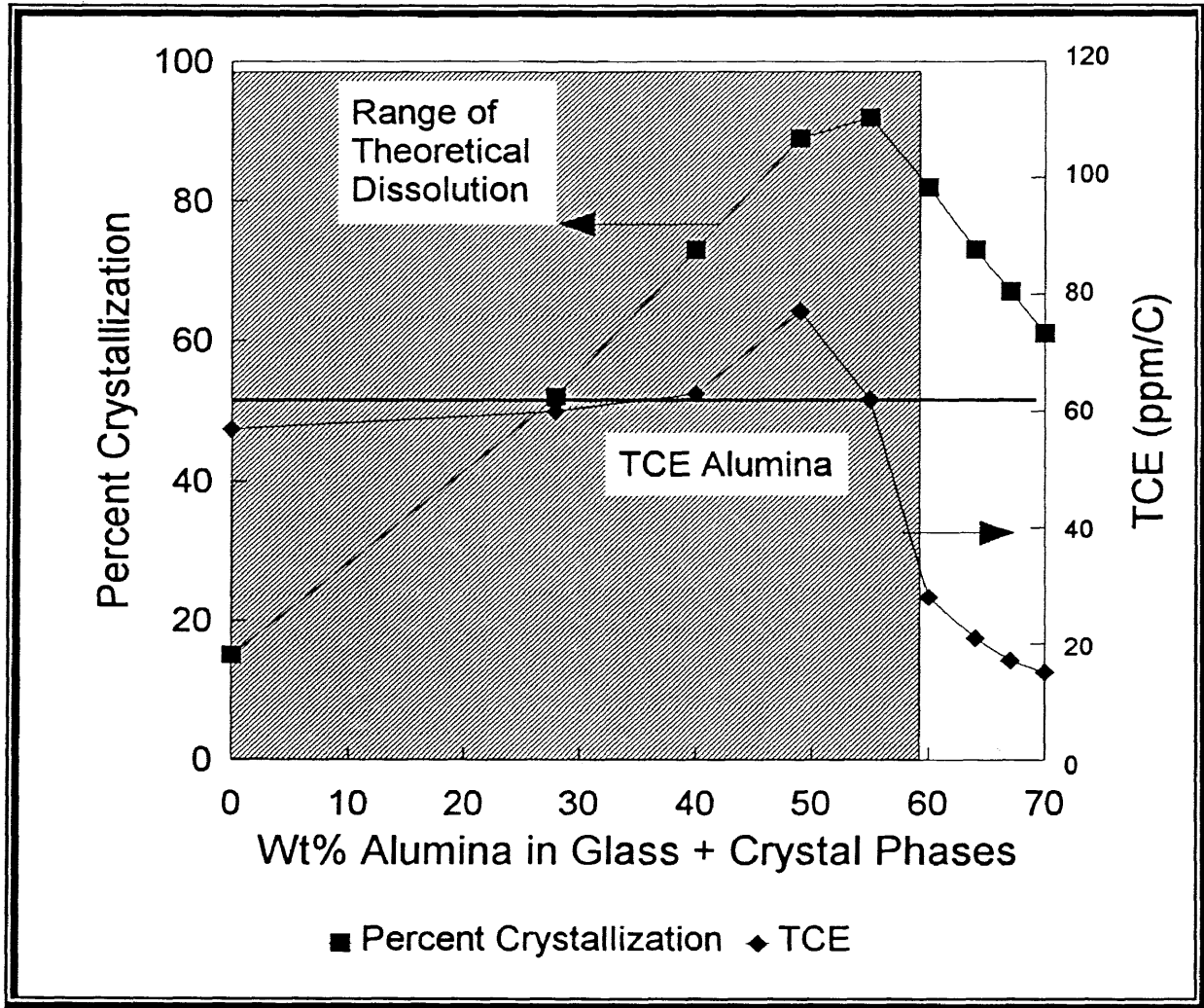


Figure 5.4. Theoretical calculations of the percent maximum crystallization (mullite/celsian = 1.5) and the resulting TCE of the residual glass plotted versus the weight percent alumina in the residual glass and crystalline phases for composition 2a with  $\text{SiO}_2/\text{BaO} = 4$ . The TCE line for alumina (6.2 ppm/°C) is plotted for comparison with the TCE of the residual glass

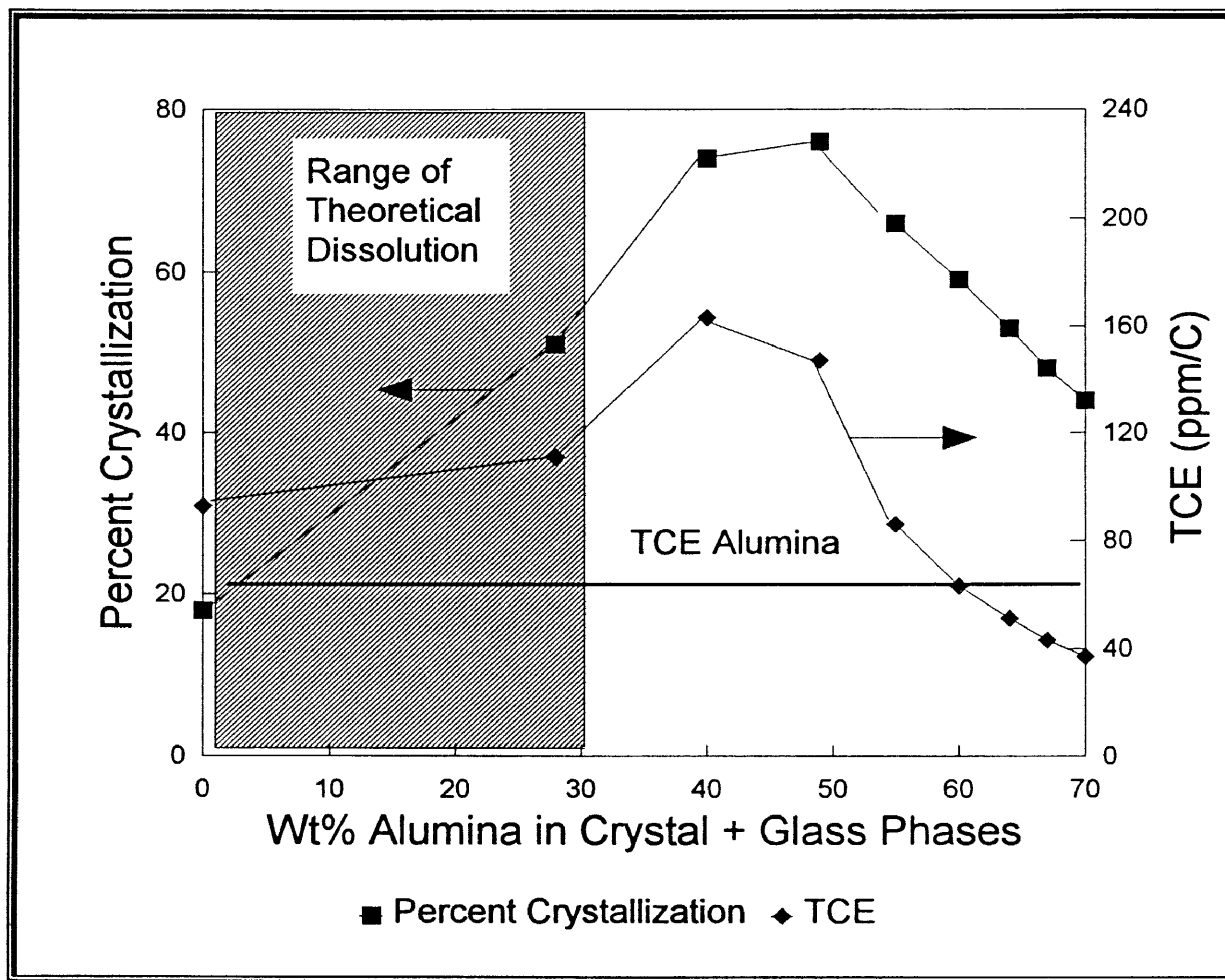


Figure 5.5. Theoretical calculations of the percent maximum crystallization (mullite/celsian = 1.5) and the resulting TCE of the residual glass plotted versus the weight percent alumina in the residual glass and crystalline phases for composition 3b with  $\text{SiO}_2/\text{BaO} = 2$ . The TCE line for alumina (6.2 ppm/°C) is plotted for comparison with the TCE of the residual glass

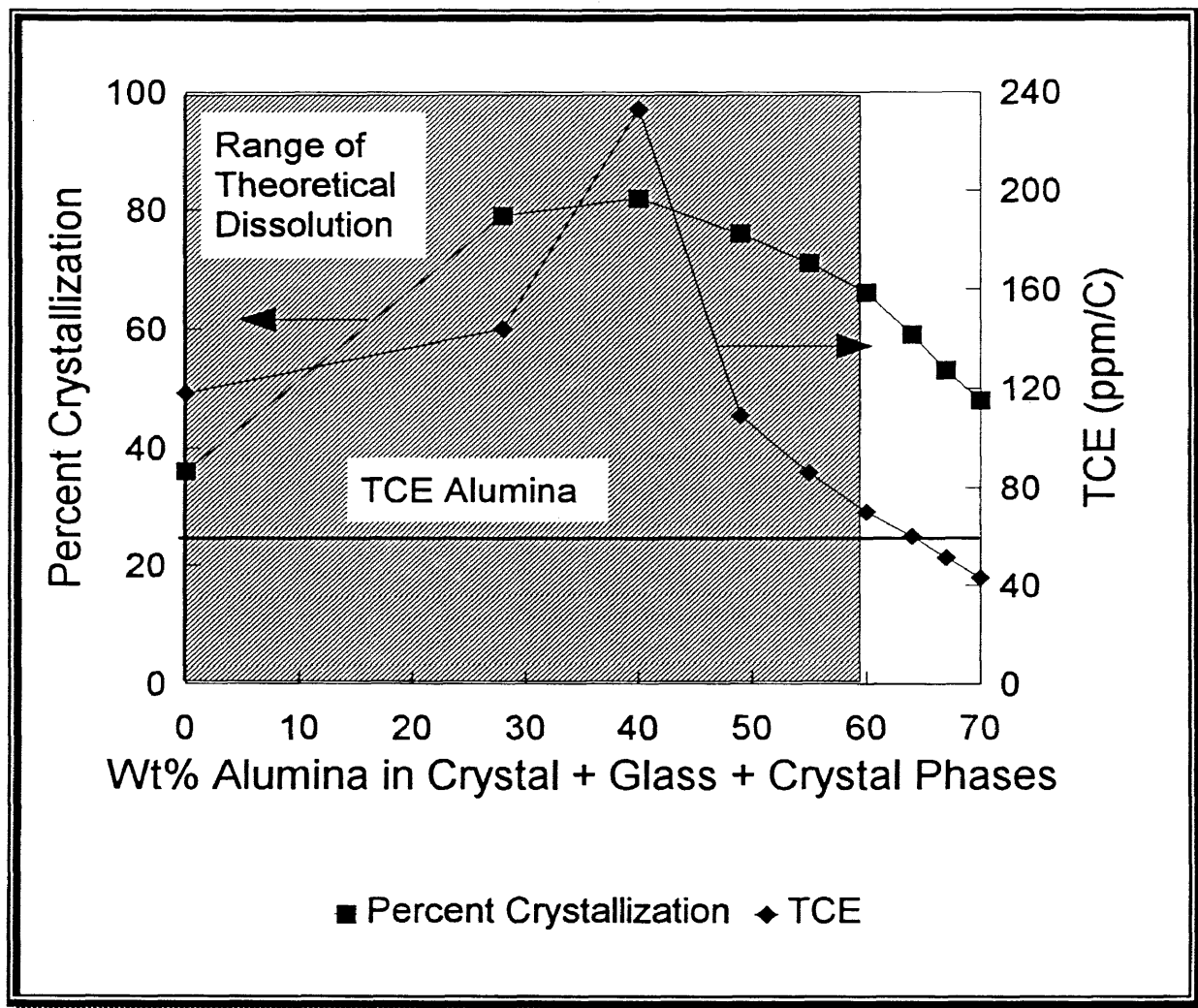


Figure 5.6. Theoretical calculations of the percent maximum crystallization (hexacelsian=1) and the resulting TCE of the residual glass plotted versus the weight percent alumina in the residual glass and crystalline phases for composition 4a with  $\text{SiO}_2/\text{BaO} = 1.4$ . The TCE line for alumina (6.2 ppm/oC) is plotted for comparison with the TCE of the residual glass

### 5.3. Compositional Modeling for Thermal Expansion Mismatch Analysis

Up to this point in the chapter results have been discussed providing information about the thermal expansion of the crystalline and glassy phases in samples containing various barium aluminosilicate glasses and 96 weight percent alumina. Based on this information, the potential of satisfying the six types of thermal expansion models (presented in Chapter One) will be summarized in this section. Table 5.3 summarizes these six models.

Table 5.3. Thermal Expansion Mismatch Models

Phase	1	2	3	4	5	6
Alumina	High	High	Med	Med	Low	Low
Glass	Med	Low	High	Low	High	Med
Crystal	Low	Med	Low	High	Med	High

Two methods were used to develop compositions to satisfy these models. The first was by direct observation of the results of various compositions from this and previous work by N. W. Chen [5]. The second was by the computational modeling method described in the last section, which was based on the utilization of J. Hormadaly's model for the estimation of thermal expansion. In the next two sections the use of each of these methods is described.

### 5.3.1. Direct Observation

The direct observation method was relatively straightforward. The thermal expansion coefficients of all crystalline and glassy phases were compared to each other and to alumina. The crystalline phases were compared to a thermal expansion value of 8.7ppm/°C (25-900°C) [53] for alumina, while the glassy phases were compared to a value of 6.2 (25-300°C) [4] because Hormadaly's model was based on glass data from this temperature range. The values of the crystalline and glassy phases were compared by approximating the adjustments necessary for the differences in the temperature range of measurement. Once all comparisons were made, the model that each composition satisfied was defined. A composition was defined as "mixed" if it could not satisfy a model. This occurs if a sample contains two crystalline phases, and the thermal expansion of one crystal phase is either higher or lower than a second phase (alumina or glass), while the second crystalline phase shows an opposite trend. Such a phenomena can be described by a sample that crystallizes both hexacelsian and celsian. Hexacelsian is higher in thermal expansion than alumina, while celsian is lower. Such mixed phenomena can occur around the TCE of the residual glass. An example is when both mullite and celsian crystallize. Both of these phases are distinctly lower in TCE than alumina. The TCE of the residual glass may however lie between the values for these two phases, resulting in a "mixed" model. In this example the composition can be redesigned through computational modeling to potentially adjust the thermal expansion to the range desired.

### 5.3.2. Computational Modeling

Computational modeling was required in two cases. The first was when redesign was required because of a mixed type model occurring. The second was in the design of

an entirely different composition to attain a model not addressed by any previous results. In either case, a composition that potentially crystallized a crystalline phase of the desired thermal expansion was selected as a base composition. The thermal expansion of the glass was then modeled to attain a desired thermal expansion through the utilization of Hormadaly's model.

The thermal expansion of the residual glass is controlled by the modifying oxides present in the glass. Figure 5.7 gives the relative thermal expansion of a silicate glass with various modifier oxide additions. Also shown in this figure is the relative thermal expansion of alumina as compared to the glass. MgO and ZnO are oxides that have a low contribution to the thermal expansion, while CaO, SrO, and BaO have high contributions to the thermal expansion when compared to alumina. The contribution in general increases with increasing ionic radius.

New glass compositions were modeled through the aid of two computerized spreadsheets. The first spreadsheet calculated the residual glass composition that needed to be redesigned. The most logical starting point was through the utilization of a composition that had been previously analyzed and for which the residual glass thermal expansion had been calculated. If the TCE needed to be lowered, the amount of alumina dissolution was chosen correlating to the greatest value of thermal expansion found within the range of alumina dissolution from Figures 5.4 - 5.6. The opposite was done for a composition that needed to be increased in thermal expansion. The amount of crystallization corresponding to this value of thermal expansion was used as the

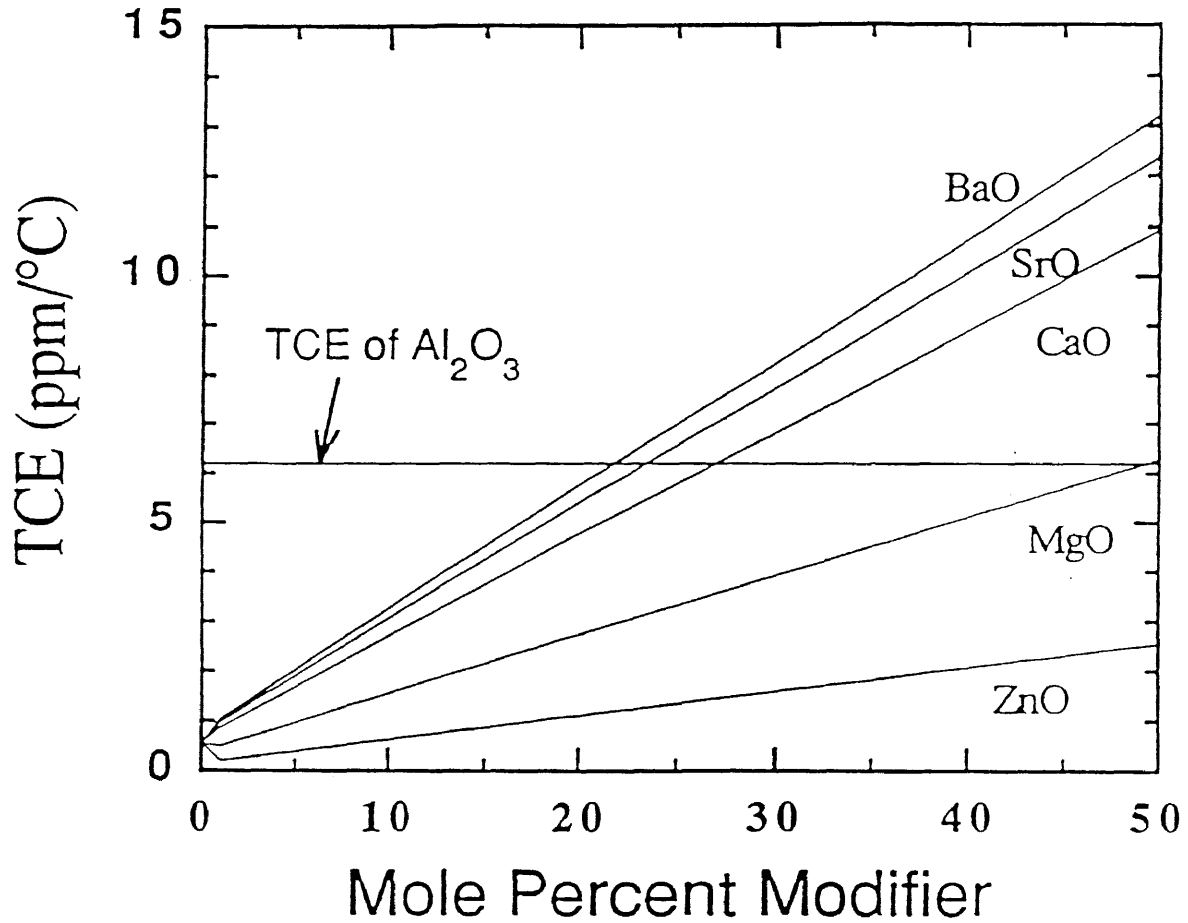


Figure 5.7. The TCE of a silicate based glass plotted versus modifier addition calculated from Hormadaly's [52] model. A TCE value of 6.2 ppm/°C for alumina is also plotted for comparison.

quantitative amount of crystalline phase present. Then by taking this amount of alumina dissolution and adding it to the original composition, normalizing for the addition, the starting glass composition could be calculated. By subtracting the amount of constituents that entered the crystalline species, the residual glass composition that needed to be redesigned could be attained. The composition of this residual glass and the quantitative amounts of crystalline phases present were then utilized in a second spreadsheet. This spreadsheet allowed the user to change the composition of the final residual glass to attain a desired thermal expansion. Once each change was made, a starting glass composition was then calculated by the spreadsheet.

In the alteration of the residual glass composition several design factors were important to maintain the crystalline phase composition originally present and the ease of glass formation and processing. The additions of modifiers to control the thermal expansion was limited to less than ten mole percent. With such small additions the tendency to crystallize phases with unwanted modifiers was reduced. If large increases or reductions in thermal expansion were needed, small additions of several different modifiers was used instead of a large addition of a single modifier. If further reduction or increase was needed, the amount of  $\text{SiO}_2$  could be altered, however the  $\text{SiO}_2$  content was kept above 40 mole percent to ensure good glass formability.

### **5.3.3. Results and Discussion**

The crystallization results of samples 2a, 3b, and 4a from this work, and compositions 29, 34, and 35 from the work by N.W. Chen[5] are presented in Table 5.4. This table summarizes the crystalline phases present and the corresponding TCE's, the



TCE's of the residual glass, and the resultant model satisfied. Table 5.5 provides the starting glass compositions.

Table 5.4. Results of Direct Observation

	Compositions Evaluated		
	2a	3b	4a
Crystal Phases	Mullite/Celsian	Mullite/Celsian	Hexacelsian
TCE Crystal (ppm/°C)	5.5-2.7	5.5-2.7	>8.0
TCE Glass	6.4	9.0	12.0
Model Satisfied	3	3	5

Table 5.4.(cont) Results of Direct Observation

	Compositions Evaluated		
	29	34	35
Crystal Phases	Mullite/Celsian	Spinel/Gahnite	Mullite/Celsian
TCE Crystal Phases (ppm/°C)	5.5-2.7	7.4	5.5-2.7
TCE Glass	8.4	2.7	3.8
Model Satisfied	3	2	Mixed

Table 5.5. Starting Glass Compositions of Observed Compositions

Mole%	2a	3b	4a	29	34	35
SiO <sub>2</sub>	73.30	59.25	52.26	55.14	43.72	53.66
Al <sub>2</sub> O <sub>3</sub>	7.42	8.73	9.63	10.00	10.00	10.00
MgO					22.88	7.45
CaO				5.41		
SrO				5.42		
BaO	18.28	29.02	37.11	23.03		21.18
ZnO					22.19	5.99
Na <sub>2</sub> O	1.00	1.00	1.00	1.00	1.21	1.71
MoO <sub>3</sub>		2.00				

From these results three models can be directly satisfied. Three more models however need to be satisfied. The first is that of high alumina, medium glass, and low crystal thermal expansion (Model 1). This may be satisfied through the compositional manipulation of composition 35, which was mixed, with the values of TCE of the crystalline phases higher and lower than that of the glass. Also composition 2a can be redesigned to lower the residual glass TCE. The second model that needed to be satisfied was that of high crystal TCE, medium alumina, and low glass (Model 4). This can be satisfied by redesigning composition 4a, which contains a high TCE crystal phase and a high residual glass. The value of the TCE of the residual glass must be reduced. The final model that needed to be satisfied was model 6, where a high crystal phase TCE, a medium

glass, and low alumina TCE are required. Again, this model can be achieved through redesigning composition 4a.

Utilizing the information above, computational modeling of the selected phases was conducted. To satisfy model 1, compositions 35 and 2a were redesigned. ZnO was added to composition 2a to reduce the thermal expansion of the glass. This resulted in a TCE of 5.8ppm/°C for the residual glass, and the composition was labeled as composition 5. MgO was added to composition 35, while ZnO was removed. The effect of such manipulation raised the thermal expansion of the residual glass of composition 35 to 5.6ppm/°C. This composition was then labeled as composition 6. Model 4 was satisfied through the manipulation of composition 4a. Since an extremely large decrease in TCE was required, the manipulation of SiO<sub>2</sub> and ZnO modifiers were implemented. This resulted in a thermal expansion of 6.0ppm/°C for the residual glass. The resultant composition was then labeled composition 8. The final model that needed to be satisfied was model 6. Again composition 4a was redesigned, and only consisted of additions of ZnO. This resulted in a thermal expansion of 7.9ppm/°C, and the composition was labeled as composition 7. Table 5.6 summarizes the results of compositional modeling.

Table 5.6. Results of Compositional Modeling

Composition	5	6	7	8
Basis	2a	35	4a	4a
TCE glass	5.8ppm/°C	5.6	7.9	6.0
Mole %				
SiO <sub>2</sub>	47.66	58.73	50.14	45.32
Al <sub>2</sub> O <sub>3</sub>	33.54	10.00	10.00	10.00
MgO		11.18		
SrO				
BaO	11.63	12.26	28.41	24.02
ZnO	6.62	4.61	10.99	19.83
Na <sub>2</sub> O	0.55	3.21	0.47	0.83

#### 5.4. Summary and Conclusions

In this chapter compositions satisfying various states of thermal expansion between the alumina, glass, and crystalline phases were satisfied. To do this a variety of assumptions and theoretical calculations had to be made. The first was that the amount of dissolution of alumina into the glass phase was less than that of 75 weight percent alumina additions at a temperature of 1640°C, and greater than that of the alumina present in the original glass. This information along with previous quantitative results was used to

calculate the theoretical crystallization and TCE of the residual glass over the range of alumina dissolution. Through direct observation of the results of the TCE of both the crystalline phases and the residual glass over the dissolution range of interest, three models of thermal expansion mismatch were satisfied. Compositions directly observed were those utilized in this work as well as that of N. W. Chen. To satisfy the remaining three models, a computational methodology was utilized. The method basically altered the residual glass of an existing composition to produce a new composition. Four new compositions were provided through this method, satisfying the three remaining mismatch models. Although the starting compositions will potentially form glasses easily based on their silica contents, a qualification step is required in order to (1) insure that appropriate densification occurs, and (2) that the modeled crystalline composition of each is maintained. Such a qualification and the effect of the resultant mismatches on the properties of strength and toughness will be discussed in the next chapter.

## **CHAPTER 6**

### **PHASE 4: THE EFFECT OF THERMAL EXPANSION MISMATCH ON THE MECHANICAL PROPERTIES OF 96% ALUMINA**

The three previous phases of this research resulted in the development of compositions that satisfy the six thermal expansion mismatch models through direct observation of quantitative results and computational modeling of selected compositions. In this chapter, an investigation of the stress states developed and the effect of such stress states on the mechanical properties of 96 weight percent alumina is described. In section one the experimental methods used for qualification and preparation of samples for mechanical property testing is presented. The analytical methodology by which the samples were tested is provided in section two. The results of mechanical property testing and the stress states which developed in the tested samples are then discussed in section three, followed by a summary of the results in section four.

#### **6.1. Experimental Methodology**

In phase three of this thesis a variety of glass compositions were found to satisfy the six models of thermal expansion mismatch. The oxide content of these glass compositions and the models they satisfy are summarized in Table 6.1.

Table 6.1. Compositions Satisfying the Six Thermal Expansion Mismatch Models

Mole%	5	6	34	2a	3b	29	8	4a	7
SiO <sub>2</sub>	47.66	58.73	43.72	73.30	59.25	55.14	45.32	52.26	50.14
Al <sub>2</sub> O <sub>3</sub>	33.54	10.00	10.00	7.42	8.73	10.00	10.00	9.63	10.00
MgO		11.18	22.88						
CaO						5.41			
SrO						5.42			
BaO	11.63	12.26		18.28	29.02	23.03	24.02	37.11	28.41
ZnO	6.62	4.61	22.19				19.83		10.99
Na <sub>2</sub> O	0.55	3.21	1.21	1.00	1.00	1.00	0.83	1.00	0.47
MoO <sub>3</sub>					2.00				
Model	1	1	2	3	3	3	4	5	6

All of the above glass compositions were prepared into powders and mixed with 96 weight percent alumina. They were then qualified through both density and qualitative x-ray diffraction analysis. The compositions satisfying this qualification were then prepared for strength and toughness testing. The details outlining each of the above segments of the experimental work are presented in the following sections.

### 6.1.1. Preparation of 96 Weight Percent Alumina Powders

The glass compositions were melted and prepared into glass powders using the procedure described in Section 3.2.1. The glass powders were then combined with a calcined 99.8% alumina (ALCAN C-72 low-soda alumina) and a 25 wt% polyethylene

glycol ( Carbowax Sentry 8000 Powder NF) binder, 75% water solution. The exact composition of this mixture is presented in Table 6.2.

Table 6.2 Amount of Constituents in 96% Alumina Powders

C-72 Alumina	192 grams
Carbowax / H <sub>2</sub> O	5 grams or 20 milliliters
Glass Powder	8 grams

This mixture was then added to 325 milliliters of reagent grade alcohol and ball milled with 500 grams of 1/4 inch alumina cylinders in a 1000 milliliter plastic bottle for eight hours. The slurry was then screened and pan dried in an oven at 50°C for 72 hours. The remaining powder was then sieved through a 325 $\mu$ m screen to remove large agglomerates.

### 6.1.2. Compositional Qualification

The 96 weight percent alumina powders for each composition were pressed at 13.5 ksi in a steel die into 60 mm X 7 mm X 3 mm modulus of rupture (MOR) bars. Isosteric acid was used as a die lubricant and the hold time was one minute. The optimum firing conditions of these 96 weight percent alumina MOR bars had been previously determined by N. W. Chen [5]. Samples were fired in a 1700°C Lindberg Box Furnace at 1640°C for four hours. Heating and cooling rates were 160 and 200°C/hour respectively.

The fired samples were qualified through density and qualitative x-ray diffraction analysis. Density was measured using Archimedes method. The percent theoretical density was then calculated, from the ratio of the measured bulk densities to the



theoretical density of alumina (3.99 g/cc). Samples were then prepared and analyzed using qualitative x-ray diffraction as described in Section 3.3.

The compositions were qualified if they satisfied the following conditions.

- (1) The percent theoretical density of the sample had to be equal to or greater than 92 percent of the theoretical value.
- (2) Qualitative x-ray diffraction had to confirm the presence of expected crystalline phases. No additional unexpected phases were allowed.

A percent theoretical density of 92 percent is considered satisfactory in 96 weight percent alumina samples for mechanical property testing. At this value no open porosity is perceived to exist. All porosity is closed porosity. Attaining a dense ceramic reduces the tendency of initiating fracture at a pore in the material.

The presence of expected crystalline phases in a given sample was vital in ensuring the correct states of thermal expansion mismatch for which the composition was designed. If unexpected crystalline phases are found, the state of the thermal expansion of the crystal may or may not change. However, with such crystallization occurring, the state of thermal expansion of the residual glass usually changes.

### **6.1.3. Fabrication of Mechanical Test Specimens**

Samples passing qualification were then prepared into MOR bars for mechanical property testing. Twenty bars of each composition were prepared as described in Section 6.1.2. Ten bars were prepared for flexural strength measurement and ten for indentation

toughness. All MOR bars were ground to military standard 1942A configuration B (3 mm X 4mm X 50mm). The ten bars prepared for indentation toughness were then polished to a 4RA surface finish. All machining and polishing was provided by Chand Kare Technical Ceramics, 2 Coppage Drive, Worcester, MA 01603-1252.

## **6.2. Analytical Methodology**

Once all MOR bars were fabricated, machined, and polished, mechanical testing was conducted. The testing that was conducted included flexural strength and fracture toughness. Generally, the fracture toughness and flexural strength for a group of tests are affected by several variables, including the rate of loading, the test environment, specimen and fixture size, and the sample fabrication process. The specimen size and fabrication process have been previously reported. The following sections will detail the fixture utilized for testing, the loading and test conditions, and the calculation procedures applied for flexural strength and toughness analysis.

### **6.2.1. Fixture Used for Mechanical Testing**

A schematic figure of the four point - 1/4 - point bend fixture is shown in Figure 6.1. The 1/4 is specified by a description of the distance between the outer support points and the inner points that is 1/4 the distance between the two outer support points. Bearing A in the fixture is such that it will not pivot about the x-axis. Such independent pivoting of the bearing cylinders is required if specimens are sintered, heat-treated, or oxidized. Such treatments often result in warping and irregular surfaces. The pivots allow for even load distribution across the sample. Samples were prepared to configuration B

dimensions (3 mm X 4 mm X 50 mm). During testing, the samples were loaded in such a manner so that an equal amount of sample overhang was present beyond each of the outer pins. Also the samples were centered below the applied load.

### 6.2.2. Flexural Strength

Once all bars were machined and ground to specification, ten bars of each qualified composition were tested in flexural strength. The ceramic bars were placed into the 4 point - 1/4 - point bend fixture. Small cotton balls were placed around the fixture to prevent pieces of the sample from flying out of the fixture upon fracture. This was done to preserve the primary fracture pieces. The specimens were then loaded in compression at a rate of 0.01 inches per minute, using a computer interfaced and controlled Instron. Once completed, the maximum load was recorded and used to calculate the flexural strength. The flexural strength,  $S$ , in four point bending was calculated by computer using the following equation.

$$S = 3PL / 4bd^2 \quad (\text{Eqn. 6.1})$$

where,

$P$  is the load in kilograms,

$L$  is the length of the span in meters as defined by Figure 6.1,

$b$  is the width of the bar in meters, and

$d$  is the thickness of the bar in meters.

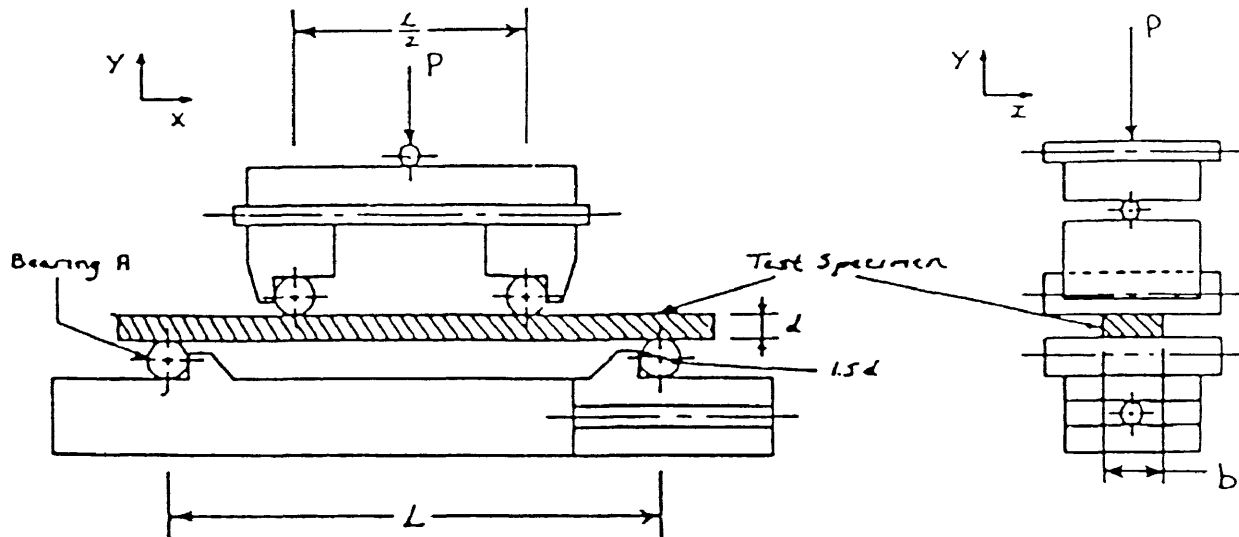


Figure 6.1. General schematic of a four-point - 1/4 - point fixture suitable for sintered, heat treated, or oxidized specimens [54].

### 6.2.3. Fracture Toughness

The measurement of the fracture toughness was based on the fracture toughness indent procedure [55]. Ten polished specimens from each composition were first indented with three Vickers indents. A Zwick 3212 was used for the indentation, with a load of 20 Kg. The indenter was calibrated to a 20 second free fall and a 10 second dwell time on the specimen. As shown in Figure 6.2 the three indentations were evenly spaced between the loading pins of the fixture.

The indented area was then covered with a red dye and immediately wiped with methanol. The dye penetrated the cracks to facilitate the measurement of the initial crack length. The crack length on the X-Y plane was denoted  $2C$  as shown in Figure 6.2.  $2C$

was viewed at 100X using cross polarizers on an optical microscope, and measured through the use of a LECO 2000 image analysis system that was linked to the microscope.

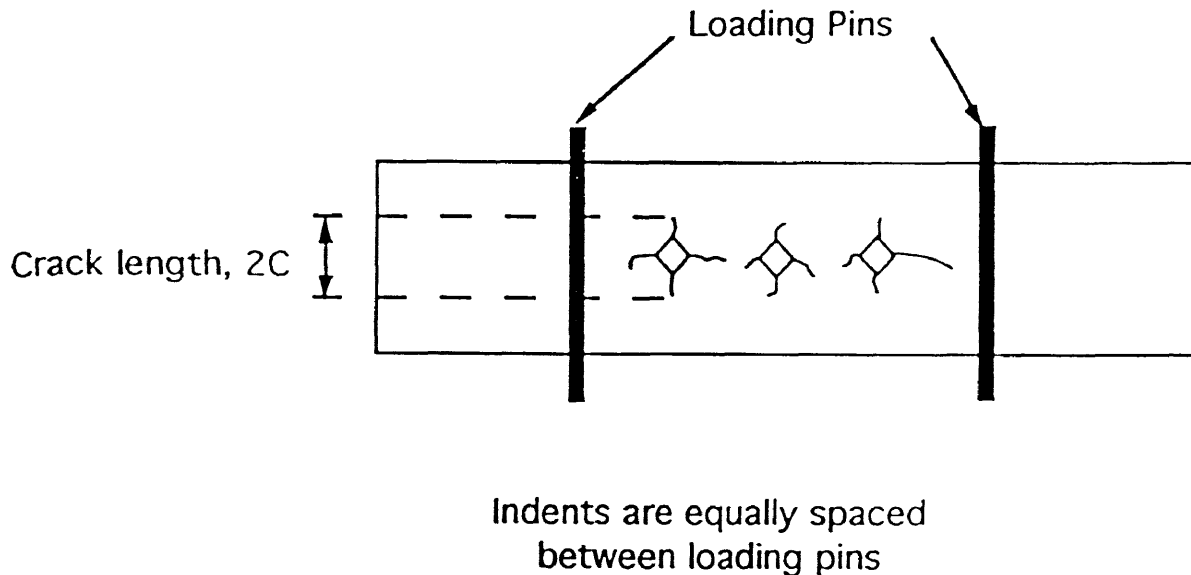


Figure 6.2. Diagram of MOR specimens with location of indents shown. The measured crack length,  $2C$ , is also shown [56].

The indented MOR bars were loaded into a four point -1/4 - point bend fixture, so that upon loading the indented surface was in tension. The samples were then loaded at a rate of 0.05 inches/minute, until fracture. The samples were then carefully handled and saved for fractography and crack extension analysis.

Dye was then reapplied to the remaining two indentations on the fractured specimens. The crack after fracture, denoted  $2C'$ , was then measured as described above. Problems in reading crack lengths were experienced by samples that were porous. This porosity led to increased dye penetration and decreased visibility of the crack under the

microscope. Measurements of the actual crack, or half-penny, were attempted. However due to the fracture surface eradicity, the measurements could not be made.

Fracture toughness ( $K_{IC}$ ) was then calculated utilizing three techniques: (1) Indentation Strength in Bending Toughness (ISB), (2) Initial Crack Length Toughness (ICB), and (3) Crack Length Extension Toughness (ICA). The  $K_{ISB}$  was calculated using the maximum breaking strength of the fracture test. The  $K_{ICB}$  was computed using the breaking strength as well as the initial crack length  $C$ , while  $K_{ICA}$  was calculated through the breaking strength, the initial crack length  $C$ , and the crack length after fracture  $C'$ . The representative equations for each calculation are as follows.

#### Indentation Strength in Bending (ISB)

$$K_{ISB} = 0.885 \times (B \times 10^6 I_1)^{3/4} \times 10^{-6} \quad (\text{Eqn. 6.2})$$

#### Initial Crack Length (ICB)

$$K_{ICB} = C^{1/2} \times B \times 2.02 - 0.68 \quad (\text{Eqn. 6.3})$$

#### Crack Length Extension (ICA)

$$K_{ICA} = (2C/2 + 2C'/2)^{1/2} \times B \times 2.02 - 0.68 \quad (\text{Eqn. 6.4})$$

where,

B is the breaking strength in MPa,

$I_1$  is the indent load (equal to 5.81 for a 20 Kg indent load),

C is the initial crack length,

C' is the crack length after fracture, and

K is the fracture toughness in  $\text{MPa} \cdot \text{m}^{-1/2}$ .

Note that all values of 2C and 2C' were the averaged values of all indentations on a sample.

#### **6.2.4. Fractography**

After evaluating the fracture toughness of the samples the fracture surfaces were analyzed. This was done utilizing a JEOL model JXA 840 scanning electron microscope. The fracture bars were mounted vertically (fracture surface parallel to table top) in a conductive Bakelite mount. Gold was then sputtered onto the fracture surface of each specimen to enhance the image quality and to reduce charging. Representative photomicrographs were taken at 500X and 1000X for each composition. The resultant fracture surface was then labeled as either intergranular or transgranular. Intergranular fracture is characterized by a tortuous path with a consequent increase in fracture surface area. Transgranular fracture is characterized by a decrease in surface area and a planar path.

### 6.3. Results and Discussion

#### 6.3.1. Compositional Qualification

Nine compositions were qualified for thermal expansion mismatched modeling. Table 6.3 summarized the results of the qualification. The summary includes the percent theoretical density attained, crystalline phases present, crystalline phase predicted, the  $\text{SiO}_2/\text{BaO}$  ratio of the starting glass, and the mismatch model satisfied.

Table 6.3. Results of Qualification Analysis

C=Celsian, M=Mullite, H=Hexacelsian

Composition	5	6	34	2a	3b
% $\rho_{th}$	92%	93%	94%	92%	85%
Phases Present	C,H,M	C,M	G,S	C,M	C,M
Phases Predicted	C,M	C,M	G,S	C,M	C,M
$\text{SiO}_2/\text{BaO}$	4.1	4.8	---	4.0	2.0
Model	1	1	2	3	3

Table 6.3. Results of Qualification Analysis

C=Celsian, M=Mullite, H=Hexacelsian

Composition	29	8	4a	7
% $\rho_{th}$	94%	93%	94%	93%
Phases Present	C,M	H,C	H	H,C,M
Phases Predicted	C,M	H	H	H
$\text{SiO}_2/\text{BaO}$	2.4	1.9	1.4	1.8
Model	3	4	5	6



All of the compositions except composition 3b satisfied the density requirements. Of the remaining compositions 6, 34, 2a, 29 and 4a satisfied the crystalline phase requirements. These compositions were then used in 96% aluminas for mechanical property testing. Models 1, 2, 3, and 5 were satisfied by these compositions. Future research is needed to further modify the compositions to achieve mismatch models 4 and 6.

### **6.3.2. Stress states**

As discussed in Chapter One, a variety of stress states can be developed between the intergranular glass, crystalline phases, and alumina matrix. When the alumina contracts more than the crystalline and glassy phases, it is put into a state of tension, while the glass and crystalline phases are put into compression. The opposite stress states are developed when the crystalline and glassy phases contract more than the alumina.

The stress states developed above only consider interactions between the alumina and the intergranular phases as a whole. This thesis however considers the interaction of each phase alone. Utilizing the states of TCE of a phase as defined by the TCE mismatch models, the following stress states were derived. Any phase that is higher in thermal expansion than the others is in a state of pure tension. When the TCE of the given phase is lower than the others, it is in pure compression. However, when a phase is defined as having a medium type expansion, it undergoes a mixed stress state. The mixed phase is in a partial state of compression from the high TCE phase, and a partial state of tension from the low TCE phase. From here on, these three stress states are referred to as T, C, and TC representing tensile, compressive, and tensile-compressive (mixed) stress states respectively.

The definitions of these various stress states were applied to the phases of the compositions satisfying the qualification. Table 6.4 summarizes the states of stress for the crystalline, glassy, and alumina phases of each composition. These stress states will allow for a better understanding of the mechanical property results discussed later in this chapter.

Table 6.4. Resultant Stress States of Qualified Compositions

Composition	4a	29	2a	6	34
Glass	T	T	T	TC	C
Crystal	TC	C	C	C	TC
Al <sub>2</sub> O <sub>3</sub>	C	TC	TC	T	T
SiO <sub>2</sub> /BaO	1.4	2.4	4.0	4.8	---

### 6.3.3. Fractography

The samples tested in the indentation strength of bending, or toughness test, yielded the fracture surfaces pictured in Figures 6.3-6.7. Each surface was labeled as transgranular, intergranular, or mixed. The fractography results were then combined with the stress states, obtained in section 6.3.2, and the SiO<sub>2</sub>/BaO ratios of each composition, as summarized in Table 6.5.

Table 6.5. Resultant Stress States of Qualified Compositions

Stress States	Composition	4a	29	2a	6	34
	Glass	T	T	T	TC	C
	Crystal	TC	C	C	C	TC
	Al <sub>2</sub> O <sub>3</sub>	C	TC	TC	T	T
SiO <sub>2</sub> /BaO		1.4	2.4	4.0	4.8	---
Fracture		I	I(Tr)	M	Tr(I)	Tr

The symbols I, Tr, and M represent intergranular, transgranular, and mixed fracture respectively. Symbols in parenthesis represent secondary or partial modes of fracture that are occurring.. In Figure 6.8 the fracture modes are plotted as a function of SiO<sub>2</sub>/BaO ratio. When the SiO<sub>2</sub>/BaO ratio is low (BaO content high), an intergranular type fracture occurs, because the residual glass has a high thermal expansion, and thus is in tension. As the SiO<sub>2</sub>/BaO ratio increases, or as the glass composition becomes silica rich, a transgranular mode of fracture dominates, because the residual glass has a low thermal expansion causing it to be in compression. A similar type of correlation of fracture mode with thermal expansion of the residual glass was previously seen in aluminas with varying MgO/CaO ratio [5,57-59]. High MgO containing glasses have low TCE resulting in transgranular fracture, while high CaO glasses have high TCE resulting in intergranular fracture.

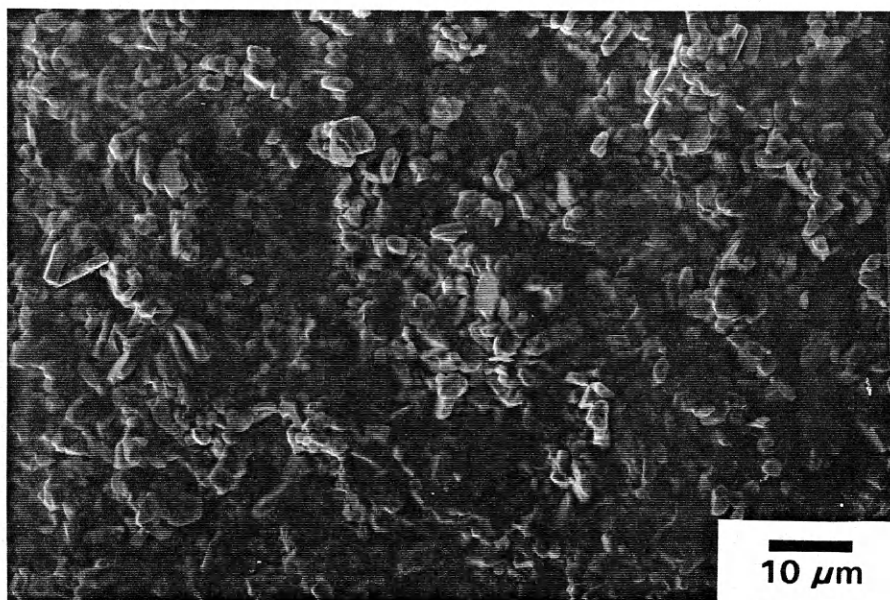


Figure 6.3. Photomicrograph at 1000X of composition 4a, showing intergranular fracture.

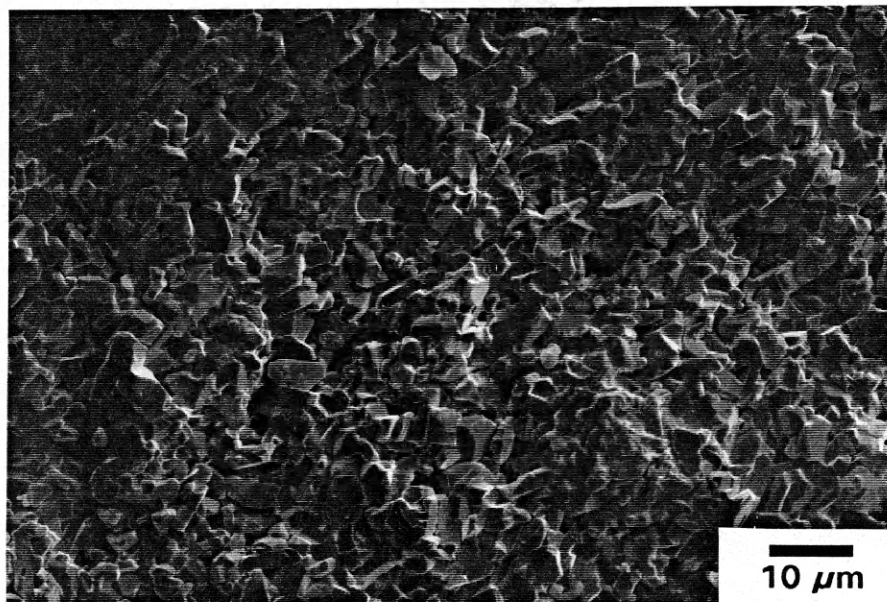


Figure 6.4. Photomicrograph at 1000X of composition 29, showing predominantly intergranular fracture with aspects of transgranular fracture.

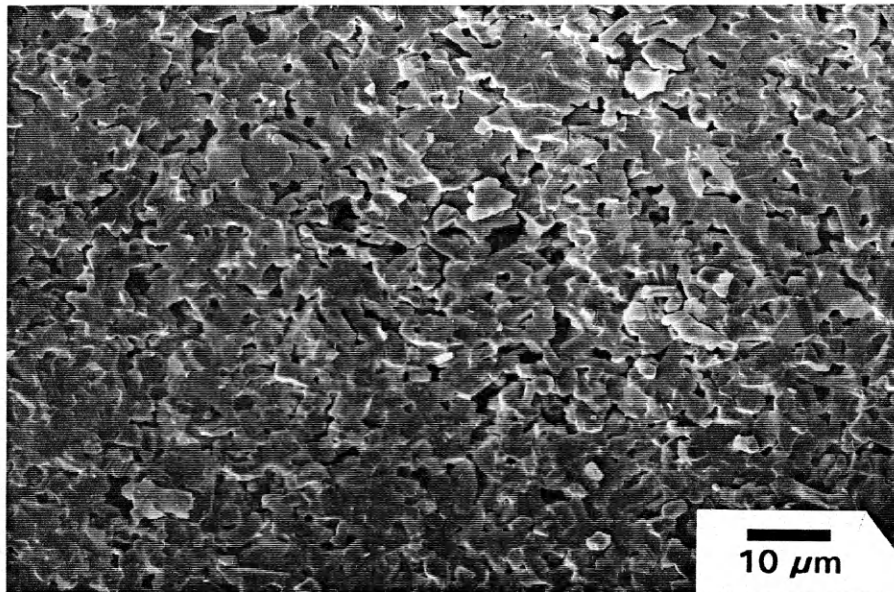


Figure 6.5. Photomicrograph at 1000X of composition 2a, showing predominantly mixed intergranular and transgranular fracture.

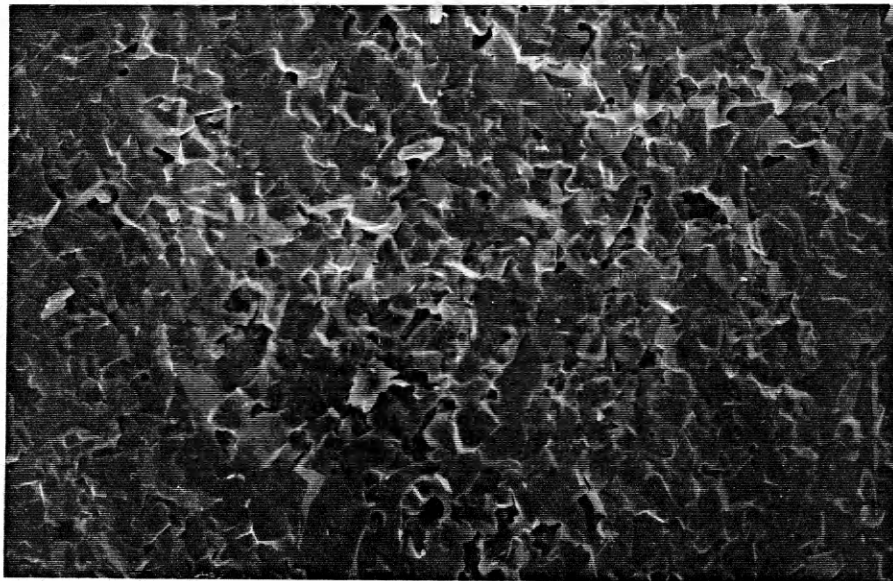


Figure 6.6. Photomicrograph at 1000X of composition 6, showing predominantly transgranular fracture with aspects of intergranular fracture.

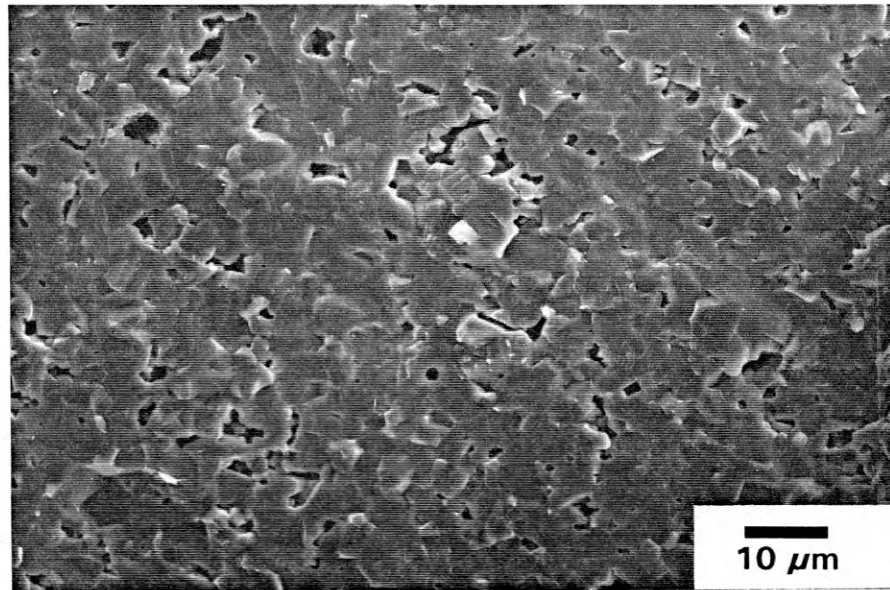


Figure 6.7. Photomicrograph at 1000X of composition 34, showing transgranular fracture.

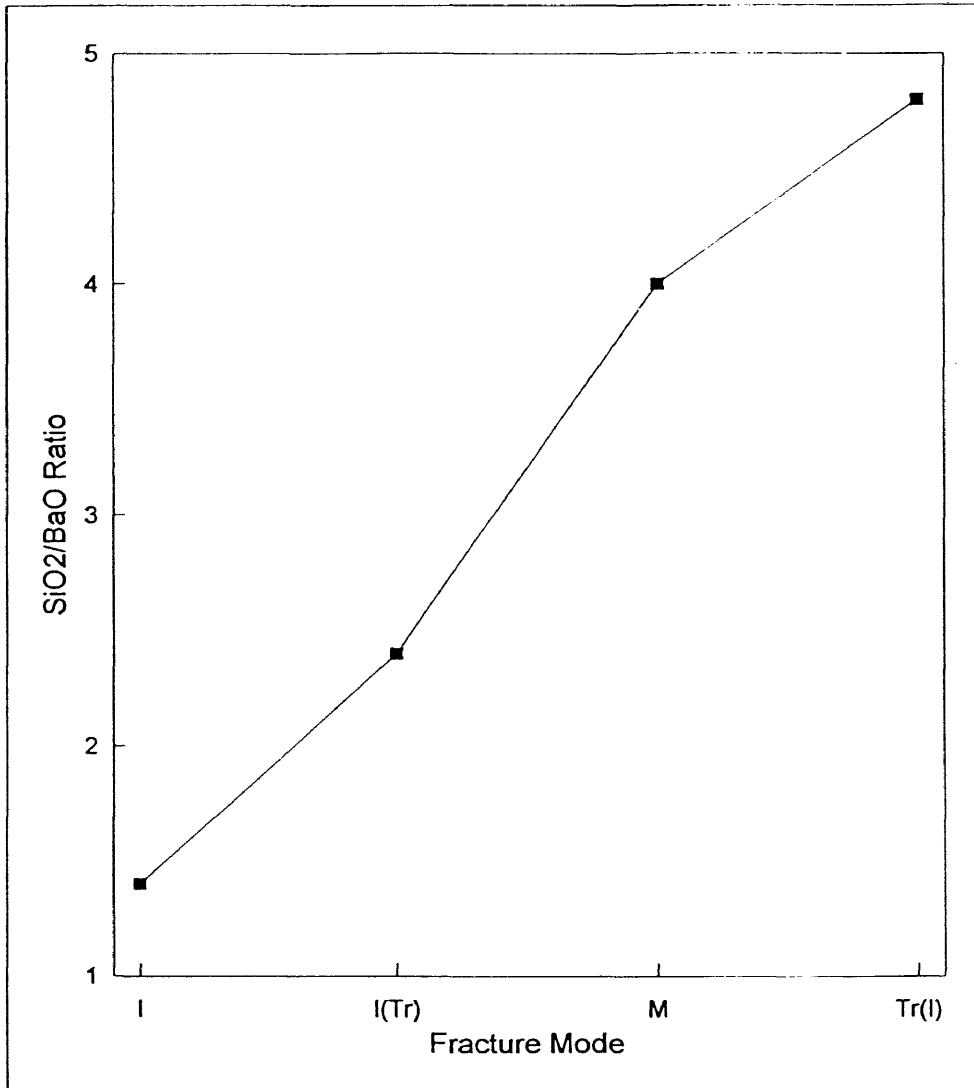


Figure 6.8. Modes of fracture plotted versus the SiO<sub>2</sub>/BaO ratio.

Mixed modes of fracture occur in compositions 29, 2a, and 6 [I(Tr), M, and Tr(I)]. The stress states from Table 6.5 will be used to analyze these modes with crack propagation assumed to occur in all phases under tension. The stress states reveal that up to two phases in one sample are in some state of tension, and thus may be involved in the propagation of a crack.

In composition 29, an intergranular type fracture occurs, with aspects of transgranular fracture. The intergranular nature comes from the glass which is in tension while the transgranular fracture occurs through crack propagation in the alumina which is in tensile-compression. In composition 6 transgranular fracture occurs, with aspects of intergranular fracture. Alumina, which is in pure tension leads to the transgranular component, while some crack propagation through the grain boundary glass leads to the intergranular component. The glass in composition 6 is in tensile-compression. In both compositions 29 and 6 the crystalline phase is in pure compression.

Composition 2a shows stress states similar to that of composition 29. However, the differences in TCE between the glass and the alumina is significantly less in 2a compared to that of 29. This appears to cause less distinct tensile stresses to form in the glass, leading to a more purely mixed intergranular/transgranular fracture surface.

#### **6.3.4. Flexural Strength**

Figure 6.9 shows the results of the flexural strength testing with the states of residual stress as well as the mode of fracture also listed. As can be seen from Figure 6.9, the flexural strength increases as the fracture mode changes from intergranular to transgranular. This is because the intergranular strength is controlled by the glass, while the transgranular strength is controlled by the alumina. Because alumina is stronger than



most glasses, transgranular fracture results in higher flexural strength. High strength therefore correlates to alumina being in pure tension, while the residual glass is in pure compression. Low strength correlates to alumina being in pure compression while the glass is in pure tension.

The flexural strength is also found to increase with increasing  $\text{SiO}_2/\text{BaO}$  ratio. In addition, the crystallization of celsian or hexacelsian seems to have an impact on strength. Composition 4a crystallized hexacelsian, and had a markedly lower strength than that of compositions 29 and 2a, two compositions crystallizing celsian.

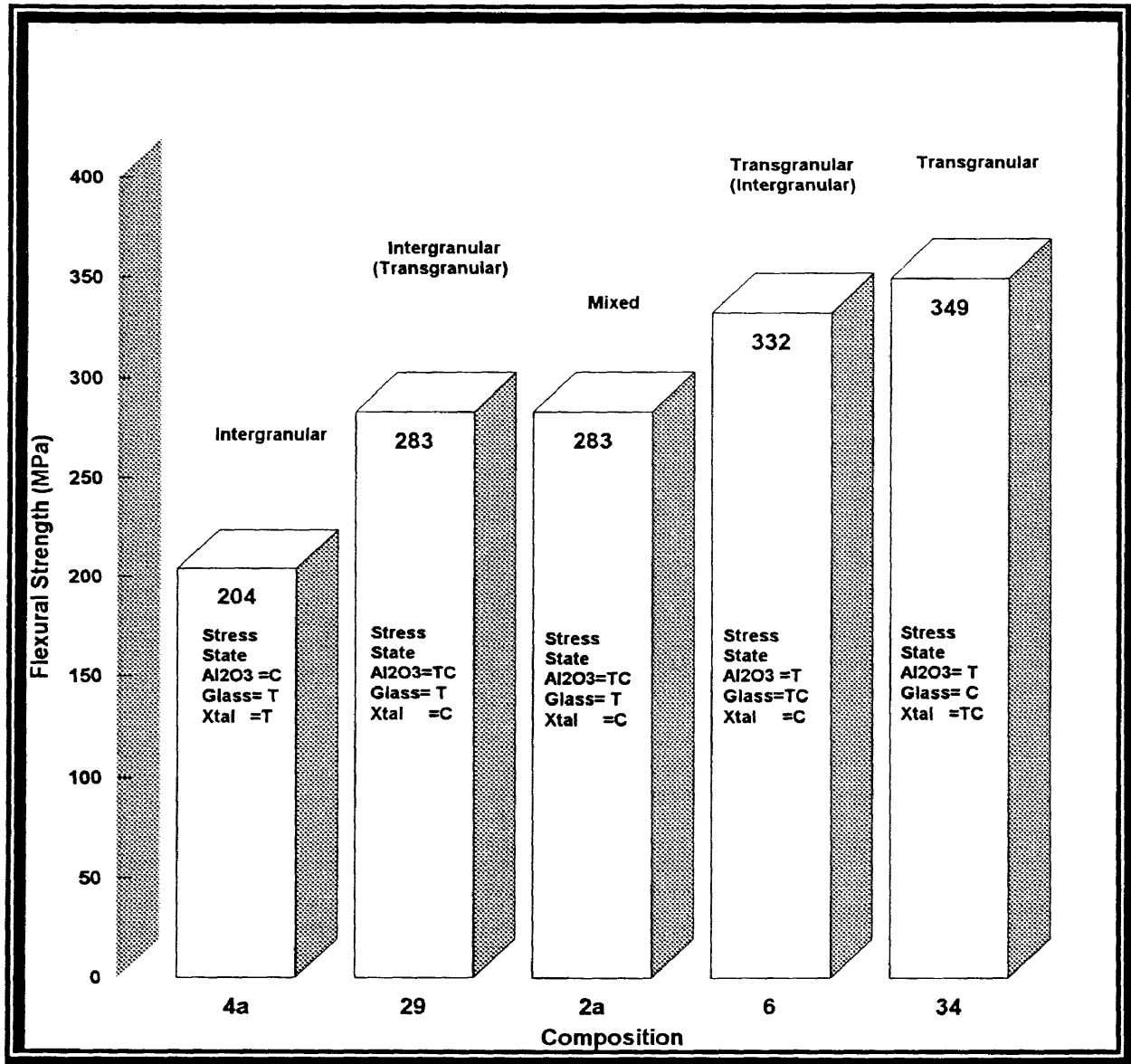


Figure 6.9. Results of the flexural strength analysis as a function of composition. Also provided are the modes of fracture, as well as the states of residual stress. The experimental error of all flexural strength results was  $\pm 28$  MPa.

### 6.3.5. Fracture Toughness

Figure 6.10 shows the results of the fracture toughness measurements of  $K_{ISB}$ ,  $K_{ICB}$ , and  $K_{ICA}$ . Values of  $K_{ICB}$  and  $K_{ICA}$  were difficult to obtain for compositions 4a and 2a, because the samples absorbed too much dye, making the reading of the crack impossible. Because all values of toughness could not be calculated for all samples, the values of  $K_{ISB}$  were used for comparison.

Figure 6.11 represents  $K_{ISB}$  for all compositions and similar to Figure 6.9, summarizes the states of residual stress as well as the modes of fracture. An opposite trend is seen in fracture toughness when compared to the flexural strength. Intergranular fracture results in higher toughness than that of transgranular fracture. Because the path in intergranular fracture is much more tortuous, a greater amount of energy is needed to propagate the crack, thus leading to a higher toughness. Transgranular fracture is very planar, leading to a lower fracture surface area. Because the surface area of the crack is much smaller a decrease in fracture toughness occurs.

The states of residual stress control the mode of fracture, and therefore the fracture toughness. As the residual glass increases in TCE, so does its residual state of tension, leading to intergranular fracture or high fracture toughness. On the other hand, as the glass decreases in TCE, it becomes compressed, leading to transgranular fracture or low fracture toughness. Compositions of mixed stress state, however can achieve a higher toughness than purely intergranular fracture.

Composition 29 has the highest value of fracture toughness,  $4.5 \text{ MPa} \cdot \text{m}^{-1/2}$ , and shows the effect of such mixed behavior. The residual glass is in pure tension, and the alumina is in tensile compression. Because the alumina and glassy phases share a common

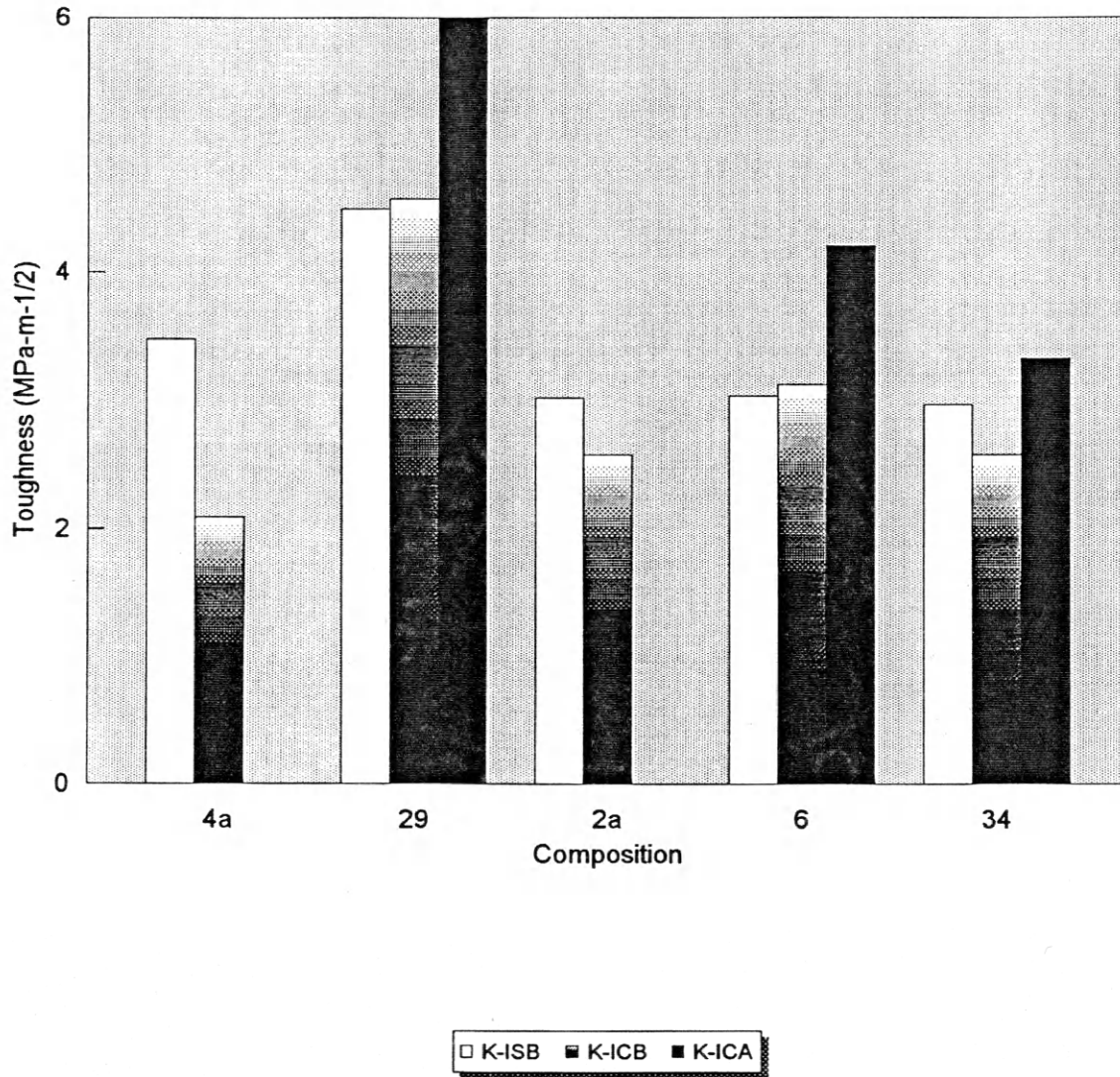


Figure 6.10. Results of fracture toughness showing  $K_{ISB}$ ,  $K_{ICB}$ , and  $K_{ICA}$ .

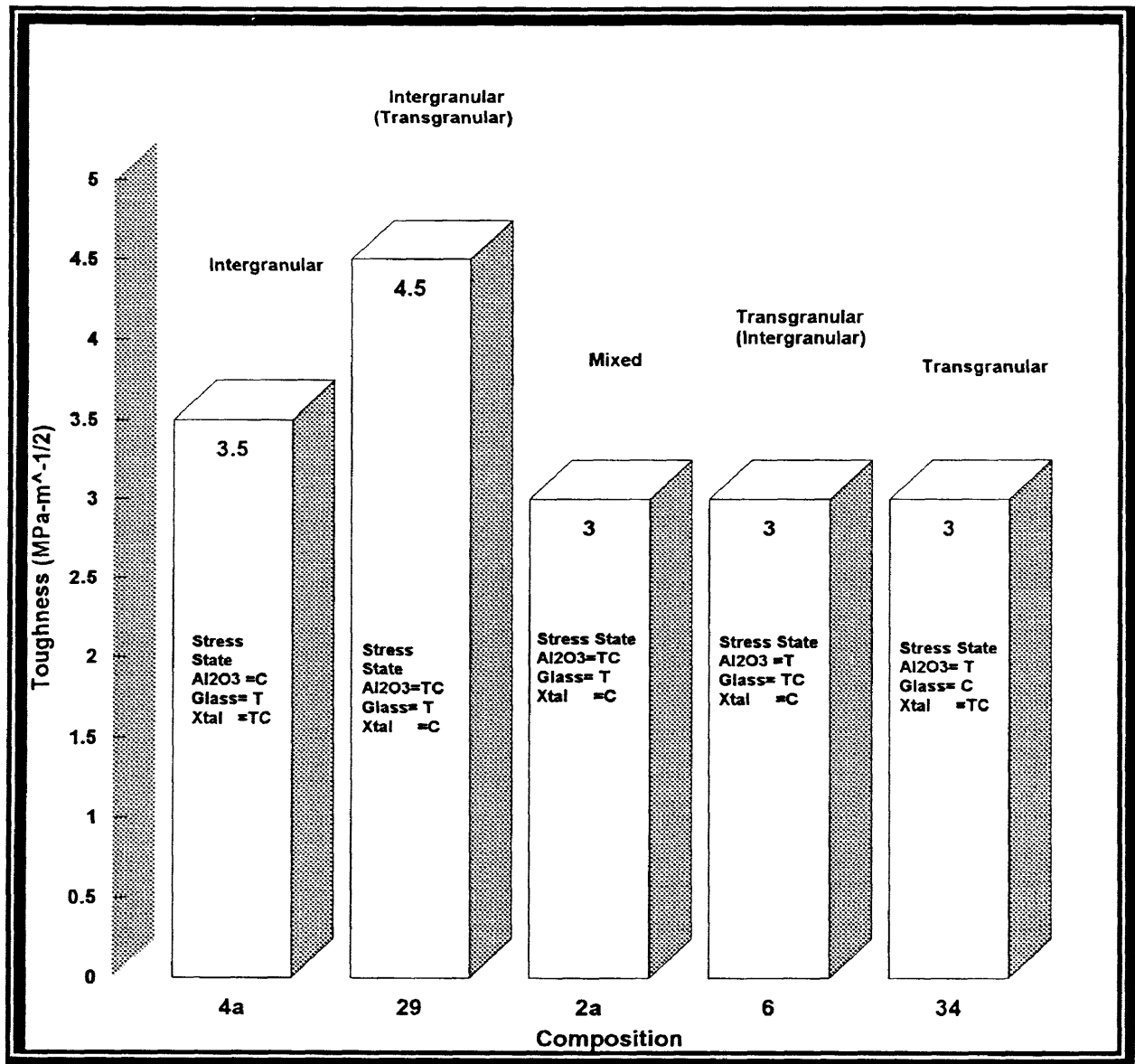


Figure 6.11. Summary of the fracture toughness ( $K_{ISB}$ ) results as a function of composition. Also provided are the modes of fracture, as well as the states of residual stress.

grain boundary, the crack may propagate through both phases. The result of such crack propagation is equivalent to that of a particulate toughened glass, where the transgranular sections of fracture through the alumina increase the toughness because (1) they are also in a partial state of compression from the glass phase TCE, and (2) the alumina is tougher than the glass. The degree to which the crack propagates through the alumina is assumed to be a function of the magnitude of TCE mismatch, and is a topic for future research.

Increases in toughness only occur when intergranular fracture through the glass is the dominant component of fracture. When a predominantly transgranular type of fracture occurs, the toughness is governed by the toughness of the alumina, and partial crack propagation through the glass does not seem to increase it.

Composition 4a, shows that differences in crystalline phase content can dramatically change the toughness. When comparing the fracture toughness and residual stresses of composition 4a to that of 29 one finds that in both cases the residual glass is in tension. The crystalline phases however are not the same. 4a crystallized hexacelsian, leading to a tensile-compressive state, while 29 crystallized celsian which was in a totally compressive state. The difference in crystallization resulted in two distinct fracture patterns. Celsian in composition 29, put the alumina in tensile-compression, allowing crack propagation through the partially compressed alumina. Hexacelsian, with its large TCE, put the alumina into total compression, significantly decreasing the toughness when compared to composition 29.

#### 6.4. Summary and Conclusions

The mechanical properties of 96% alumina ceramics were investigated as a function of thermal expansion mismatch, and the resulting residual stress states. Five different samples were qualified satisfying four models of thermal expansion mismatch. The results show that as the residual glass increased in thermal expansion an intergranular type of fracture was dominant. Transgranular fracture was dominant when the TCE of the glass was low. Stress states further develop this result by showing that during intergranular fracture the glass is in tension and the alumina is in compression, while the crystalline phase is in tensile-compression. Transgranular fracture was defined as having the opposite trend in stress, with the crystalline phase in a state of tensile-compression.

Strength was found to be greatest when transgranular fracture occurred and was controlled by the strength of alumina. Toughness was high when intergranular fracture occurred. Composition 29 was an exception to this conclusion. In composition 29 intergranular fracture dominates, but transgranular fracture also occurred through the tensile-compressed alumina phase, which increased the fracture toughness. Such a toughening mechanism is similar to that of a particulate reinforced glass.

In both properties of strength and toughness, the crystallization of celsian versus hexacelsian appeared to also have an effect. The hexacelsian containing composition 4a had a dramatically lower strength than that of the celsian containing compositions. When a high TCE glass was formed, hexacelsian decreased toughness by putting the alumina in compression, while celsian increased the toughness by putting the alumina into tensile compression.

## CHAPTER 7

### CONCLUSIONS AND FUTURE WORK

Qualitative and quantitative x-ray diffraction were conducted on a number of barium aluminosilicate glass compositions as a function of heat treatment temperature, alumina addition, and composition. The effect of  $\text{MoO}_3$  as a nucleating agent was also investigated. The qualitative x-ray diffraction results show that the  $\text{MoO}_3$  additions did not change the crystallization characteristics of the base compositions, except in samples with 96 weight percent alumina addition fired at a temperature of  $1640^\circ\text{C}$ . In the low  $\text{SiO}_2$  content glass (4a) fired at low temperatures, hexacelsian was the dominant crystalline phase. Firing between  $1340$  and  $1640^\circ\text{C}$  resulted in celsian as the dominant phase, especially for the stoichiometric  $\text{SiO}_2$  content glasses (3a, 3b). Above  $1640^\circ\text{C}$  hexacelsian was the dominant phase in the low  $\text{SiO}_2$  glasses (4a), while mullite and celsian dominated in all other compositions.

The quantitative results show that in all compositions, the amount of alumina dissolution increases with temperature. Areas of 100% crystallization are attainable in the 50 and 75 weight percent alumina additions, occurring at  $1340$  and  $1540^\circ\text{C}$ , respectively. This temperature increase signifies that increased alumina additions decrease the rate of crystallization. The amount of residual glass was found to reach a minimum at the maximum crystallization temperatures, and then increase with higher temperature heat treatment. The increase in residual glass is attributed to the increased dissolution of both the alumina and celsian phases back into the glass, and is confirmed by the residual glass



compositions. In general the stoichiometric composition ( $\text{SiO}_2/\text{BaO}=2$ ) crystallized more than the nonstoichiometric compositions with  $\text{SiO}_2/\text{BaO}$  ratios of 4 and 1.4.

Crystallization was limited in these nonstoichiometric compositions because of the depletion of oxide constituents from the glass compositions. The crystallization of the high  $\text{SiO}_2/\text{BaO}$  composition was limited by the amount of BaO, while the low  $\text{SiO}_2/\text{BaO}$  composition was limited by the amount of  $\text{SiO}_2$ . However solid solutions of celsian phases with silica as well as the crystallization of non-celsian phases increased the crystallization of these nonstoichiometric compositions to near 100%.

The results from both qualitative and quantitative x-ray diffraction were then used to theoretically estimate the amount of alumina dissolution and the TCE of the residual glass phase of 96 weight percent aluminas. This was done in an effort to satisfy the six models of thermal expansion mismatch through direct observation as well as through computational modeling. Three models of thermal expansion were satisfied by the original barium aluminosilicate glass compositions, while computational modeling produced four new compositions, potentially satisfying the remaining thermal expansion mismatch models. Of these seven compositions only five satisfied both the density and crystalline phase requirements, producing four types of thermal expansion mismatch.

The residual stress states of the five compositions were then defined and the mechanical properties of flexural strength and fracture toughness were tested. The results show that as the residual glass increased in thermal expansion an intergranular type of fracture was dominant. Transgranular fracture was dominant when the TCE of the glass was low. Stress states further develop this result by showing that during intergranular fracture the glass is in tension and the alumina is in compression, while the crystalline

phase is in tensile-compression. Transgranular fracture was defined as having the opposite trend in stress state, with the crystalline phase in a state of tensile-compression.

Strength was found to be greatest when transgranular fracture occurred and was controlled by the strength of alumina. Toughness was high when intergranular fracture occurred, except in composition 29. This composition was found to have a dominant intergranular type fracture, but transgranular fracture through the tensile-compressed alumina phase increased its toughness. Such a toughening mechanism is similar to that of a particulate reinforced glass, and is seen as being the optimum toughening mechanism in thermal expansion mismatch toughening of 96 weight percent aluminas.

A process was observed during this research known as transient glass phase processing (TGPP). This process crystallized the residual glass entirely by dissolving crystalline alumina into an alumina deficient glass. This shifted the glass composition toward the stoichiometric celsian composition, and resulted in 100% crystallization. TGPP can be used as a novel processing route in the synthesis of stoichiometric crystalline species, composite materials, and novel glass-ceramics at lower processing temperatures than are normally required. Future work in the synthesis of such crystalline phases as anorthite and cordierite using this method are presently being pursued by D.B. Price and C.Y. Kim in thesis research at CSM. Work in such an area would encompass the rate of crystallization and alumina dissolution as a function of alumina content and temperature.

Other future work includes the mechanical testing of the completely crystallized samples with 50 and 75 weight percent alumina additions. This is of interest, because such a material would have applications in high temperature composites, electronics, structural ceramics, as well as biomaterials. The high temperature properties of 96 weight percent aluminas with barium aluminosilicate glass addition is also of interest, because celsian and

mullite have very good high temperature properties, and the degree of crystallization can be controlled to minimize the amount of residual glass phase. Reducing the amount of residual glass phase will potentially improve the high temperature properties of alumina, such as creep, which will expand the uses and durability of alumina in high temperature environments.

## REFERENCES CITED

1. D. R. Clarke, "High-Temperature Deformation of a Polycrystalline Alumina Containing an Intergranular Glass Phase", *J. Mat. Sci.*, 20, 1985.
2. W. A. Zdaniewski and H. P. Kirchner, "Toughening of a Sintered Alumina by the Crystallization of the Grain Boundary Phase", *Adv. Ceram. Mat.*, 1 [1], 1986.
3. M. Claussen, J. Steeb, and R. F. Pabst, "Effect of Induced Microcracking on the Fracture Toughness of Ceramics", *Ceramic Bulletin*, 56 [6], 1977.
4. M. P. Harmer, H. M. Chan, and G. A. Miller, "Unique Opportunities for Microstructural Engineering with Duplex and Laminar Ceramic Composites", *J. Am. Ceram. Soc.*, 75 [7], 1992.
5. N. W. Chen, "Control of Intergranular Glass Phase in Commercial Aluminas", M.S. Thesis No. T-4328, Colorado School of Mines, Golden, CO, 1992.
6. N. W. Chen, M. W. Krutyholowa, M. J. Haun, T. K. Brog, D. G. Wirth, J. D. Sibold, and K. R. McNerney, "The Effect of Thermal Expansion Mismatch between the Intergranular Glass and Crystal Phases on the Fracture toughness of Alumina Ceramics", *Advanced Ceramic Matrix Composites, Ceramic Transactions*, The American Ceramic Society, Westerville, OH, 1994.
7. N. W. Chen, M. J. Haun, T. K. Brog, D. G. Wirth, J. D. Sibold, and K. R. McNerney, "Crystallization Behavior of the Intergranular Glass Phase in Commercial Aluminas: Part II - Effects of Thermal expansion Mismatch on Mechanical Properties", to be published.
8. C. H. Drummond, III, and N.P. Bansal, "Crystallization Behavior and Properties of BaO-Al<sub>2</sub>O<sub>3</sub>-SiO<sub>2</sub>. Glass Matrices", *Ceram. Eng. Sci. Proc.*, 11 [7-8], 1990.
9. L. D. Hart, *Alumina Chemicals*, The American Ceramic Society, Columbus, OH, 1990.

10. W. H. Gitzen, Alumina as a Ceramic Material, The American Ceramic Society, Columbus, OH, 1970.
11. D. G. Wirth, "Ceramic Substrates", Ceramics and Glasses, Engineered Materials Handbook, Volume 4, ASM.
12. Communication with J. Sibold, Coors Ceramics Company, Nov. 1993.
13. D. W. Richerson, Modern Ceramic Engineering, Marcel Dekker, Inc., NY, 1992.
14. Coors Ceramics Company, "Application Guide", Coors Ceramics Company, Golden, CO.
15. S. Hampshire, "Engineering Properties of Nitrides", Ceramics and Glasses, Engineered Materials Handbook, Vol. 4, ASM.
16. O. Kwon and G. L. Messing, "Kinetic Analysis of Solution-Precipitation During Liquid-Phase Sintering of Alumina", *J. Am. Ceram. Soc.* 73 [2], 1990.
17. J. E. Marion, C. H. Hsueh, and A. G. Evans, "Liquid-Phase Sintering of Ceramics", *J. Am. Ceram. Soc.*, 70 [10], 1987.
18. W. D. Kingery, "Densification During Sintering in the Presence of a Liquid Phase. 1. Theory", *J. Appl. Phys.*, 30 [1], 1950.
19. W. D. Kingery, "Densification During Sintering in the Presence of a Liquid Phase. 2. Experimental", *J. Appl. Phys.*, 30 [1], 1950.
20. R. B. Heady and J. W. Cahn, "An Analysis of the Capillary Force in Liquid-Phase Sintering of Spherical Particles", *Metall. Trans.*, 1 [1], 1970.
21. R. B. Heady and J. W. Cahn, "An Analysis of the Capillary Force in Liquid-Phase Sintering of Jagged Particles", *J. Am. Ceram. Soc.*, 53 [7], 1970.
22. T. M. Shaw, "Liquid Redistribution During Liquid-Phase Sintering", *J. Am. Ceram. Soc.*, 69 [1], 1986.
23. F. Lange, "Liquid Phase Sintering: Are Liquids Squeezed Out from Between Compressed Particles?", *J. Am. Ceram. Soc.*, 65 [2], 1982.

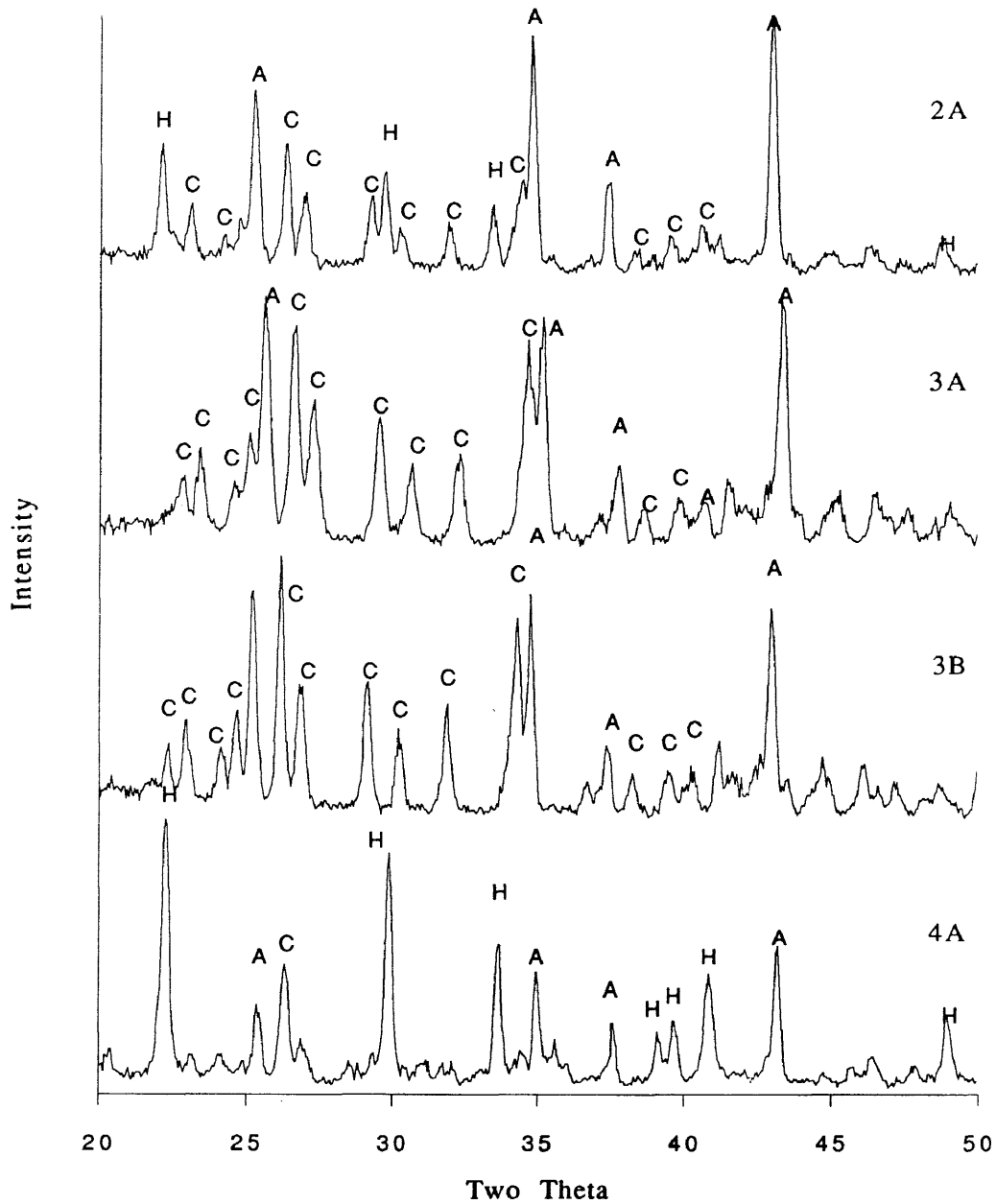
24. J. Kim, B. Kim, B. Song, D. Kim, and D. Yoon, "Effect of Sintering Atmosphere on Isolated Pores During the Liquid-Phase Sintering of MgO-CaMg-SiO<sub>4</sub>", *J. Am. Ceram. Soc.*, 70 [10], 1987.
25. J. Mencik, Strength and fracture of Glass and Ceramics, Glass Science and Technology, Volume 12, Elviseer, Amsterdam, 1992
26. Communication with M. J. Haun, Colorado School of Mines, Nov. 1992.
27. N. P. Padture and H. M. Chan, "Improved Flaw Tolerance in Alumina Containing 1 Vol% Anorthite via Crystallization of the Intergranular Glass", *J. Am. Ceram. Soc.*, 75[7], 1992.
28. W. H. Rhodes, "Agglomerate and Particle Size Effects on the Sintering of Yttria-Stabilized Zirconia", *J. Am. Ceram. Soc.*, 64, 1981.
29. Ceramic Powder Science, Ceramic Transactions, Vol. 1. Edited by G.L. Messing, E.R. Fuller, and H. Hauser. American Ceramic Society, Westerville, OH, 1988.
30. S. C. Hansen and D. S. Phillips, "Grain-Boundary Microstructures in a Liquid-Phase Sintered Alumina ( $\alpha$ -Al<sub>2</sub>O<sub>3</sub>)", *Philos. Mag. A.*, 47, 1983.
31. S. M. Wiederhorn, B. J. Hockey, R. F. Krause, and K. Jakus, "Creep and Fracture of aa Vitreous-Bonded Aluminum Oxide", *J. Mat. Sci.*, 21, 1986.
32. A. H. Heuer and P. Labun; Unpublished work.
33. H. Tomaszewski, "Effect of the Intergranular Phase Structure on the Thermomechanical Properties of Alumina Ceramics", *Ceram. Int.*, 14, 1988.
34. C. A. Powell-Dogan, "Grain Boundary Crystallization in 96% Alumina Ceramics", Ph.D. Thesis, Case Western Reserve University, 1989.
35. B. Lawn, Fracture of Brittle Solids, Cambridge University Press, Cambridge, 1993.
36. D. Bahat, "Compositional Study and Properties Characterization of Alkaline Earth Feldspar Glasses and Glass-Ceramics", *J. Mat. Sci.*, 4, 1969.
37. C. H. Drummond, III, W. E. Lee, N. P. Bansal, and M. J. Hyatt, "Crystallization of a Barium-Aluminosilicate Glass", *Ceram. Eng. Sci. Proc.*, 10 [9-10], 1989.

38. B. Yoshiki and K. Matsumoto, "High Temperature Modification of Barium Feldspar", *J. Am. Ceram. Soc.*, 34 [9], 1951.
39. R. E. Newnham and H. D. Megaw, "The Crystal Structure of Celsian (Barium Feldspar)", *Acta. Cryst.*, 13, 1960.
40. H. C. Lin and W. R. Foster, "Studies in the System BaO-Al<sub>2</sub>O<sub>3</sub>-SiO<sub>2</sub>. I. The Polymorphism of Celsian", *Amer. Min.*, 55[1], 1968.
41. D. Bahat, "Kinetic Study of the Hexacelsian-Celsian Phase Transformation", *J. Mat. Sci.*, 5, 1970.
42. C. E. Semler and W. R. Foster, "Studies in the System BaO-Al<sub>2</sub>O<sub>3</sub>-SiO<sub>2</sub>: VI. The System Celsian-Silica-Alumina", *J. Am. Ceram. Soc.*, 53 [11], 1970.
43. H. C. Lin and W. R. Foster, "Studies in the System BaO-Al<sub>2</sub>O<sub>3</sub>-SiO<sub>2</sub>: V. The Ternary System Sanbornite-Celsian-Silica", *J. Am. Ceram. Soc.*, 53 [10], 1970.
44. J. S. M. Corral and A. G. Verduch, "The Solid Solution of Silica in Celsian", *Trans. and J. Brit. Ceram. Soc.*, 77 [2], 1978.
45. N. A. Toropov, F. Y. Galukhov, and I. A. Bondar, *Izvest. Akad. Nauk S.S.S.R. Otdel. Khim. Nauk*, [5], 1954.
46. B. D. Cullity, Elements of X-Ray Diffraction, Addison-Wesley, Melno Park, CA, 1978.
47. F. H. Chung, "Qualitative Interpretation of X-Ray Diffraction Patterns of Mixtures, 1. Matrix-Flushing Method for Quantitative Multicomponent Analysis", *J. Appl. Cryst.*, 7, 1974.
48. M. W. Krutyholowa, C. Y. Kim, and C. T. Reed; Unpublished work.
49. S. R. Scholes, Modern Glass Practice, CBI Publishing Company, Inc., Boston, 1975.
50. G.W. Morrey, The Properties of Glass, 2nd edition, Reinhold, New York, 1954.
51. L.G. Van Uitert, "Relations Between Melting Point, Glass Transition, and Thermal Expansion for Inorganic Crystals and Glasses," *J. Appl. Phys.*, 50 [12], 1979.

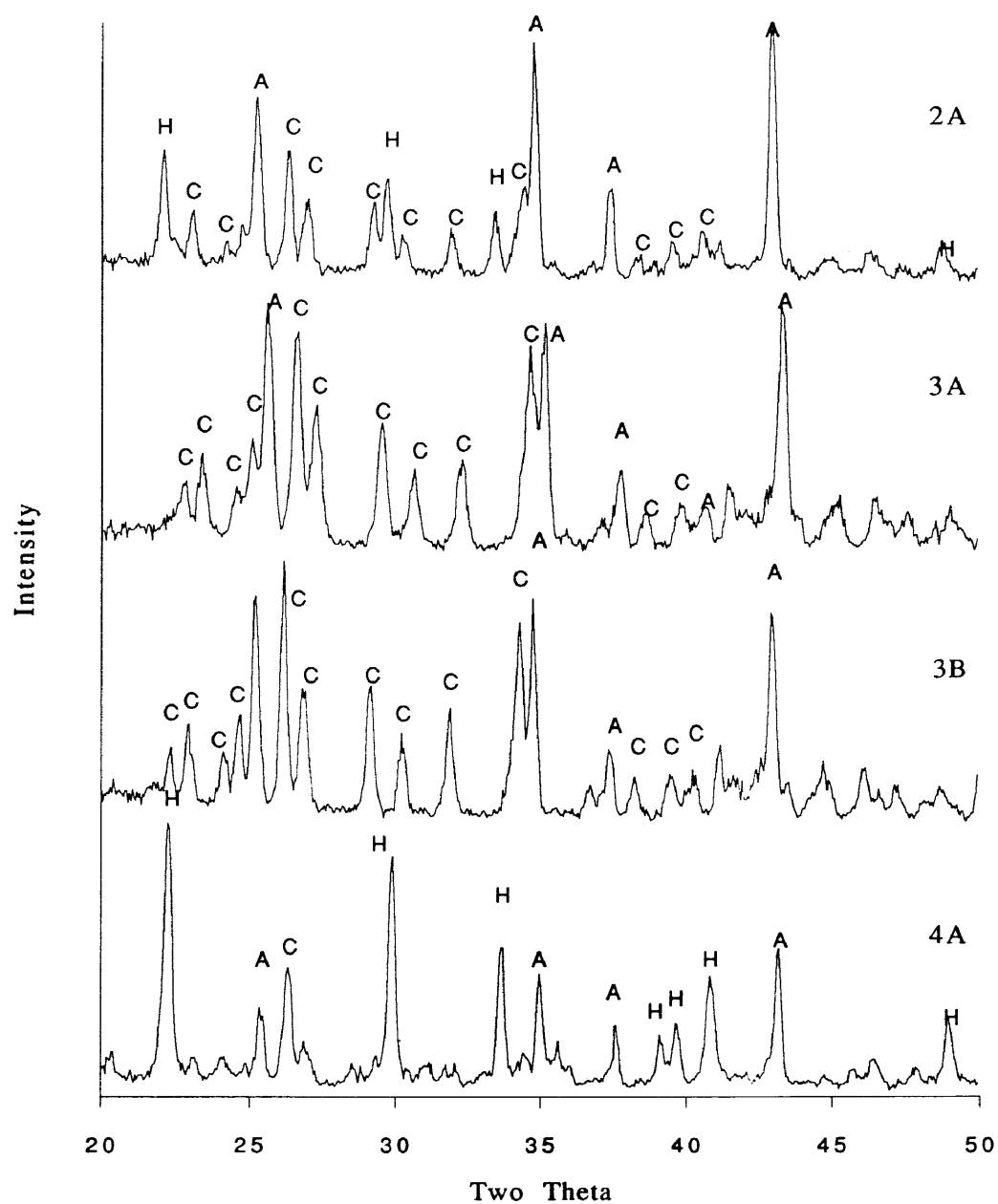
52. J. Hormadaly, "Empirical Methods for Estimating the Linear Coefficient of Expansion of Oxide Glasses From Their Composition," *J. Non-Cryst. Solids*, 79, 1986.
53. Z. Strnad, Glass-Ceramic Material, Elsevier Science Publishing Co., Inc., New York.
54. Military standard MIL-STD-1942A, November, 1990.
55. Coors Ceramics Company, "Fracture Toughness Indent Procedure", Coors Ceramics Company, Golden, CO.
56. C. T. Reed, M. J. Haun, T. K. Brog, J. D. Sibold, and K. R. McNerney, "Effects of Zirconia Additions on the Mechanical Properties of MgO-Al<sub>2</sub>O<sub>3</sub>-SiO<sub>2</sub> Based Glass-Ceramics; to be published.
57. C. A. Powell-Dogan and A. H. Heuer, "Microstructure of 96% Alumina Ceramics: 1. Characterization of the As-Sintered Materials", *J. Am. Ceram. Soc.*, 73 [12], 1990.
58. C. A. Powell-Dogan and A. H. Heuer, "Microstructure of 96% Alumina Ceramics: 2. Crystallization of High-Magnesia Boundary Glass", *J. Am. Ceram. Soc.*, 73 [12], 1990.
59. C. A. Powell-Dogan and A. H. Heuer, "Microstructure of 96% Alumina Ceramics: 3. Crystallization of High-Calcia Boundary Glass", *J. Am. Ceram. Soc.*, 73 [12], 1990.



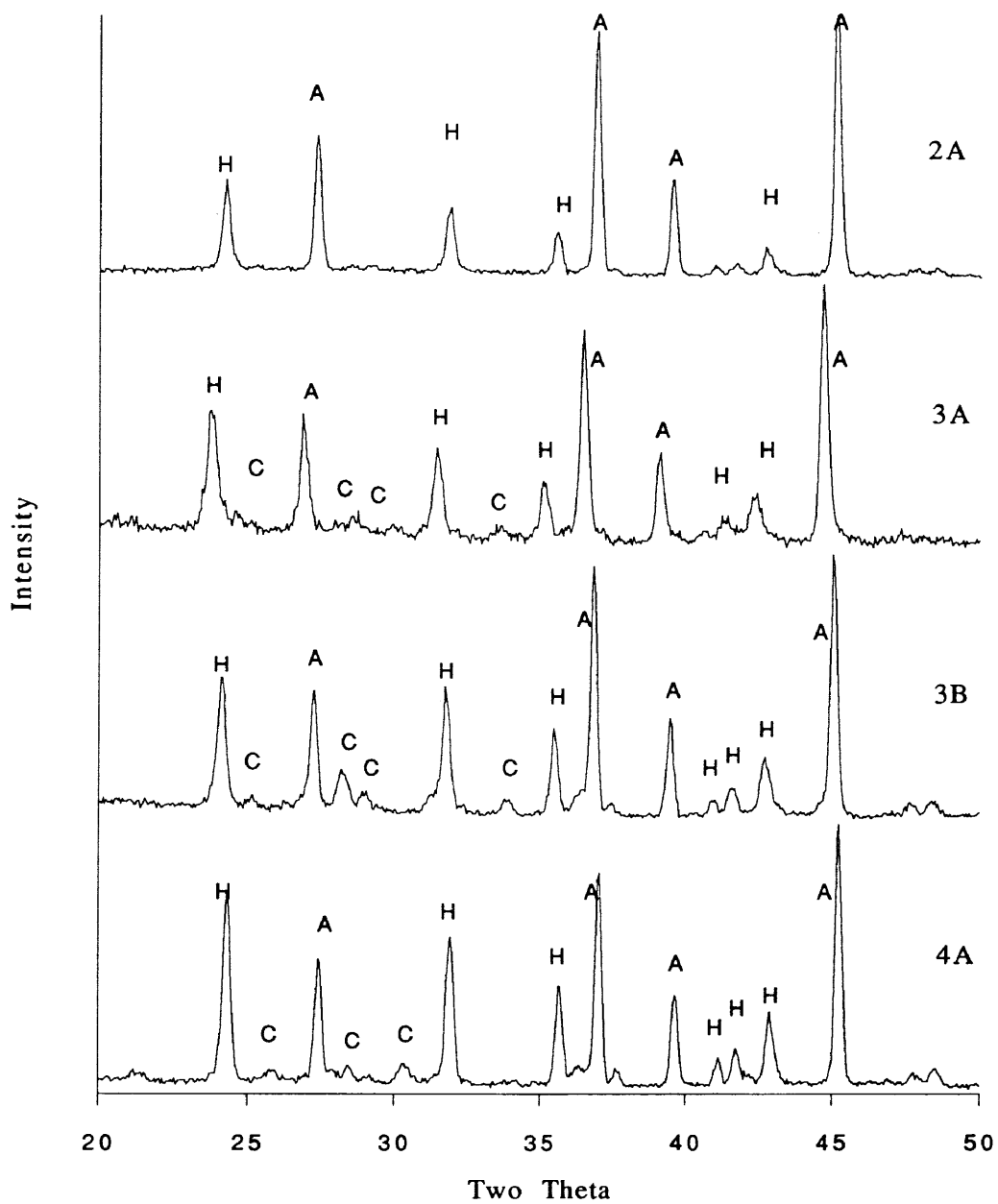
**APPENDIX A**  
**QUALITATIVE X-RAY DIFFRACTION PATTERNS**



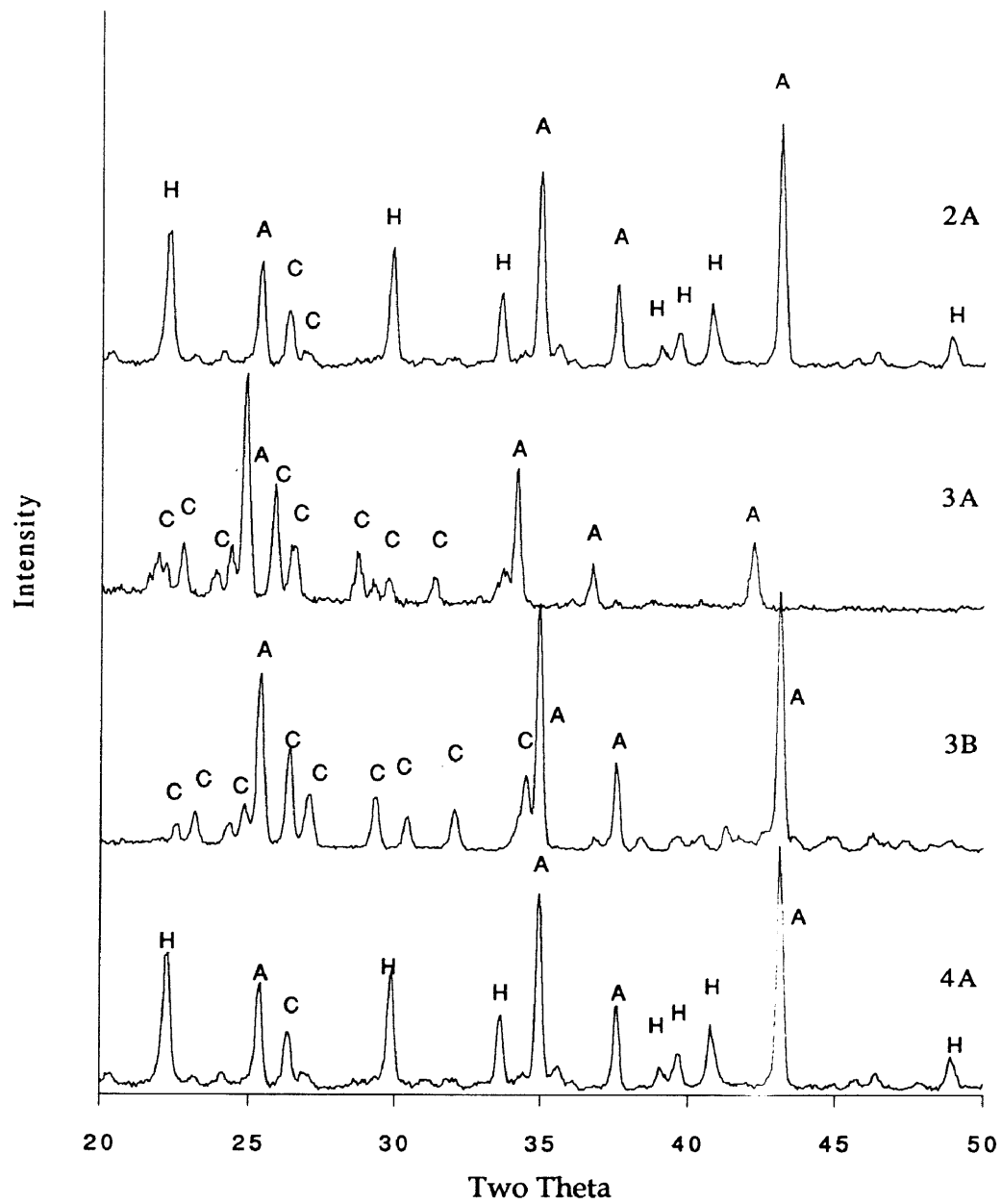
A.1. Qualitative x-ray diffraction patterns for compositions 2a, 3a, 3b, and 4a with 50 percent alumina addition, fired at 1340°C. H=Hexacelsian; C=Celsian; A=Corundum.



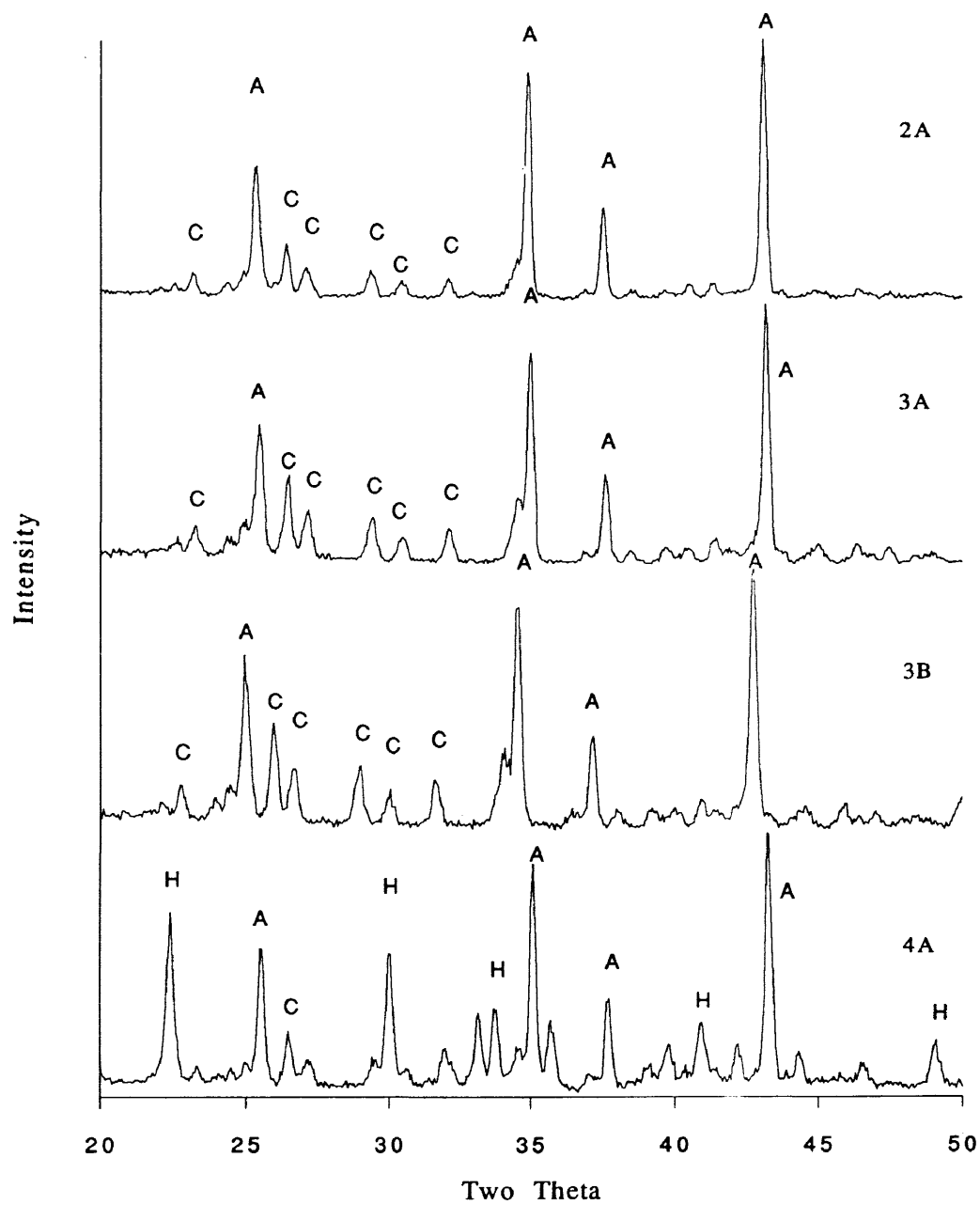
A.2. Qualitative x-ray diffraction patterns for compositions 2a, 3a, 3b, and 4a with 50 percent alumina addition, fired at 1540°C. H=Hexacelsian; C=Celsian; A=Corundum.



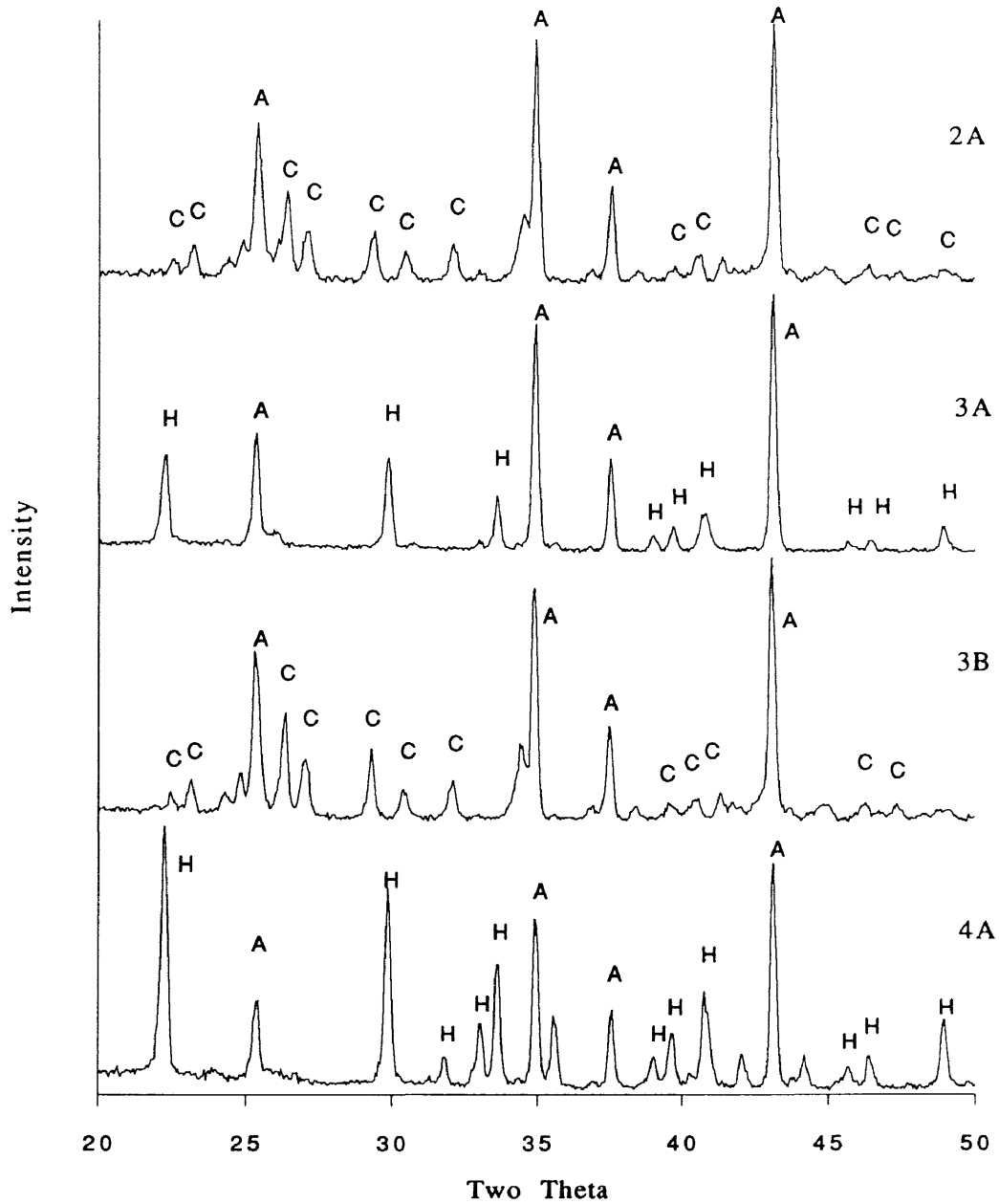
A.3. Qualitative x-ray diffraction patterns for compositions 2a, 3a, 3b, and 4a with 75 percent alumina addition, fired at 1100°C. H=Hexacelsian; C=Celsian; A=Corundum.



A.4. Qualitative x-ray diffraction patterns for compositions 2a, 3a, 3b, and 4a with 75 percent alumina addition, fired at 1340°C. H=Hexacelsian; C=Celsian; A=Corundum.



A.5. Qualitative x-ray diffraction patterns for compositions 2a, 3a, 3b, and 4a with 75 percent alumina addition, fired at 1540°C. H=Hexacelsian; C=Celsian; A=Corundum.



A.6. Qualitative x-ray diffraction patterns for compositions 2a, 3a, 3b, and 4a with 75 percent alumina addition, fired at 1640°C. H=Hexacelsian; C=Celsian; A=Corundum.

**APPENDIX B**  
**QUANTITATIVE X-RAY DIFFRACTION DATA**



**0% Alumina****2a**

<b>Temp</b>	<b>%al2o3</b>	<b>%celsian</b>	<b>%hex</b>	<b>%BaSiO3</b>	<b>%glass</b>
<b>800</b>	5.93	0	0	0	94.07
<b>1000</b>	11.37		15.44		73.19
<b>1100</b>	1.62		5.98		92.41

**3a**

<b>Temp</b>	<b>%al2o3</b>	<b>%celsian</b>	<b>%hex</b>	<b>%BaSiO3</b>	<b>%glass</b>
<b>800</b>	8.43	0	0		91.57
<b>1000</b>	8.36	20.50	18.14		53.00
<b>1100</b>	6.39	20.15	22.75		50.70

**3b**

<b>Temp</b>	<b>%al2o3</b>	<b>%celsian</b>	<b>%hex</b>	<b>%BaSiO3</b>	<b>%glass</b>
<b>800</b>	11.83	0	0		88.17
<b>1000</b>	4.92	15.50	9.69		69.89
<b>1100</b>	5.76	27.81	18.49		47.94

**4a**

<b>Temp</b>	<b>%al2o3</b>	<b>%celsian</b>	<b>%hex</b>	<b>%BaSiO3</b>	<b>%glass</b>
<b>800</b>	3.93	0	0	0	96.07
<b>1000</b>	12.85	0	15.27	13.24	58.64
<b>1100</b>	13.57	0	11.35	13.11	61.97

B.1. Weight percent of crystalline and glassy phases for compositions 2a, 3a, 3b, and 4b for samples with 0% alumina addition

### 50% Alumina

#### Comp 2a

Temp	%al203	%celsian	%hex	%BaSiO3	%glass
800	52.97	0.00	0.00		47.03
1000	48.95		10.61		40.44
1100	56.42		13.11		30.47
1340	66.27	24.34	9.40		0.00
1540	30.21	14.73	0.33		54.72

#### Comp 3a

Temp	%al203	%celsian	%hex	%BaSiO3	%glass
800	54.22				45.78
1000	59.44	16.90	23.61		0.05
1100	54.59	17.27	28.15		0.00
1340	53.26	46.63			0.11
1540	36.14	29.65	0.75		33.00

#### Comp 3b

Temp	%al203	%celsian	%hex	%BaSiO3	%glass
800	55.92				44.08
1000	59.77	19.07	20.46		0.69
1100	36.00	28.33	35.60		0.00
1340	44.31	55.68			0.00
1540	41.53	38.00	1.32		19.15

#### comp 4a

Temp	%al203	%celsian	%hex	%BaSiO3	%glass
800	51.97				48.03
1000	48.94		30.33	10.28	10.44
1100	39.46		42.39	18.15	0.00
1340	47.69	18.97	34.00		0.00
1540	15.74	20.42	25.25		39.00

B.2. Weight percent of crystalline and glassy phases for compositions 2a, 3a, 3b, and 4b for samples with 50% alumina addition.

**75% Alumina****Comp 2a**

<b>Temp</b>	<b>%al2o3</b>	<b>%celsian</b>	<b>%hex</b>	<b>%glass</b>
<b>800</b>	76.48			24
<b>1100</b>	73.68		6.67	19.65
<b>1340</b>	74.51	12.55	3.20	9.74
<b>1540</b>	76.48	12.77		10.75
<b>1640</b>	56.12	16.09		27.78

**Comp 3a**

<b>Temp</b>	<b>%al2o3</b>	<b>%celsian</b>	<b>%hex</b>	<b>%glass</b>
<b>800</b>	77.11			22.89
<b>1100</b>	60.90	8.61	14.87	15.61
<b>1340</b>	67.92	18.39	1.74	11.95
<b>1540</b>	76.21	22.75		1.04
<b>1640</b>	69.92	9.74		20.34

**Comp 3b**

<b>Temp</b>	<b>%al2o3</b>	<b>%celsian</b>	<b>%hex</b>	<b>%glass</b>
<b>800</b>	77.96			23
<b>1100</b>	74.00	8.52	15.45	2.90
<b>1340</b>	78.00	23.21	1.82	0.00
<b>1540</b>	78.27	22.03	0	0.00
<b>1640</b>	66.00	19.92	0	14.10

**Comp 4a**

<b>Temp</b>	<b>%al2o3</b>	<b>%celsian</b>	<b>%hex</b>	<b>%glass</b>
<b>800</b>	75.98			24.02
<b>1100</b>	78.00	3.00	19.00	0.00
<b>1340</b>	74.48		10.75	14.77
<b>1540</b>	68.21	11.15	15.25	5.39
<b>1640</b>	62.95		17.44	19.61

B.3. Weight percent of crystalline and glassy phases for compositions 2a, 3a, 3b, and 4b for samples with 75% alumina addition

**Composition 2a**

<b>Oxide</b>	<b>Firing Temperature (C)</b>		
	<b>800</b>	<b>1000</b>	<b>1100</b>
<b>SiO2</b>	74	78.28595	72.78513
<b>Al2O3</b>	7.5	4.401498	9.758561
<b>BaO</b>	18.5	17.31256	17.45631

**Composition 3a**

<b>Oxide</b>	<b>Firing Temperature (C)</b>		
	<b>800</b>	<b>1000</b>	<b>1100</b>
<b>SiO2</b>	61.1	67.36168	67.4099
<b>Al2O3</b>	9	0.010171	0
<b>BaO</b>	29.9	32.62815	32.5901

B.4. Residual glass composition for compositions 2a and 3a with 0% alumina addition.

**Composition 2a**

<b>Oxide</b>	<b>Firing Temperature (C)</b>				
	<b>800</b>	<b>1000</b>	<b>1100</b>	<b>1340</b>	<b>1540</b>
<b>SiO<sub>2</sub></b>	74	76.54321	82.47517	0	65.77724
<b>Al<sub>2</sub>O<sub>3</sub></b>	7.5	7.134183	1.348064	0	20.83081
<b>BaO</b>	18.5	16.32261	16.17677	0	13.39195

**Composition 3a**

<b>Oxide</b>	<b>Firing Temperature (C)</b>				
	<b>800</b>	<b>1000</b>	<b>1100</b>	<b>1340</b>	<b>1540</b>
<b>SiO<sub>2</sub></b>	61.1	0	0	0	54.77837
<b>Al<sub>2</sub>O<sub>3</sub></b>	9	0	0	0	18.86946
<b>BaO</b>	29.9	0	0	0	26.35218

**Composition 4a**

<b>Oxide</b>	<b>Firing Temperature (C)</b>				
	<b>800</b>	<b>1000</b>	<b>1100</b>	<b>1340</b>	<b>1540</b>
<b>SiO<sub>2</sub></b>	52.8	43.16577	0	0	23.9772
<b>Al<sub>2</sub>O<sub>3</sub></b>	9.7	0	0	0	44.69774
<b>BaO</b>	37.5	56.83423	0	0	31.32506

B.5. Residual glass composition for compositions 2a, 3a, and 4a with 50% alumina addition

**Composition 2a**

<b>Oxide</b>	<b>Firing Temperature (C)</b>				
	<b>800</b>	<b>1000</b>	<b>1100</b>	<b>1340</b>	<b>1540</b>
<b>SiO<sub>2</sub></b>	74	78.74646	91.92775	89.08461	70.42439
<b>Al<sub>2</sub>O<sub>3</sub></b>	7.5	5.143783	0	0.010182	18.13025
<b>BaO</b>	18.5	16.10976	8.072252	10.9052	11.44536

**Composition 3a**

<b>Oxide</b>	<b>Firing Temperature (C)</b>				
	<b>800</b>	<b>1000</b>	<b>1100</b>	<b>1340</b>	<b>1540</b>
<b>SiO<sub>2</sub></b>	61.1	58.14595	66.93995	74.86522	60.81931
<b>Al<sub>2</sub>O<sub>3</sub></b>	9	14.14554	1.12728	0.01198	9.632934
<b>BaO</b>	29.9	27.7085	31.93277	25.1228	29.54776

**Composition 4a**

<b>Oxide</b>	<b>Firing Temperature (C)</b>				
	<b>800</b>	<b>1000</b>	<b>1100</b>	<b>1340</b>	<b>1540</b>
<b>SiO<sub>2</sub></b>	52.8	0	53.4969	11.12665	43.61063
<b>Al<sub>2</sub>O<sub>3</sub></b>	9.7	0	0	0	14.82537
<b>BaO</b>	37.5	0	46.5031	88.81954	41.564

B.6. Residual glass composition for compositions 2a, 3a, and 4a with 75% alumina addition

**Composition 2a**

<b>Temp</b>	<b>0%Al<sub>2</sub>O<sub>3</sub></b>	<b>50%Al<sub>2</sub>O<sub>3</sub></b>	<b>75% Al<sub>2</sub>O<sub>3</sub></b>
<b>800</b>	8.870801	8.869858	9.0528
<b>1000</b>	8.8708	8.869858	9.0528
<b>1100</b>	13.02426	8.869858	20.2528
<b>1340</b>		25	44.3728
<b>1540</b>		55.72019	55
<b>1640</b>			61.6928

**Composition 3a**

<b>Temp</b>	<b>0%Al<sub>2</sub>O<sub>3</sub></b>	<b>50%Al<sub>2</sub>O<sub>3</sub></b>	<b>75% Al<sub>2</sub>O<sub>3</sub></b>
<b>800</b>	8.43	9.091908	9.091908
<b>1000</b>	8.36	9.091908	9.091908
<b>1100</b>	6.39	9.091908	71.04029
<b>1340</b>		1.941846	41.50654
<b>1540</b>		42.7138	4.013088
<b>1640</b>			36.83905

**Composition 4a**

<b>Temp</b>	<b>0%Al<sub>2</sub>O<sub>3</sub></b>	<b>50%Al<sub>2</sub>O<sub>3</sub></b>	<b>75% Al<sub>2</sub>O<sub>3</sub></b>
<b>800</b>	4	9.548364	9.550352
<b>1000</b>	4	8.135472	9.550352
<b>1100</b>	4	25.02	9.550352
<b>1340</b>		8.56	11.87255
<b>1540</b>		80.2132	33.22306
<b>1640</b>			59.91694

B.7. Weight percent alumina in glass plus crystalline phases for compositions 2a, 3a, and 4a with 0, 50, and 75 weight percent alumina addition

0% Al<sub>2</sub>O<sub>3</sub>

## Comp 2a

Temp	Density	Theory	% Theory
800	0	0	55
1000	3.05	3.226595	94.52689
1100	3.02	3.093934	97.61036

## Comp 3a

Temp	Density	Theory	% Theory
800	0	0	55
1000	3.27	3.633665	89.99178
1100	3.14	3.607502	87.04084

## Comp 4a

Temp	Density	Theory	% Theory
800	0	0	55
1000		3.242226	
1100	2.08	3.14081	66.22496

75% Al<sub>2</sub>O<sub>3</sub>

## Comp 2a

Temp	Density	Theory	% Theory
800	0	0	55
1000			55
1100	2.08	3.718788	55.9322
1340	2.25	3.726037	60.38587
1540	3.53	3.755299	94.00051
1640	3.46736	3.467364	99.9999

## Comp 3a

Temp	Density	Theory	% Theory
800	0	0	55
1000			55
1100	2.14	3.716686	57.57817
1340	2.22	3.824822	58.04192
1540	3.25	3.828651	84.88629
1640	3.56	3.825155	93.06811

## Comp 4a

Temp	Density	Theory	% Theory
800			55
1000			55
1100	2.16	3.817028	56.58852
1340	2.22	3.958471	56.08227
1540	2.53	3.863703	65.48122
1640	3.46	3.835715	90.20481

50% Al<sub>2</sub>O<sub>3</sub>

## Comp 2a

Temp	Density	Theory	% Theory
800	0	0	55
1000	2.09	3.478716	60.07964
1100	2.09	3.582261	58.34303
1340	2.36	3.753626	62.87254
1540	3.1825	3.182591	99.99714

## Comp 3a

Temp	Density	Theory	% Theory
800	0	0	55
1000	2.2	3.697442	59.50059
1100	2.17	3.660757	59.27736
1340	2.19	3.685545	59.42134
1540	2.9	3.567415	81.29137

## Comp 4a

Temp	Density	Theory	% Theory
800			55
1000			
1100			
1340	2.24	3.588888	62.41488
1540	2.32	3.353818	69.17489

96% Al<sub>2</sub>O<sub>3</sub>

## Comp 2a

Temp	Density	% Theory
800	0	55
1000		55
1100	2.27	56.89223
1340	2.42	60.65163
1540	3.01	75.4386
1640	3.48	87.21805

## Comp 3a

Temp	Density	% Theory
800	0	55
1000		55
1100	2.27	56.89223
1340	2.46	61.65414
1540	3.1	77.69424
1640	3.55	88.97243

## Comp 4a

Temp	Density	% Theory
800	0	55
1000		55
1100	2.27	56.89223
1340	2.39	59.89975
1540	3.15	78.94737
1640	3.63	90.97744

B.8. Density data for compositions 2a, 3a, and 4a with 0, 50, 75, and 96 weight percent alumina addition



**APPENDIX C**  
**MECHANICAL TESTING DATA**

Strength Test: Sample 29

Sample #	Length (m)	Width(in)	Thick(in)	Width(m)	Thick (m)	Max Load	MPa	
1	0.04	0.158	0.119	0.004013	0.003023	35.34	283.5775	
2	0.04	0.158	0.119	0.004013	0.003023			pressing defect
3	0.04	0.158	0.119	0.004013	0.003023	37.72	302.6753	
4	0.04	0.158	0.119	0.004013	0.003023			pressing defect
5	0.04	0.158	0.119	0.004013	0.003023			pressing defect
6	0.04	0.1585	0.119	0.004026	0.003023	31.86	255.6531	
7	0.04	0.158	0.119	0.004013	0.003023	36.61	291.3152	
8	0.04	0.158	0.1195	0.004013	0.003035			pressing defect
9	0.04	0.158	0.119	0.004013	0.003023			pressing defect
10	0.04	0.158	0.119	0.004013	0.003023	average	283.3053	
						std	17.34988	

Strength Test: Sample 6

Sample #	Length (m)	Width(in)	Thick(in)	Width(m)	Thick (m)	Max Load	MPa	
1	0.04	0.158	0.119	0.004013	0.003023	33.8891	271.9351	
2	0.04	0.158	0.1195	0.004013	0.003035	41.6246	331.2176	
3	0.04	0.158	0.1195	0.004013	0.003035	44.2031	351.7354	
4	0.04	0.1585	0.119	0.004026	0.003023	43.098	344.7388	
5	0.04	0.158	0.119	0.004013	0.003023	37.7568	302.9706	
6	0.04	0.158	0.119	0.004013	0.003023	48.4393	388.6898	
7	0.04	0.158	0.119	0.004013	0.003023			pressing defect
8	0.04	0.158	0.119	0.004013	0.003023	48.0709	385.7336	pressing defect
9	0.04	0.158	0.119	0.004013	0.003023	35.3625	283.7581	
10	0.04	0.158	0.119	0.004013	0.003023	average	332.5974	
						std	40.97002	

C.1. Flexural strength data samples 29 and 6

Strength Test: Sample 34

Sample #	Length (m)	Width(in)	Thick(in)	Width(m)	Thick (m)	Max Load	MPa
1	0.04	0.158	0.119	0.004013	0.003023	43	345.0434
2	0.04	0.158	0.1185	0.004013	0.00301	40.5	327.731
3	0.04	0.158	0.119	0.004013	0.003023	39	312.9463
4	0.04	0.158	0.119	0.004013	0.003023	40	320.9706
5	0.04	0.158	0.1185	0.004013	0.00301	48.43	391.9015
6	0.04	0.158	0.119	0.004013	0.003023	50.0969	401.9908
7	0.04	0.158	0.119	0.004013	0.003023	42.3613	339.9183
8	0.04	0.159	0.119	0.004039	0.003023		pressing defect
9	0.04	0.158	0.1185	0.004013	0.00301	44.01	356.1343
10	0.04	0.158	0.119	0.004013	0.003023		pressing defect
						average	349.5795
						std	30.27539

Flexural Strength Sample 2a

Sample #	Length (m)	Width(in)	Thick(in)	Width(m)	Thick (m)	Max Load	MPa
1	0.04	0.158	0.1195	0.004013	0.003035		pressing defect
2	0.04	0.1585	0.119	0.004026	0.003023		pressing defect
3	0.04	0.158	0.119	0.004013	0.003023		pressing defect
4	0.04	0.158	0.119	0.004013	0.003023		pressing defect
5	0.04	0.158	0.119	0.004013	0.003023	35.2336	282.7237
6	0.04	0.158	0.119	0.004013	0.003023	37.72	302.6753
7	0.04	0.158	0.1185	0.004013	0.00301	37.6095	304.3407
8	0.04	0.158	0.1185	0.004013	0.00301		pressing defect
9	0.04	0.158	0.1185	0.004013	0.00301	29.8739	241.7433
10	0.04	0.158	0.119	0.004013	0.003023		pressing defect
						average	282.8708
						std	25.22236

C.2. Flexural strength data samples 34 and 2a

Flexural Strength Sample 4a

Sample #	Length (m)	Width(in)	Thick(in)	Width(m)	Thick (m)	Max Load	MPa
1	0.04	0.158	0.119	0.004013	0.003023	37.6095	301.7886
2	0.04	0.158	0.119	0.004013	0.003023	23.0225	184.7386
3	0.04	0.157	0.119	0.003988	0.003023		pressing defect
4	0.04	0.1575	0.119	0.004001	0.003023	22.3778	180.1354
5	0.04	0.1575	0.119	0.004001	0.003023	22.8199	183.6942
6	0.04	0.158	0.119	0.004013	0.003023		pressing defect
7	0.04	0.158	0.118	0.004013	0.002997		pressing defect
8	0.04	0.158	0.1185	0.004013	0.00301		pressing defect
9	0.04	0.158	0.119	0.004013	0.003023		pressing defect
10	0.04	0.158	0.1185	0.004013	0.00301	21.0702	170.5027
					average	204.1719	
					std	49.06603	

C.3. Flexural strength data samples 4a

Sample 6

Sample #	Length (m)	Width(in)	Thick(in)	Width(m)	Thick (m)	Max Load	Strength MPa	ISB MPam2
1	0.04	0.1575	0.118	0.004001	0.002997	13.63	111.5854	3.59568
2	0.04	0.1575	0.1185	0.004001	0.00301	9.12	74.03445	2.643326
3	0.04	0.1575	0.118	0.004001	0.002997	14.05	115.0239	3.678463
4	0.04	0.1575	0.1185	0.004001	0.00301	12.62	102.4468	3.372478
5	0.04	0.1575	0.1185	0.004001	0.00301	13.37	108.5352	3.521707
6	0.04	0.1575	0.1185	0.004001	0.00301	11.93	96.8455	3.233218
7	0.04	0.1575	0.1185	0.004001	0.00301	13.45	109.1846	3.537499
8	0.04	0.1575	0.1185	0.004001	0.00301	14.53	117.9518	3.748468
9	0.04	0.1575	0.1185	0.004001	0.00301	14.53	117.9518	3.748468
10	0.04	0.1575	0.118	0.004001	0.002997	14.2	116.2519	3.707878

Avg 3.478719  
Error 0.10131

Sample #	Crack Before		KICB		Crack After		K-ICA		
	Left Ind (um)	Center (um)	Right (um)	Avg (um)	MPam2	1	2	Avg (um)	2Cb+2Ca/4 MPam1/2
1	564	693	660	639	3.348973	1100	918	1009	891.25
2	662	630	648	646.6667	2.009122	716	676	696	820.6667
3	621	586	661	622.6667	3.419701	1069	1060	1064.5	888.7917
4	576	733	606	638.3333	3.017077	1109	1031	1070	905.8333
5	660	685	721	688.6667	3.388285	1189	1204	1196.5	987.7917
6	652	635	713	666.6667	2.891661	1000	1000	1000	916.6667
7	709	580	605	631.3333	3.238565	866	992	929	863.5833
8	634	630	727	663.6667	3.660263	1050	1166	1108	940.6667
9	608	475	678	587	3.401878	995	930	962.5	827.625
10	427	574	475	492	3.003146	1120	1071	1095.5	765.875

Avg 3.137867  
Error 0.138089

Avg 4.202068  
Error 0.248515

C.4. Fracture toughness data for sample 6

Sample #	Length (m)	Width(in)	Thick(in)	Width(m)	Thick (m)	Max Load	Strength MPa	ISB MPam2
1	0.04	0.1575	0.1175	0.004001	0.002985	11.31	93.38188	3.146098
2	0.04	0.1575	0.118	0.004001	0.002997	10.76	88.08947	3.011399
3	0.04	0.157	0.1185	0.003988	0.00301	10.28	83.71688	2.898579
4	0.04	0.157	0.1185	0.003988	0.00301	10.57	86.07854	2.959692
5	0.04	0.1575	0.1185	0.004001	0.00301	11.25	91.32539	3.093991
6	0.04	0.1575	0.118	0.004001	0.002997	10.6	86.77959	2.977752
7	0.04	0.158	0.118	0.004013	0.002997	10.98	89.60609	3.050201
8	0.04	0.1575	0.118	0.004001	0.002997	11.09	90.79109	3.080405
9	0.04	0.157	0.1175	0.003988	0.002985	10.57	87.54995	2.997556
10	0.04	0.1575	0.118	0.004001	0.002997	10.5	85.96091	2.956658
							Avg	3.017233
							Error	0.022498

Sample #	Crack Before		KICB		After		KICA	
	Left Ind (um Center)	Right (um)	Avg (um)	MPam2	After 1	After 2	Avg (um)	2Cb+2Ca/4 MPam1/2
1	730	655	520	635	2.681134	1039	1040	1039.5
2	730	655	520	635	2.681134	1039	1040	1039.5
3	693	726	672	697	2.641825	1009	807	908
4	700	773	713	728.6667	2.547854	940	1053	996.5
5	632	684	685	667	2.495369	1062	1206	1134
6	649	704	687	680	2.721593	938	1128	1033
7	664	670	679	671	2.530814	1050	945	997.5
8	721	746	560	675.6667	2.646903	1060	1030	1045
9	648	736	686	690	2.726467	1027	1044	1035.5
10	564	623	643	610	2.408568	1025	1120	1072.5
	723	688	488	633	2.409152	816	856	836
							Avg	3.327027
							Error	0.0713

C.5. Fracture toughness data for sample 34

Sample #	Length (m)	Width(in)	Thick(in)	Width(m)	Thick (m)	Max Load	Strength MPa	ISB MPam2	KICB		KICA	
									Avg (um)	MPam2	2Cb+2Ca/4	MPam1/2
1	0.04	0.1575	0.118	0.004001	0.002997	18.29	148.4748	4.454664				
2	0.04	0.1575	0.1185	0.004001	0.00301	18.01	147.4434	4.431436				
3	0.04	0.1575	0.118	0.004001	0.002997	18.09	148.0984	4.446191				
4	0.04	0.1575	0.118	0.004001	0.002997	19.76	161.7702	4.75061				
5	0.04	0.1575	0.118	0.004001	0.002997	18.49	151.3731	4.519723				
6	0.04	0.1575	0.118	0.004001	0.002997	17.39	142.3676	4.316521				
7	0.04	0.1575	0.118	0.004001	0.002997							
8	0.04	0.1575	0.118	0.004001	0.002997							
9	0.04	0.1575	0.118	0.004001	0.002997							
10	0.04	0.158	0.118	0.004013	0.002997							
									Avg	4.486524		
									Error	0.054114		
Sample #	Crack Before		Right (um)	Avg (um)	KICB MPam2	After 1	After 2	Avg (um)	2Cb+2Ca/4	KICA MPam1/2		
	Left Ind (um Center)	Center (um)										
1												
2	643	628	578	616.3333	4.584982	954	794	874	834.8333	5.589672		
3	578	621	621	606.6667	4.507246	1033	936	984.5	852.7917	5.927994		
4	577	593	627	599	4.497261	1084	1084	1084	870	6.284682		
5	609	638	600	615.6667	5.053342	971	1110	1040.5	875.7917	6.773428		
6	623	571	585	593	4.585169	889	1091	990	840.5	6.123033		
7	593	567	600	586.6667	4.245421	873	1091	982	832.1667	5.692406		
8												
9												
10												
									Avg	6.065202		
									Error	0.124969		

C.6. Fracture toughness data for sample 29

**Sample 2a**

Sample #	Length (m)	Width (in)	Thick (in)	Width (m)	Thick (m)	Max Load	Strength MPa	ISB MPam2	Left Ind (u)	Crack Before Center (um)	Right (um)	Avg (um)	KICB MPam2
1	0.04	0.1575	0.118	0.004001	0.002997	10.66	87.27079	2.990385	566	588	718	312	2.433849
2	0.04	0.157	0.1185	0.003988	0.00301								
3	0.04	0.157	0.1185	0.003988	0.00301	11.2	91.20905	3.091034	781	728	607	705.3333	2.779964
4	0.04	0.1575	0.1185	0.004001	0.00301								
5	0.04	0.157	0.118	0.003988	0.002997								
6	0.04	0.1575	0.118	0.004001	0.002997	10.68	87.43453	2.994592	730	783	591	701.3333	2.627361
7	0.04	0.1575	0.118	0.004001	0.002997								
8	0.04	0.1575	0.1185	0.004001	0.00301	11.84	96.1149	3.214907	639	814	613	688.6667	2.922729
9	0.04	0.1575	0.118	0.004001	0.002997	10.52	86.12465	2.960881	809	763	708	760	2.711334
10	0.04	0.1575	0.118	0.004001	0.002997	8.58	70.24234	2.541117	675	781	742	732.6667	2.035742
							Avg	2.965486				Avg	2.585163
							Error	0.065771				Error	0.09077

**Sample 4a**

Sample #	Length (m)	Width (in)	Thick (in)	Width (m)	Thick (m)	Max Load	Strength MPa	ISB MPam2	Left Ind (u)	Crack Before Center (um)	Right (um)	Avg (um)	KICB MPam2
1	0.04	0.1575	0.1175	0.004001	0.002985	11.44	94.45523	3.173181	422	405	444	423.6667	2.096991
2	0.04	0.1575	0.117	0.004001	0.002972								
3	0.04	0.157	0.118	0.003988	0.002997								
4	0.04	0.1575	0.118	0.004001	0.002997	11.03	90.29989	3.067897	485	472	612	523	2.269677
5	0.04	0.157	0.118	0.003988	0.002997	10.09	82.86741	2.876492	412	548	578	512.6667	2.000018
6	0.04	0.157	0.118	0.003988	0.002997	10.55	86.64531	2.974296	426	342	377	381.6667	1.737818
7	0.04	0.157	0.1175	0.003988	0.002985	11.11	92.0227	3.111692	536	541	490	522.3333	2.324036
8	0.04	0.157	0.118	0.003988	0.002997								
9	0.04	0.157	0.1175	0.003988	0.002985								
10	0.04	0.157	0.118	0.003988	0.002997								
							Avg	3.040712				Avg	2.085708
							Error	0.033077				Error	0.066203

**C.7. Fracture toughness data for samples 2a and 4a**